



university of  
 groningen

faculty of mathematics  
and natural sciences

## **Silica particle formation and deposition in gas-fired appliances**

*Study of flame generated silica particle growth and deposition in domestic gas appliances  
from siloxane containing biogases*

Master thesis Chemical Engineering

Author: P. Visser

Student number: 1947400

Supervisor: prof. dr. ir. H.J. Heeres

Second corrector: prof. dr. A.A. Broekhuis

External supervisors: dr. ir. V.M. van Essen & dr. ir. S. Gersen (DNV KEMA, Groningen)

Groningen, September 2012

## Abstract

---

A growing trend in the Netherlands is the injection of biogases into the natural gas grid for transportation and distribution to end-users (industrial, commercial and residential). Biogases can contain (trace) compounds, like for example siloxanes, which may have adverse effects on the integrity of the gas infrastructure, the safety and performance of gas utilization equipment and even the health of end users. The harmful aspect of siloxanes is that they are converted to silicon dioxide (silica,  $\text{SiO}_2$ ) particles upon combustion, which deposit as a layer on relatively cold parts of gas utilization equipment. The impact of the presence of siloxanes in biogases on the performance of domestic end-user equipment is discussed in this thesis.

In chapter 3, transmission electron microscopy (TEM) measurements and theoretical analysis are combined to construct the physical picture of silica particle formation in premixed laminar methane/air flames. In the reaction zone of the flame siloxanes are quickly converted to a supersaturated  $\text{SiO}_2$  (g) vapor. Nucleation of silica causes nanoclusters to appear in the early stage of combustion. These nanoclusters will continue to grow into larger clusters via Ostwald ripening, sintering processes (after collision between (nano)clusters) and by taking up free  $\text{SiO}_2$  (g) molecules. Further downstream, after cooling of the combustion products clusters combine to form fractal aggregates. The measured sizes of clusters and fractal aggregates are in accordance with those calculated with theoretical models. The presented models are divided in two flame regions: one where cluster growth is the dominant process and one where fractal aggregate growth is the dominant process. The position of the dividing line between these regions can be determined experimentally and depends on the temperature of the flame and the concentration of silica particles. An increased temperature favors the cluster growth process and an increased concentration favors the fractal aggregate growth process.

In chapter 4, practical tests were performed with domestic appliances (boiler and geyser) operating on siloxane containing natural gas to study silica deposition. In a widely used boiler in the Netherlands clogging of the heat exchanger by silica deposition (>90% yield of deposition) resulted in an increased flow resistance. This flow resistance caused a significant reduction of the thermal output of the appliance. Experiments with different siloxane concentrations yielded that the flow resistance scaled non-linearly with the siloxane concentration in natural gas. This indicates that the density of the silica layer changes with the siloxane concentration. The density influences the layer thickness, which in turn influences the flow resistance. At higher siloxane concentrations the silica layer would be thicker and at lower concentrations the silica layer would be thinner due to the density. This difference may be caused by the morphology or the size of the silica particles in the heat exchanger.

Siloxane admixture caused the combined ionization and ignition probe of the boiler appliance to be covered with silica. This silica layer decreased the measured ionization current. After some time the critical value for the ionization current was reached and the boiler automatically turned off. The time till failure did not scale linearly with concentration.

This non-linearity may be caused by the density of the silica layer or by an effect of siloxanes (or a combustion product of siloxanes) on the ions in the flame.

Silica deposition in the heat exchanger of a domestic gas geyser also resulted in clogging of the heat exchanger by silica deposition. Here, the increased flow resistance caused the CO emissions to increase exponentially.

In chapter 5, a simplified model is presented to describe silica deposition in heat exchangers. Several trends observed in experiments were in accordance with the deposition model. For example, the position of silica deposition and the yield of deposition could roughly be determined. In order to make a quantitative analysis of the silica deposition a more detailed model should be developed. With this model, the maximum allowable silicon content in biogases can be determined by extrapolating the results from the practical appliances to low concentrations. This avoids the need to perform time consuming long-term tests at these concentrations.

## Preface

---

This master thesis concludes my master program for the study of chemical engineering at the faculty of Mathematics and Natural Sciences, University of Groningen. The research was carried out at the DNV KEMA Gas Consulting & Services (GCS) premises in Groningen. I appreciate all the help from my colleagues at GCS in the process of writing my thesis and the work that preceded it. Moreover, I would like to thank them for the always-pleasant working atmosphere within the company.

Special thanks go to my supervisors at GCS, dr. ir. V.M. van Essen and dr. ir. S. Gersen. Martijn and Sander, without your help I would not have been able to perform my graduation project at GCS. You know that it was my fervent wish to graduate within a company and GCS in particular because of my interest in (bio)gas related topics, you made that wish come true for me. I remember the discussions we had as fruitful and in times of disappointment, you always knew the next step to take. I have learned much from you and I will strive to use everything you taught me throughout my career.

I acknowledge prof. dr. ir. H.J. Heeres for the opportunity to perform my graduation project under his supervision and prof. dr. A.A. Broekhuis for his work being the second corrector. I would like to thank prof. dr. H.B. Levinsky and dr. A.V. Mokhov of the Combustion Technology research group (University of Groningen) for their help and patience during the in depth discussions we had. I thank dr. A.V. Sepman (Combustion Technology) for his help and letting me use his laboratory to perform flame temperature measurements. Furthermore, I would like to thank ir. M. Dutka, dr. J. Rao, dr. A.A. Türkin, dr. D.I. Vainchtein and prof. dr. J.Th.M. de Hosson at the Department of Applied Physics, Zernike Institute for Advanced Materials, University of Groningen for their helpful discussions and the work performed with the electron microscopes.

Last but not least, I thank my parents Tjeerd and Anna Hinke for supporting and encouraging me throughout my study and my girlfriend Rommie for her unconditional love and support.

# Table of contents

---

<b>Abstract</b>	<b>i</b>
<b>1. Introduction</b>	<b>1</b>
<b>2. Combustion of siloxanes in natural gas flames</b>	<b>3</b>
2.1 Structure and properties of siloxanes	3
2.2 Siloxanes in biogas	4
2.3 Laminar premixed flames	4
2.4 Silica formation in premixed flames	7
<b>3. Silica particle formation in methane /air flames</b>	<b>10</b>
3.1 Experimental setup to study silica particle formation in flames	10
3.1.1 Laminar 1-D burner	10
3.1.2 Gas handling system	10
3.1.3 Localized thermophoretic sampling system	13
3.2 Experimental results and discussion	15
3.2.1 Silica yield experiment	15
3.2.2 Influence of siloxane concentration on silica particle formation	17
3.2.3 Influence of distance above the burner surface on silica particle formation	18
3.2.4 Influence of flame temperature on silica particle formation	24
3.2.5 Silica particle formation models	27
3.2.5.1 Cluster growth region	28
3.2.5.2 Fractal aggregate growth region	30
3.3 Summary and conclusions: particle formation in flames	32
<b>4. Silica deposition in domestic appliances</b>	<b>33</b>
4.1 Experimental setups to study silica deposition in domestic appliances	33
4.1.1 Intergas domestic boiler	33
4.1.2 Gas handling system for studying silica deposition in the Intergas boiler	34
4.1.3 Vaillant domestic geyser	35
4.1.4 Gas handling system for studying silica deposition in the Vaillant geyser	36
4.2 Experimental results and discussion	37

4.2.1	<i>Clogging of the lamella heat exchanger by silica deposition</i>	37
4.2.2	<i>Effect of siloxanes on the ionization probe</i>	41
4.2.3	<i>Influence of silica clogging on CO emissions in a domestic geyser</i>	44
4.3	<i>Summary and conclusions: silica deposition in domestic appliances</i>	45
<b>5.</b>	<b>Silica particle deposition model</b>	<b>47</b>
5.1	<i>Temperature profile in the heat exchanger</i>	47
5.2	<i>Thermophoresis and diffusion</i>	51
5.3	<i>Deposition model</i>	52
5.4	<i>Summary and conclusions: silica deposition model</i>	57
<b>6.</b>	<b>Recommendations for future work</b>	<b>58</b>
	<b>References</b>	<b>59</b>
	<b>Appendix I: Gravimetric determination of siloxane concentrations</b>	<b>62</b>
	<b>Appendix II: Optimization of the sampling probe design</b>	<b>64</b>
	<b>Appendix III: The TEM image processing</b>	<b>66</b>
	<b>Appendix IV: Silica mass balance over the Intergas domestic boiler</b>	<b>67</b>
	<b>Appendix V: Temperature profile in the Intergas boiler</b>	<b>68</b>
	<b>Appendix VI: Thermal conductivity coefficients and specific heats</b>	<b>70</b>

## 1. Introduction

---

Increasingly stringent regulations regarding CO<sub>2</sub> emissions and the growing desire to enhance the sustainability of the energy supply have resulted in an increasing trend towards the use of biogases in the Netherlands. Given the existing natural gas infrastructure an (cost-) effective way to transport and deliver biogases to end-users (industrial, commercial and residential) is to inject them into the natural gas grid. There are currently fifteen sites in the Netherlands where biogases are injected in the gas distribution grid and there is one site where biogases are injected in the transmission grid [1].

Biogases can contain (trace) compounds which are not present in natural gas. These compounds can have adverse effects on the integrity of the gas infrastructure, the safety and performance of gas utilization appliances and even on the health of end users. One of these compounds is siloxanes. Siloxanes are a subgroup of silicones that contain alternating silicon and oxygen atoms with alkyl or other functional organic groups bound to silicon. Siloxanes are widely used because of their useful properties, including high compressibility, low flammability, low surface tension, water repellent properties and a high thermal stability. Furthermore they present a low toxicity, low allergy, they are not environmental persistent and compliant with volatile organic compound restrictions. Because of these properties siloxanes are frequently added to consumer products. Some of these products are detergents, shampoos, cosmetics, paper coatings and textiles. In addition siloxanes are released as a residue in the production of silicon containing chemicals [2]. Annually the worldwide production of siloxanes is estimated at over one million tons [3].

Siloxane containing products or their packagings end up in landfills and in the sludge of wastewater treatment plants. As a result siloxanes may end up in biogases produced from landfill waste and wastewater sludge but siloxanes can also be present in biogases from other sources. This may be partially due to the addition of silicon anti foaming agents in digesters, which can biodegrade to siloxanes [2].

Upon combustion, siloxanes are converted to silicon dioxide (silica, SiO<sub>2</sub>) particles, which deposit as a layer on relatively cold parts of gas utilization equipment. For example, Figure 1 shows a silica covered piston head from a gas engine after operating on siloxane containing biogases [4]. These particles have proven to be highly abrasive in gas utilization equipment with moving parts like gas engines. As a result, gas engine manufacturers have put up specifications for the maximum allowable siloxane concentration in the gas engine operating on biogases based on the maintenance regime.

In gas appliances, silica particles may deposit on for example the heat exchanger and can cause deterioration in the performance. Gas appliances with narrow channels in the heat exchanger will suffer adverse effects most quickly. Since domestic appliances tend to have compact heat exchangers, which can be relatively easily blocked, these appliances will be particularly susceptible to clogging by silica formation. Progressive clogging of heat exchangers may lead to an increased pressure drop resulting in a decreased flow or spillage of flue gases. In addition an increased pressure drop can lead to increased carbon monoxide (CO) emissions. Furthermore, possible formation of silica nanoparticles (<100 nm) in gas

utilization equipment may lead to an increased environmental or health burden if spilled in the exterior.



**Figure 1: Piston head covered with silica [4].**

Given the growing trend towards the introduction of biogases in the natural gas grid and the needed flexibility to use different types of biomass for the production of biogases, the development of well founded siloxane specifications (or in general specifications for silicon containing compounds) for gas utilization equipment are needed. Many European countries (at least France, Germany, Sweden and Switzerland) excluding Austria and the Netherlands did not yet develop siloxane specifications. The siloxane specification in Austria and the Netherlands are  $10 \text{ mgSi/m}^3_n$  and 5 ppm respectively [5]. In the Netherlands however, this value is not based on proper research. Specifications should take into account the performance, lifetime of equipment, safety, environmental and health aspects, which is not the case with the Dutch siloxane specification. To develop specifications based on a physically correct basis, fundamental knowledge on silica particle formation in flames and deposition in appliances is essential.

In this thesis, an effort is made to develop this knowledge with the focus on domestic appliances. First, the silica particle formation in laminar premixed flames at well-defined laboratory conditions is studied (Chapter 3). The results obtained from these experiments are combined with results from practical tests using domestic appliances (Chapter 4) to study and model deposition of silica in heat exchangers (Chapter 5). It should be noted that time consuming long-term tests (order of years) using domestic appliances were not performed. Therefore, although outside the scope of this thesis, a silica deposition model is essential in estimating the maximum allowable silicon content in biogases by extrapolating the results from the short-term practical tests with domestic appliances. I.e. with a silica deposition model siloxane specifications made. The goal of this thesis is to develop this model used to describe silica deposition in heat exchangers of domestic appliances.



## 2. Combustion of siloxanes in natural gas flames

In this chapter, the properties of some common siloxanes in biogases are described. Also, laminar premixed flames, which are similar to the flames in many domestic gas appliances are discussed to study the formation of silica particles.

### 2.1 Structure and properties of siloxanes

Siloxanes have either linear (L) or cyclic (D) structures, hexamethyldisiloxane ( $C_6H_{18}Si_2O$ ) is an example of a linear siloxane with the abbreviation L2 and octamethylcyclotetrasiloxane ( $C_8H_{24}Si_4O_4$ ) is an example of a cyclic siloxane with the abbreviation D4 [2]. Note that the number in the abbreviations corresponds to the amount of silicon atoms present in the molecule. Figure 2 shows the repeating structural unit for both linear and cyclic siloxanes [2].

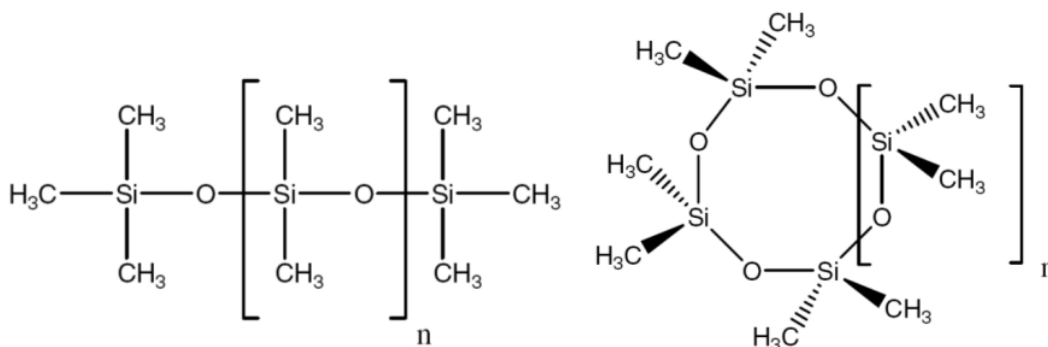


**Figure 2: Repeating structural units for linear (left) and cyclic (right) siloxanes. The left siloxane is L3 and the right siloxane is D4 [2].**

Table 1 shows the properties of several types of siloxanes at 25 °C [6]. Most siloxanes have high vapor pressures, low water solubility and a high Henry constant. This indicates that they easily transfer from a water solution to the gas phase [7].

**Table 1: Siloxane properties (25 °C).**

Formula [-]	Abbreviation [-]	Molecular weight [g/mole]	Vapor pressure [Pa]	H <sub>2</sub> O solubility [μg/L]	Henry's const. [-]
$C_6H_{18}Si_2O$	L2	162.38	5613	933	397
$C_8H_{24}Si_3O_2$	L3	236.53	445	34.5	-
$C_{10}H_{30}Si_4O_3$	L4	310.77	50	6.76	-
$C_6H_{18}Si_3O_3$	D3	222.46	471	1563	-
$C_8H_{24}Si_4O_4$	D4	296.62	140	56.3	259
$C_{10}H_{30}Si_5O_5$	D5	370.77	27	17.2	185
$C_{12}H_{36}Si_6O_6$	D6	444.93	3	5.14	104

## 2.2 Siloxanes in biogas

The properties of siloxanes indicate that in waste water treatment plants and landfills siloxanes are easily volatilized into biogas [7]. The siloxane concentration in biogas may vary depending on the biogas production/process conditions and the properties of present siloxanes. In a study performed by M. Schweigkofler and R. Niessner [8] a total siloxane concentration of 50 mg/m<sup>3</sup> in different types of biogases was reported. D6, D5, D4, D3, L4, L3 and L2 were found to be present in landfill biogases according to this study. According to a study by R. Dewil, L. Appels and J. Baeyens [2] concentrations of siloxanes were present in biogases<sup>A</sup> in the ranges of 5 – 400 mg/m<sup>3</sup>. In this study at least siloxanes D4 and D5 were found with higher concentrations of D5. In our own measurements of biogases in the Netherlands, concentrations of up to 85 mg/m<sup>3</sup> of D5 and up to 14 mg/m<sup>3</sup> of D4 were found<sup>B</sup>. Beside siloxanes, biogases may also contain organic silicon compounds other than siloxanes which are also converted to silica upon combustion. For example, methoxytrimethyl silane, tetramethylsilane, trimethylfluorosilane and trimethylpropoxysilane have been detected in biogases from waste water treatment plants [7].

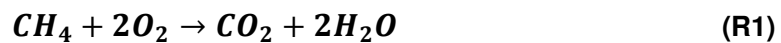
## 2.3 Laminar premixed flames

Laminar premixed flames are an important tool for combustion research due to the relatively simple structure of these flames. Their one-dimensional (1-D) structure (Figure 3) allows for numerical modeling and model to experiment comparison [9, 10, 11].

In laminar premixed flames, fuel and oxidizer are homogeneously mixed prior to combustion. The composition of a premixed fuel/oxidizer mixture is usually expressed as the equivalence ratio  $\phi$ , which can be calculated with equation (1) if the composition of the premixed gas mixture is known. In equation (1), the molar ratio of fuel and oxidizer is divided by the molar ratio of a stoichiometric mixture to determine  $\phi$ .

$$\phi = \frac{(n_{fuel}/n_{oxidizer})}{(n_{fuel}/n_{oxidizer})_{st.}} \quad (1)$$

where  $n_{fuel}$  and  $n_{oxidizer}$  are the amounts of fuel and oxidizer expressed in either moles or mole fractions. A flame is considered stoichiometric ( $\phi=1$ ) if fuel and oxidizer consume each other completely leaving only reaction products as shown, for example, in reaction (R1) for methane and oxygen. Fuel rich combustion occurs in the case of excess fuel ( $\phi>1$ ) and fuel lean combustion occurs in the case of excess oxidizer ( $\phi<1$ ).



The combination of heat and mass transfer with chemical reaction results in a spatial structure for laminar premixed flames, as illustrated in Figure 3.

---

<sup>A</sup> Sources landfill and sewage treatment plants in Belgium, Germany, Switzerland and the United Kingdom

<sup>B</sup> Sources sewage treatment plants, co-digestion and landfill gas

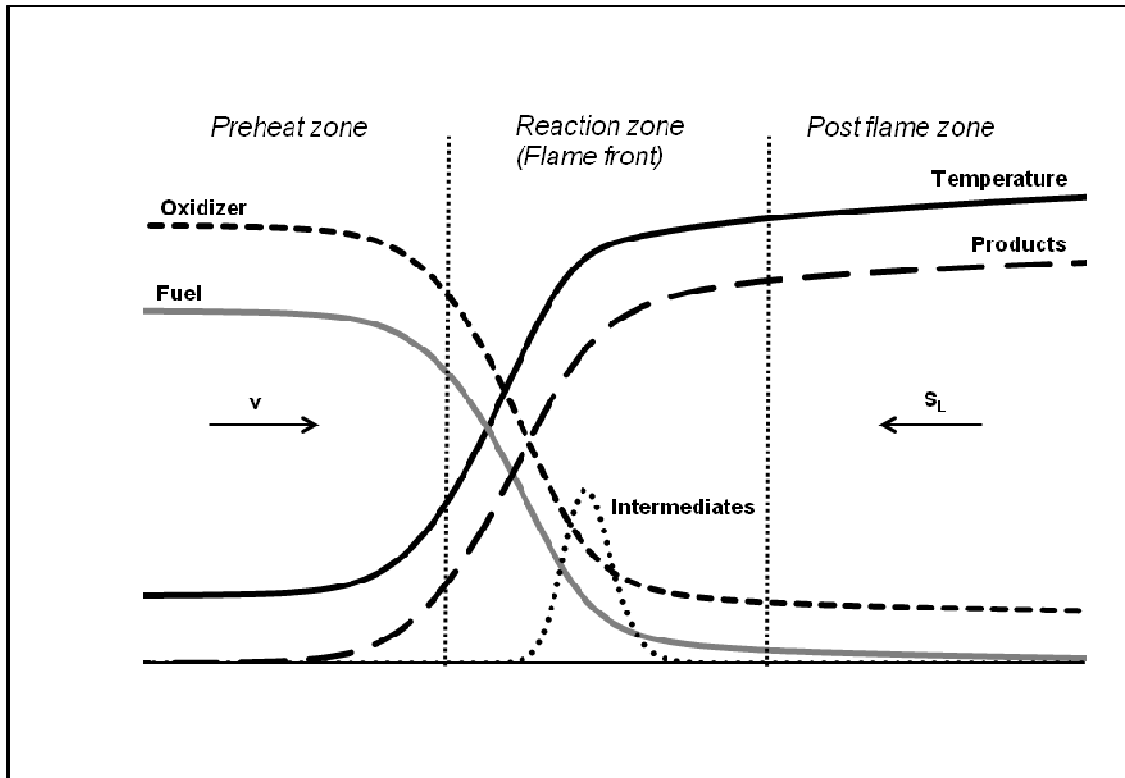


**Figure 3: Spatial structure of a laminar premixed flame, the temperatures and concentration of species is given as a function of distance above the burner surface.**

The spatial structure can be divided in three main zones, the preheat zone, the reaction zone (or flame front) and the post flame zone. In the first zone, the cold premixed gas is heated through conduction and diffusion of species from the reaction zone. The reaction takes place in the second zone where the temperature further increases due to the release of chemical energy. The temperature in the reaction zone is sufficiently high to produce intermediate chemicals (radicals) to sustain the flame. In the post flame zone the reaction is completed, the temperature levels out and concentrations of the mayor species approach equilibrium [9, 10, 11].

The laminar burning velocity ( $S_L$ ), which is strongly dependent on the gas composition, temperature and pressure of the unburned fuel and oxidizer mixture, is a characteristic value for laminar premixed flames. If  $v$  is the velocity of the cold fuel/oxidizer mixture then  $S_L - v$  is the velocity at which the flame front propagates. Three situations can be considered regarding  $S_L$  and  $v$  which are  $S_L = v$ ,  $S_L < v$  and  $S_L > v$ . In the first situation ( $S_L = v$ ) the flame front is stationary relative to the burner surface and all heat generated during combustion is transferred into the gas mixture, the flame in this situation is called the adiabatic or freely propagating flame. The temperature for adiabatic flames is the maximum flame temperature that can be achieved for the corresponding fuel/oxidizer mixture. In the second situation ( $S_L < v$ ) the flame front moves downstream, away from the burner surface which results in flame lift and ultimately in blow off. In the last situation ( $S_L > v$ ) the flame front propagates upstream, towards the burner surface. Here the flame transfers heat to the burner surface

resulting in a lower flame temperature, which decreases the actual burning velocity. Due to the heat transfer to the burner surface the system reaches a new stationary situation, this type of flame is called a burner stabilized flame. Figure 4 shows a schematic of both a freely propagating flame and a burner stabilized flame [9, 10, 11]. Note the distance between flame and burner surface for the freely propagating flame in comparison to the burner stabilized flame.

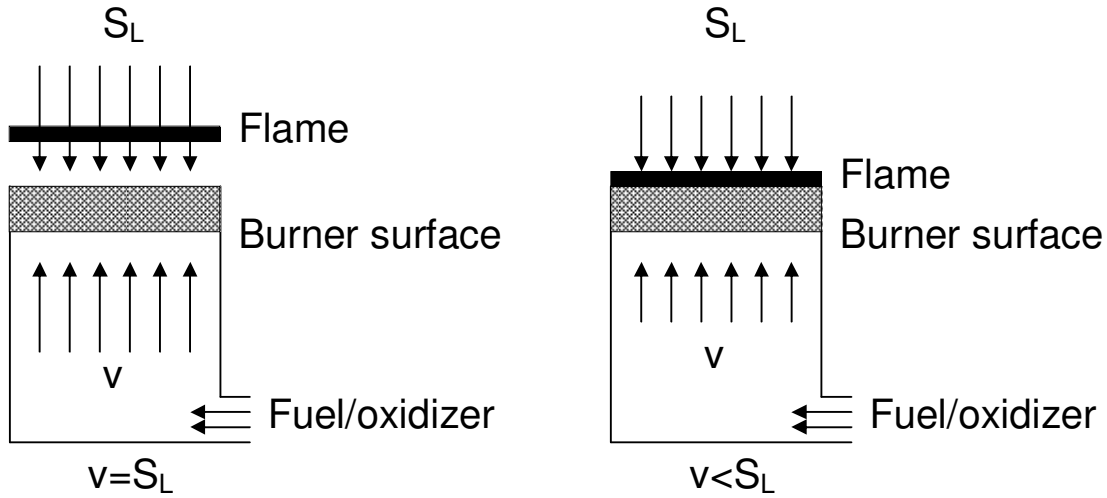


**Figure 4: Freely propagating flame (left) and a burner stabilized flame (right) in which  $S_L$  is the laminar burning velocity and  $v$  is the cold gas velocity.**

In this thesis premixed flames are numerically modeled using the PREMIX code of CHEMKIN II with the GRI-Mech 3.0 chemical mechanism (hereafter shortly called PREMIX). The GRI-Mech 3.0 mechanism which describes the combustion process from reactants to products, uses a set of 325 elementary reactions and 53 species [10, 12, 13]. Temperatures and composition of species as function of distance above the burner surface are calculated with PREMIX for both freely propagating and burner stabilized stoichiometric premixed methane/air flames. In Figure 5 the temperatures of these flames with different mass flow rates,  $\rho \cdot v$  in  $\text{g/cm}^2 \cdot \text{s}$  are shown after complete reaction. For the numerical calculations equations for the conservation of mass, species and energy are solved for the flame system, assuming no heat losses to the environment [13]. As can be seen in Figure 5 the flame temperature can be varied over a wide range to study the influence of temperature on silica particle formation in flames. According to a study performed by A.V. Sepman [11] the flame temperatures calculated with PREMIX are accurate and similar to measured temperatures for premixed laminar methane/air flames.

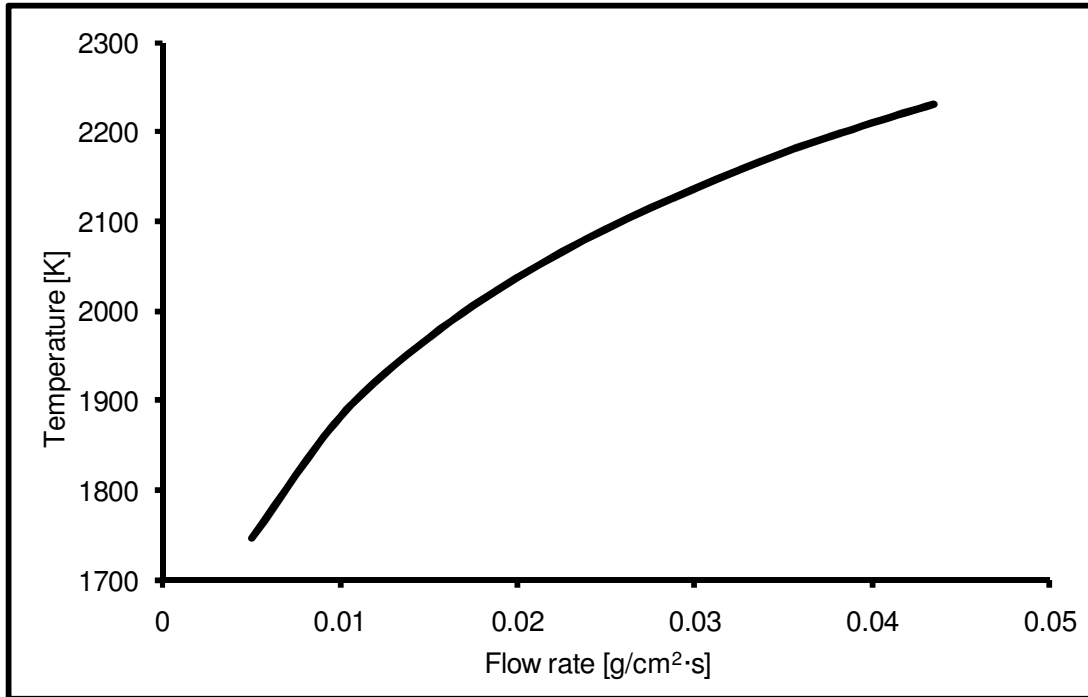
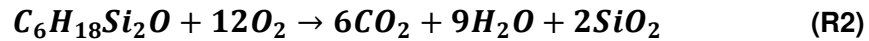


**Figure 5: Calculated temperatures (PREMIX) for stoichiometric premixed CH<sub>4</sub>/air flames for different mass flow rates after complete combustion assuming no heat losses to the environment.**

## 2.4 Silica formation in premixed flames

Upon combustion, siloxanes in biogases form silica. As an example, the overall oxidation reaction of L2 is shown in reaction (R2) wherein each L2 molecule produces 2 silica molecules in the case of complete oxidation.



It is unrealistic to think that combustion of L2 in biogases (mainly methane) takes place via one single reaction described by the overall reaction (R2). Instead, the combustion in the reaction zone occurs in a sequential process involving many reactions. Although studies on the combustion kinetics of Si containing compounds in counter flow methane-nitrogen-L2/air flames have been performed by H.K. Chagger et al. [14] to our knowledge a detailed chemical mechanism to simulate the combustion of siloxanes doesn't exist. Chagger et al. found that L2 decomposes rapidly to form gaseous silicon monoxide, SiO (g) which subsequently oxidizes to SiO<sub>2</sub> and proposed mechanisms for SiO<sub>2</sub> formation. In accordance with the findings of Chagger et al., thermodynamic equilibrium calculations indicate that during combustion of methane/silicon/air mixtures all silicon is converted to either SiO (g) or SiO<sub>2</sub> (g). According to these calculations, the ratio between SiO and SiO<sub>2</sub> in the flue gases depends on both the temperature and the initial silicon concentration in the fuel. Although there is no experimental evidence to support these calculations the same behavior for the

formation of  $\text{SiO}_x$  is assumed when siloxanes are added to unburned  $\text{CH}_4/\text{air}$  mixtures. To study the temperature and concentration dependence on the formation of  $\text{SiO}$  (g),  $\text{SiO}_2$  (g) and condensed  $\text{SiO}_2$  in flames equilibrium concentrations of silicon based chemicals after combustion of methane/air with respectively 0.5 and 5 ppm silicon in methane [15] have been calculated and illustrated in Figure 6 and Figure 7.

At low temperatures (<1700K) silicon in the flue gases is only present in the form of condensed silica according to these graphs. Condensed silica can be either in a solid or liquid state depending on the structure (amorphous or one of several crystalline structures), the size of the silica particles and the temperature. It is unknown at which temperature silica becomes solid (melting point/trajectory depending on the structure ~1990 K [16]), we can assume however that all silica eventually become solid after cooling down to moderate temperatures (<1500 K). Between Figure 6 and Figure 7 it can be seen that the temperature at which the bulk of the  $\text{SiO}_2$  (g) condenses is increasing with the initial silicon concentration. After combustion silicon containing compounds are considered to be in an equilibrium state, however it should be noted that it is uncertain to which degree thermodynamic equilibrium is reached during different phases of combustion [15].

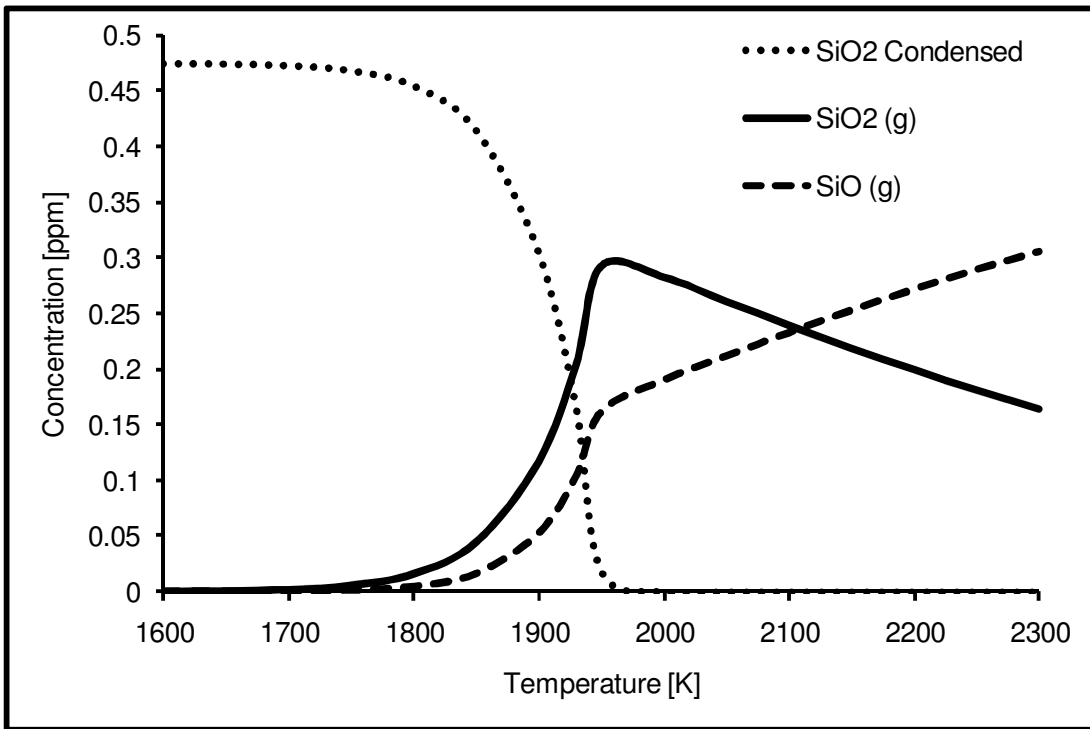


**Figure 6: Equilibrium concentrations of  $\text{SiO}_2$  Condensed,  $\text{SiO}_2$  (g) and  $\text{SiO}$  (g) after stoichiometric combustion of methane/air with 5 ppm silicon in methane.**

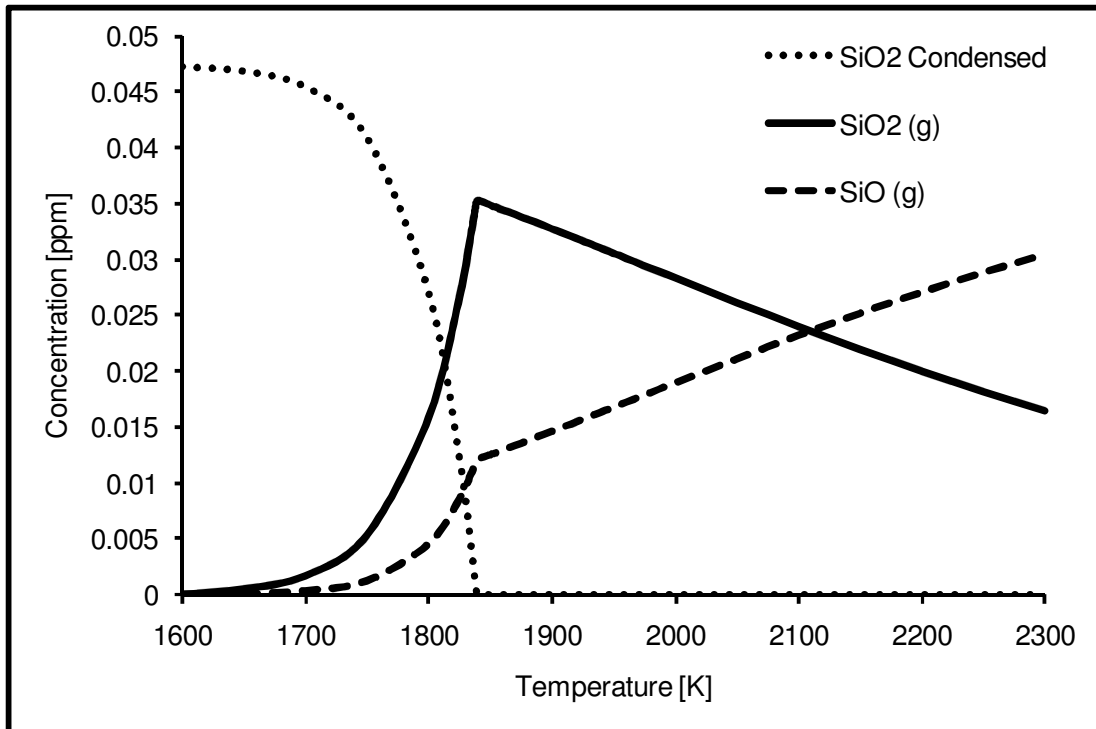


Figure 7: Equilibrium concentrations of SiO<sub>2</sub> Condensed, SiO<sub>2</sub> (g) and SiO (g) after stoichiometric combustion of methane/air with 0.5 ppm in methane.

### 3. Silica particle formation in methane /air flames

---

In this chapter the experimental setup, results and conclusions regarding the silica particle formation in premixed laminar 1-D methane/air flames are described. Equations for the growth of silica particles in flames are presented and discussed. These equations form a basis for deposition models used for domestic appliances which will be described later in this thesis.

#### 3.1 Experimental setup to study silica particle formation in flames

##### 3.1.1 Laminar 1-D burner

The measurements were performed in premixed laminar 1-D methane/air flames stabilized above a custom made perforated ceramic tile burner (pore diameter of ~1mm) of 6 cm in diameter. The ceramic tile burner used for the experimental work in this chapter is shown in Figure 8.



**Figure 8: Photograph of the custom made perforated ceramic tile burner.**

A cylindrical chimney with a 6 cm inner diameter and a length of 40 cm was positioned above the burner to stabilize the flame. The burner was fixed to a positioner (FINN Corporation) with a precision of 0.1 mm, to allow for sampling of silica particles as a function of distance above the burner surface.

##### 3.1.2 Gas handling system

To produce the premixed methane/siloxane/air mixtures the gas handling system shown schematically in Figure 9 was used. Methane supplied in gas cylinders, with a purity better than 99.99% as guaranteed by manufacturer (Linde gas), was used during the experimental work. The air is dried and made free of particulates and oil on-site using filters. All gas flows



are provided as volumetric flow rates normalized to 273 K and 1 atmosphere and measured using calibrated Bronkhorst EL-FLOW mass flow meters with an accuracy of  $0.5\% + 0.1\%$  of full scale. The minimum flow for accurate measurement is at 2% of the full scale.

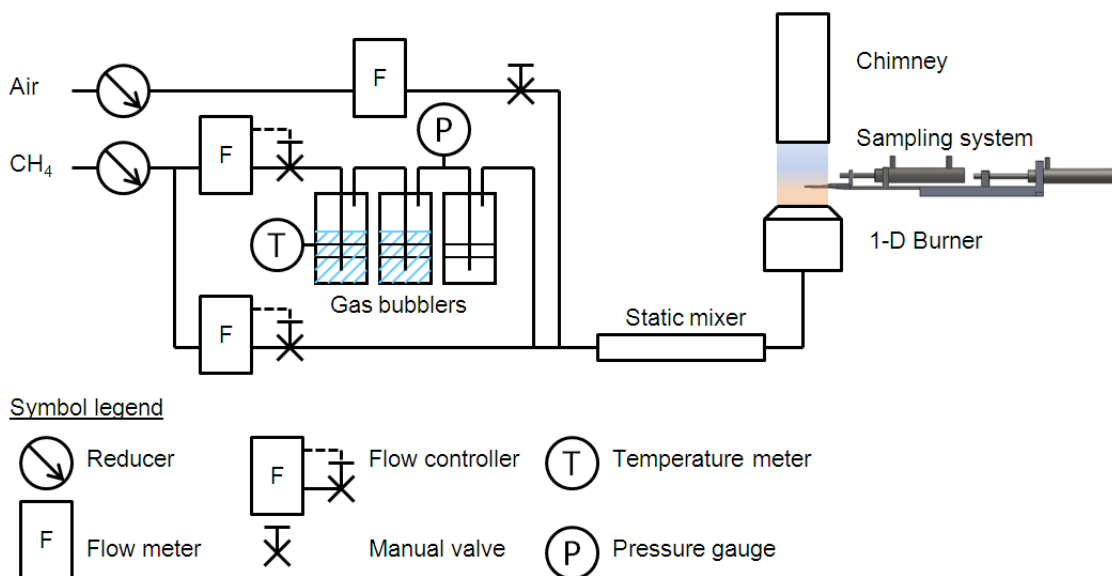


**Figure 9: Gas handling system for the 1-D burner system.**

Custom made pressure resistant gas bubblers are used to introduce siloxanes in the methane gas flow, which was done to simulate the siloxane containing biogas. The temperature and pressure in the gas bubblers is measured using a digital thermometer (Kane-May KM330) and an analog pressure gauge (WIKA Model 232.36). The first two gas bubblers are filled with a liquid siloxane, while the last bubbler is empty to capture siloxane condensate. In this way, the methane gas flowing through the bubblers is saturated with siloxanes. The methane flow controllers used are interchangeable allowing for a wide range of siloxane concentrations. The methane and air gas flows are mixed using a static mixing tube to ensure homogeneous mixing.

A photograph of the three gas bubblers containing siloxanes is shown in Figure 10. In this thesis siloxanes D4 (purity 98%, Acros Organics), D5 (purity 97%, Aldrich Chemistry) and L2 (purity 98+%, Acros Organics) were used for the experiments.



**Figure 10: Photograph of the custom made pressure resistant gas bubblers containing a liquid siloxane used to introduce siloxanes in methane.**

The concentration of siloxanes in methane leaving the gas bubblers,  $C$  in  $\text{g/m}^3_n$  can be calculated using equation (2). In equation (2) the concentration is first determined using the ideal gas law ( $n/V = p/R \cdot T$ ) multiplied by the molar mass of the siloxanes (see also Table 1) in the gas bubbler. To account for the pressure above atmospheric in the gas bubblers a correction factor is used (CF), which equals the atmospheric pressure divided by the pressure in the bubblers. The mixture leaving the gas bubblers is saturated with siloxanes and can be diluted with pure methane to obtain the desired concentration.

$$C = CF \cdot \frac{P_{\text{vap}}(T)}{T_N \cdot R} \cdot M_{\text{silox}} = \frac{P_N}{P_{\text{exp}}} \cdot \frac{P_{\text{vap}}(T)}{T_N \cdot R} \cdot M_{\text{silox}} \quad (2)$$

where  $P_{\text{vap}}(T)$  is the vapor pressure of the siloxane in the gas bubblers at a given temperature,  $P_{\text{exp}}$  is the pressure in the gas bubblers and  $P_N$  is the atmospheric pressure of 101325 Pa.  $T_N$  is the normalized temperature of 273 K,  $R$  is the ideal gas constant of  $8.314 \text{ J} \cdot \text{mol}^{-1} \cdot \text{K}^{-1}$  and  $M_{\text{silox}}$  the molar mass in g/mole of the siloxane in the gas bubblers.

To verify if the concentration calculated with equation (2) is the actual concentration during experiments (i.e. if the methane leaving the gas bubblers is saturated with siloxanes), the average siloxane concentration was also gravimetrically determined, using a Mettler Toledo P83002-S/FACT balance with a reproducibility of 0.1 g. This is done by weighing the gas bubblers before and after the experiment. Since the flow through the gas bubblers is

known the difference in weight yields the siloxane concentration. Equation (3) is used to determine the siloxane concentration gravimetrically.

$$C = \frac{m_1 - m_2}{t \cdot \phi_v} \quad (3)$$

here  $\phi_v$  is the volumetric flow rate through the gas bubblers in  $\text{m}^3/\text{min}$ ,  $t$  is the duration of the experiment in min,  $m_1$  is the mass of the gas bubblers before the experiment in g and  $m_2$  is the mass of the gas bubblers after the experiment in g. In Appendix I experiments are described in which concentrations calculated with equation (2) and equation (3) are compared for siloxanes L2, D4 and D5. Based on these experiments we assume that methane leaving the gas bubblers is saturated with siloxanes for each methane flow used in this thesis.

### 3.1.3 Localized thermophoretic sampling system

Silica particles in the flame at various positions were sampled by introduction of a probe holding a thin carbon coated copper grid ( $\varnothing=3$  mm) in the flame. The probe was rapidly inserted in the flame by a nitrogen driven double acting pneumatic cylinder mounted on a rail. To avoid sampling particles from the outermost areas of the flame, the grid was shielded during flame entry. This is necessary because at the outermost areas of the flame a temperature gradient is present which has a large influence on the growth of silica particles. A second double acting pneumatic cylinder removes the shield for a short time period to allow the grid to sample silica particles. The system used in this thesis is based on the system of J. Lee, I. Altman and M. Choi [17] and is shown schematically in Figure 11. The working principle of the sampling system is based on thermophoresis (see chapter 5 for details): because of the temperature difference between the hot surrounding gas molecules and the relatively cold grid, silica particles diffuse to the grid. The larger the temperature difference between the grid and the surrounding gas molecules, the larger the thermophoretic force applied to the particles.

Experiments reveal that the sampling times used in this thesis were sufficient to collect a substantial amount of particles due to thermophoresis but insufficient to damage the grid. An electronic circuit capable of producing pulses 50 – 1000 ms in length controls solenoid valves used to relay pressure to the pneumatic cylinders. A precise oscilloscope (100 MHz Agilent 54622A) determined the pulse duration, which is assumed to be equal to the sampling time. To study the particle growth at different positions in the flame, the burner was moved vertically along the sampling system with a precision of 0.1 mm.

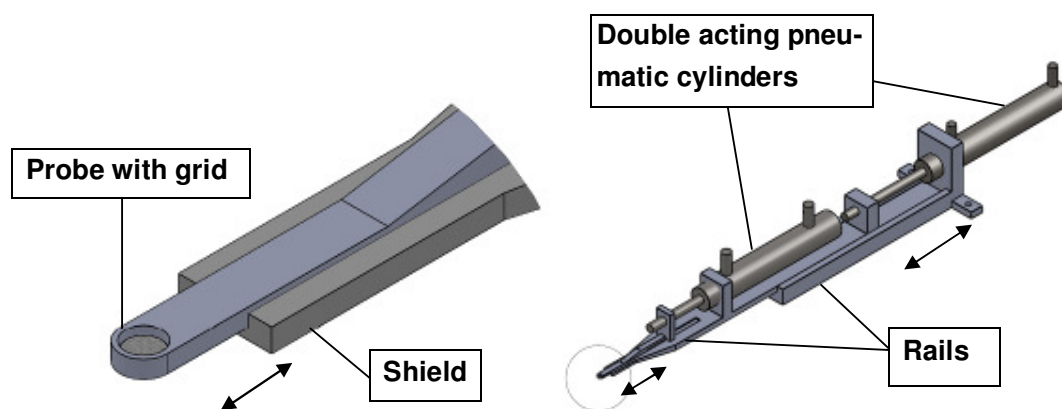


**Figure 11: Localized thermophoretic sampling system, schematic on the right and a detailed schematic of the probe and shield on the left.**

The design of the sampling probe containing the grid was optimized to sample silica particles which are representative for particles in the flame in terms of morphology and size. The probe optimization is discussed in more detail in Appendix II.

A Transmission Electron Microscope (TEM) has been used to analyze samples (grids) taken in flames with varying parameters at different distances above the burner surface. The microscope used for samples taken in this study was a Jeol 2010F electron microscope operated at 200 kV located at the University of Groningen. With the TEM an electron beam is transmitted through a thin specimen, in this case the grid containing the silica particles. Electrons interacting with the specimen are focused on an imaging device from which a TEM image can be extracted. With the TEM setup used in this study, silica particles as small as 3 nm can be distinguished on the TEM images. Figure 12 shows two examples of TEM images with silica particles on grids which were sampled using the thermophoretic sampling system.

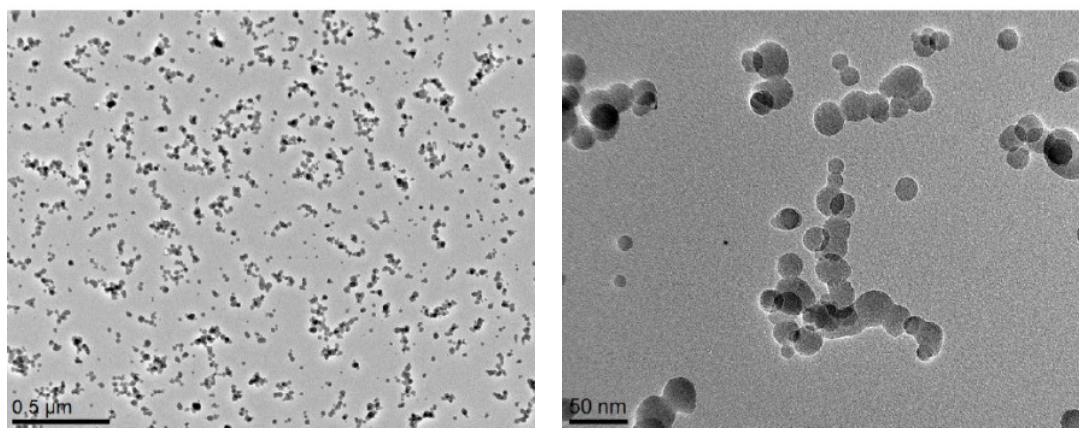


**Figure 12: Examples of TEM images at two different levels of magnification. These samples were taken in a  $\dot{p}v=0.038 \text{ g/cm}^2\cdot\text{s}$  stoichiometric laminar premixed  $\text{CH}_4/\text{L}_2/\text{air}$  ( $19 \text{ g/m}^3$   $\text{n L}_2$ ) flame at a distance above the burner surface of 200 mm.**

The University of Groningen has analyzed the particles shown in Figure 12 on their composition: the ratio between Si and O molecules in the particles was 1:2 which confirms

that they are silica particles. The method used to determine this ratio was energy dispersive x-ray spectroscopy (EDX or EDS).

## 3.2 Experimental results and discussion

### 3.2.1 Silica yield experiment

According to equilibrium calculations all silicon present in siloxanes should be converted to either  $\text{SiO}$  or  $\text{SiO}_2$  upon combustion. After cooling, all silicon is assumed to be present in the form of  $\text{SiO}_2$  (s). To confirm these calculations and assumptions a silica yield experiment was performed. This was done by using the gas handling system as described in paragraph 3.1.2 with the ceramic tile burner in combination with a long chimney. On top of the chimney a High Efficiency Particulate Air (HEPA) filter (H13, Camfil Farr) is installed which is capable of filtering particles of any size with an efficiency of at least 99.95 %. The chimney covers most of the burner including its stainless steel housing which has enough height (1.5 m) to avoid overheating of the HEPA filter situated on top of the chimney. A photograph of the experimental setup containing the ceramic tile burner, the chimney and the HEPA filter is shown in Figure 13.

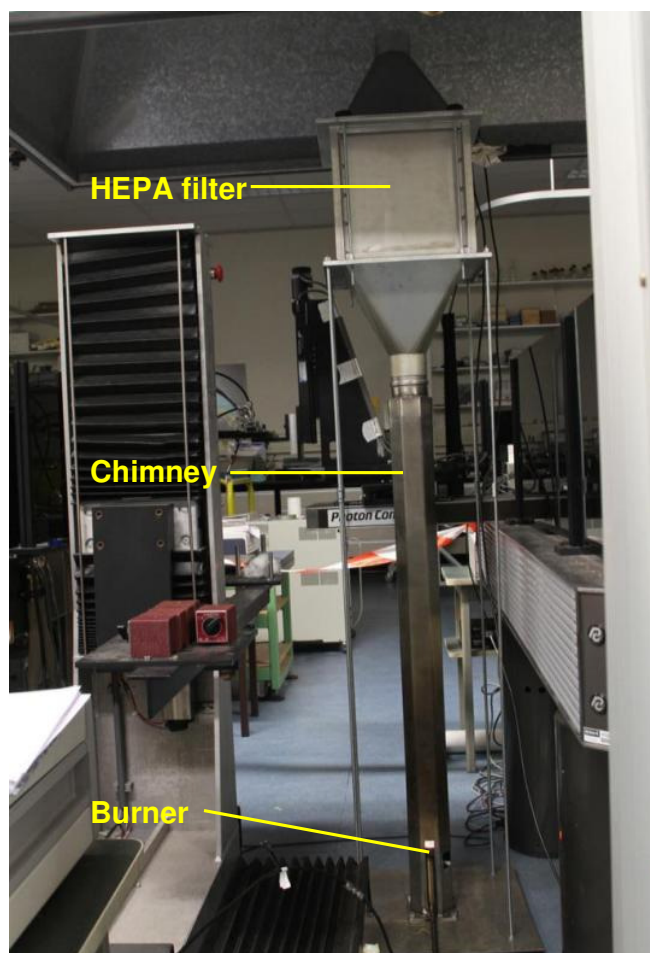
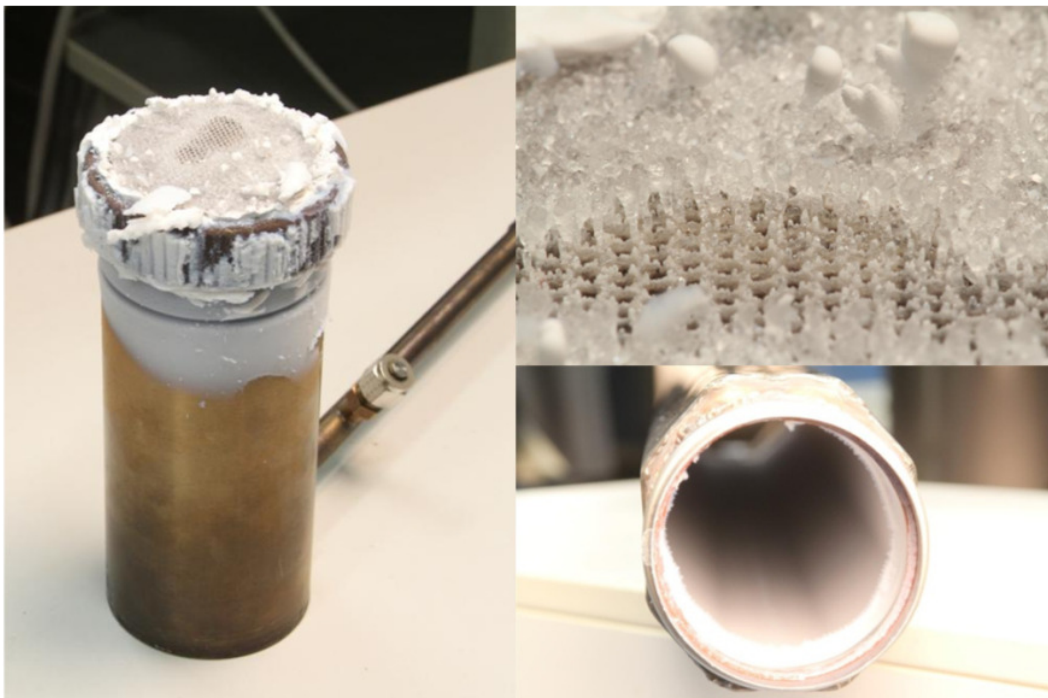


Figure 13: Photograph of the experimental setup for the silica yield experiment.



Since the chimney contains the flame, silica particles can only deposit inside the chimney, in the HEPA filter or on the burner itself. Therefore by weighing all these components before and after the experiments, the difference in mass yields the amount of produced silica. This amount can be compared to the expected amount of silica assuming that all siloxanes are converted to silica. The balance used to weigh each individual component is a PRECISA 480 (reproducibility=0.3 g). Each component is dried with ambient air before it is weighed.

The yield of silica from siloxanes was determined using a stoichiometric  $p \cdot v = 0.023 \text{ g/cm}^2 \cdot \text{s}$  flame with an L2 concentration of  $191 \text{ g/m}^3$ . The duration of the experiment was 4 hours, after this time the experiment was aborted because the HEPA filter was completely clogged with silica and flue gases started to leave the system through an opening at the bottom of the chimney. Also, the burner surface was almost completely clogged with silica due to the high siloxane concentrations used for a long period of time. Photographs taken of the burner and chimney after the experiment are shown in Figure 14.



**Figure 14: Photographs taken after the silica yield experiment with the burner on the left and a detailed view of the burner surface on the top right. The inside of the chimney, which is partly covered with a uniform layer of silica, is shown on the bottom right.**

The experimental silica yield of deposition was found to be 89%. It should be noted that clogging of the HEPA filter resulted in small leakages of flue gases at the base of the chimney. An analysis of the composition of the white layer on the burner surface confirmed that the layer consists of silica. Within experimental uncertainties, these experiments confirm the assumption from thermodynamic equilibrium calculations that all silicon is converted to

$\text{SiO}_2$  (s). Furthermore since a large quantity of silica was found on the burner surface it follows that silica particles form relatively fast and are present in the flame at short distances above the burner surface.

### 3.2.2 Influence of siloxane concentration on silica particle formation

To determine the influence of the siloxane concentration on silica particle formation in  $\text{CH}_4/\text{siloxane}/\text{air}$  flames the siloxane concentration is varied between  $19 \text{ g/m}^3_n$  and  $191 \text{ g/m}^3_n$  L2 in methane. L2 is used for these experiments because it has a sufficiently high vapor pressure to obtain these high concentrations (see also Table 1). Silica is sampled at 4 mm above the burner surface using a sampling time of 100 ms in a  $\text{pv}=0.028 \text{ g/cm}^2\cdot\text{s}$  stoichiometric laminar premixed  $\text{CH}_4/\text{L2}/\text{air}$  flame (calculated flame temperature of 2050 K at 4 mm above the burner surface, also see paragraph 3.2.4 for temperature calculations). Figure 15 shows the TEM images of samples taken in the flames at different L2 concentrations in methane, the concentrations are shown in the upper left part of the respective TEM images.

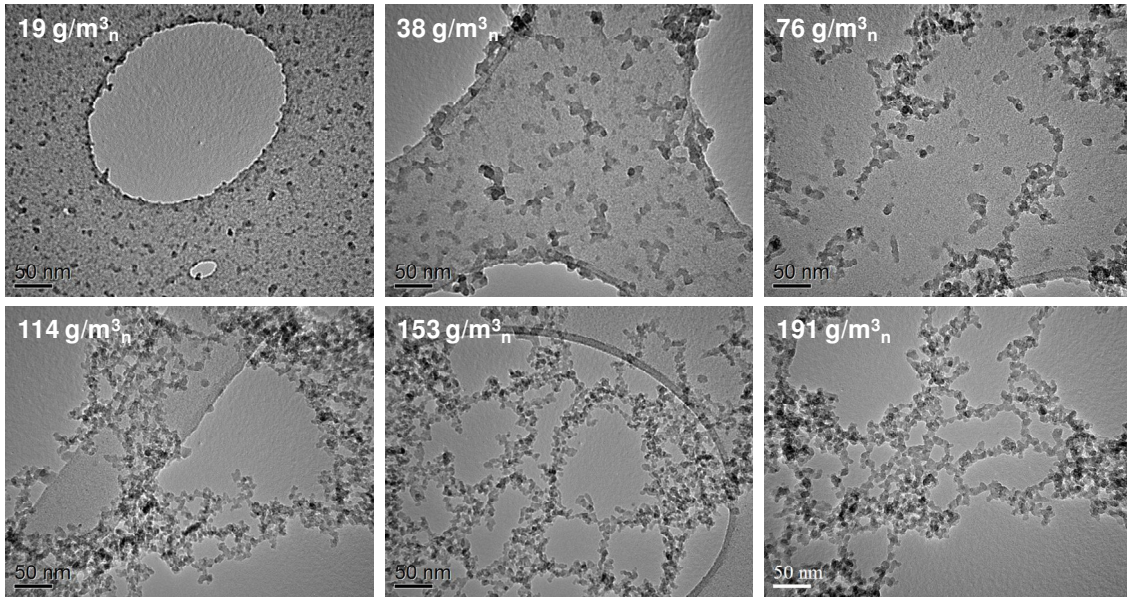


**Figure 15: TEM images from samples taken in a  $\text{pv}=0.028 \text{ g/cm}^2\cdot\text{s}$  stoichiometric laminar premixed  $\text{CH}_4/\text{L2}/\text{air}$  flame, at 4 mm above the burner surface using a 100 ms sampling time at L2 concentrations ranging from  $19 \text{ g/m}^3_n$  to  $191 \text{ g/m}^3_n$  in methane.**

The TEM images shown in Figure 15 confirm that silica particles are already formed close to the burner surface (4 mm) in a flame with a mass flux of  $\text{pv}=0.028 \text{ g/cm}^2\cdot\text{s}$ . From Figure 15 it can be seen that the siloxane concentration has a large influence on the morphology and size of silica particles in the flame. At lower concentrations more individual particles are present, which are called clusters (round silica particles). At higher concentrations silica particles are heavily branched, these particles are called fractal aggregates (multiple clusters) or fractal agglomerates (multiple fractal aggregates) [26]. Also,

the size of particles increases with concentration. Based on these results, we may expect that only small clusters (size in the order of several nanometers) are present in biogas flames (with much lower siloxane concentrations) near the burner surface. It should be noted that on samples taken in flames with siloxane concentrations similar to those found in biogases, no particles were observed. The sizes of particles at these concentrations are likely too small to be distinguished on the TEM images. Therefore, we can only observe trends at increased siloxane concentrations and extrapolate to lower concentrations.

### 3.2.3 Influence of distance above the burner surface on silica particle formation

To follow the development of silica particles in flames several samples of silica particles are taken at different distances above the burner surface in a  $\dot{p}v=0.028 \text{ g/cm}^2\cdot\text{s}$  stoichiometric laminar premixed  $\text{CH}_4/\text{L2}/\text{air}$  flame. For these experiments, the L2 concentration in methane was kept constant at  $19 \text{ g/m}^3_n$  and the sampling time was 100 ms. Figure 16 shows TEM images of the samples, the distances above the burner surface are shown in the upper left part of the respective TEM images.

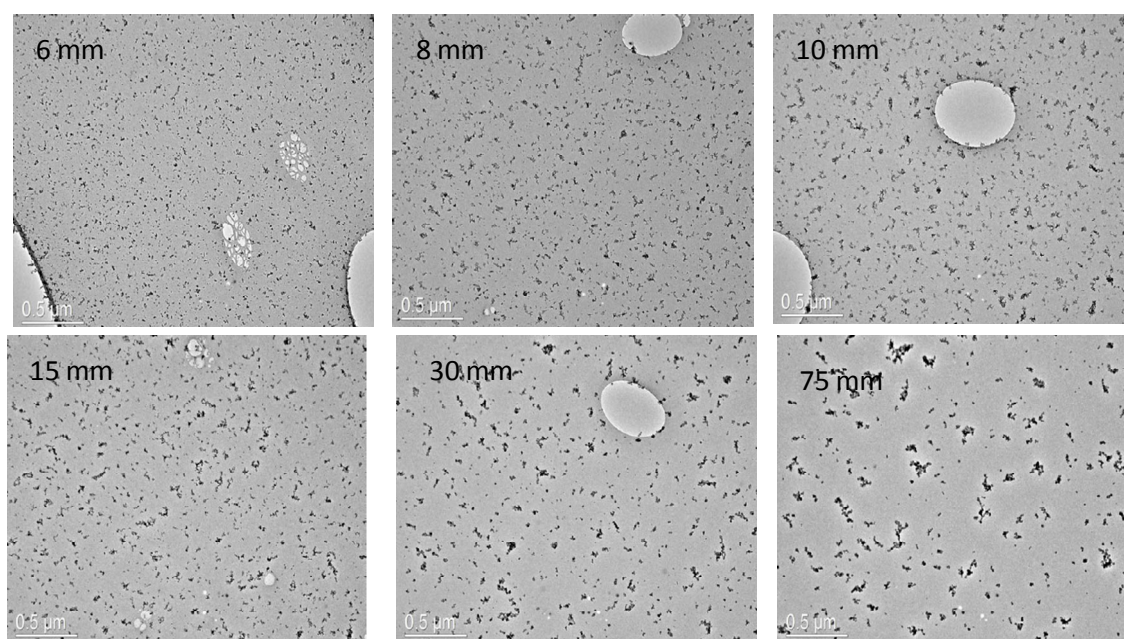


**Figure 16: TEM images from samples taken in a  $\dot{p}v=0.028 \text{ g/cm}^2\cdot\text{s}$  stoichiometric laminar premixed  $\text{CH}_4/\text{L2}/\text{air}$  flame at a concentration of  $19 \text{ g/m}^3_n$  with a 100 ms sampling time at different distances above the burner surface.**

The silica particle size in Figure 16 is increasing with distance, also closer to the burner surface more clusters are formed and further downstream clusters combine to form fractal aggregates. To be able to distinguish individual particles, magnified TEM images from samples taken at different distances above the burner surface in the same flame are shown in Figure 17.



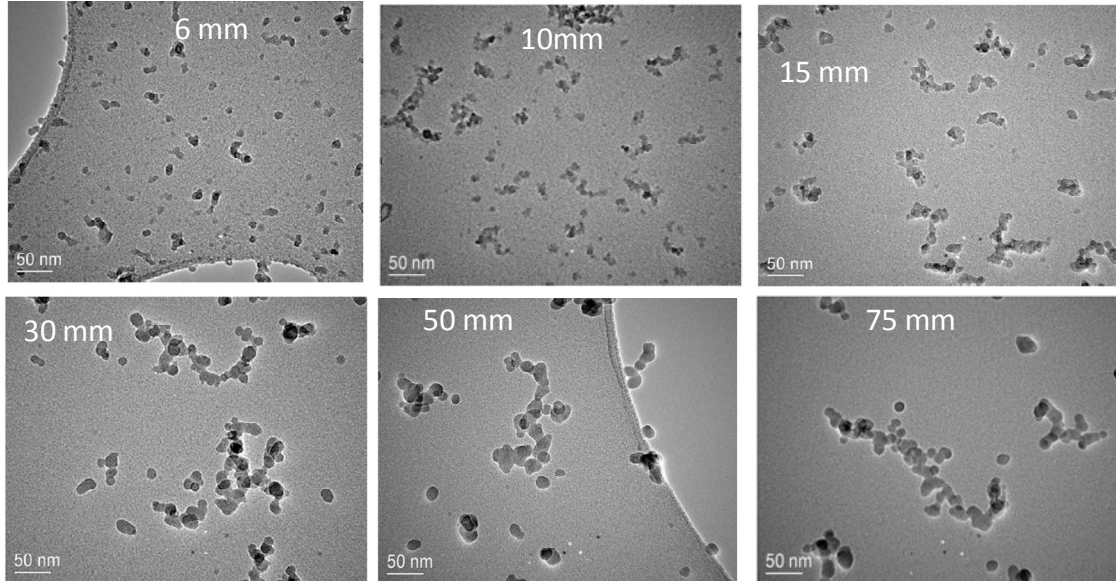


**Figure 17: TEM images with increased magnification from samples taken in a  $\dot{p}v=0.028 \text{ g/cm}^2\cdot\text{s}$  stoichiometric laminar premixed  $\text{CH}_4/\text{L2}/\text{air}$  flame at a L2 concentration of  $19 \text{ g/m}^3$  with a 100 ms sampling time at different distances above the burner surface.**

From samples taken in the  $\dot{p}v=0.028 \text{ g/cm}^2\cdot\text{s}$  stoichiometric laminar premixed  $\text{CH}_4/\text{L2}/\text{air}$  flame, sufficient number of TEM images were acquired to allow the characterization of more than 150 individual fractal aggregates per sample. Image pre-processing and analysis was performed using the MATLAB software package following the procedure described in Ref. [18]. The processing of the images yielded both the radius of gyration  $R_g$  (which is a measure of the size of an object of arbitrary shape and can be calculated from the root mean square distance from the centre of gravity to different parts of the particle) and the mean cluster radius  $a$ . The processing of the TEM images is described in more detail in Appendix III.

Figure 18 shows the experimentally determined mean radius of clusters  $a$ , as a function of distance above the burner surface in the  $\dot{p}v=0.028 \text{ g/cm}^2\cdot\text{s}$  stoichiometric laminar premixed  $\text{CH}_4/\text{L2}/\text{air}$  flame. For the mean cluster sizes in the figure, both individual clusters and clusters inside fractal aggregates are taken into account. At distances from 6 mm above the burner surface upwards the silica particles are mainly fractal aggregates and not many individual clusters are left. Figure 19 shows the experimentally determined mean radius of gyration of fractal aggregates  $R_g$ , as a function of distance above the burner surface in the same flame.

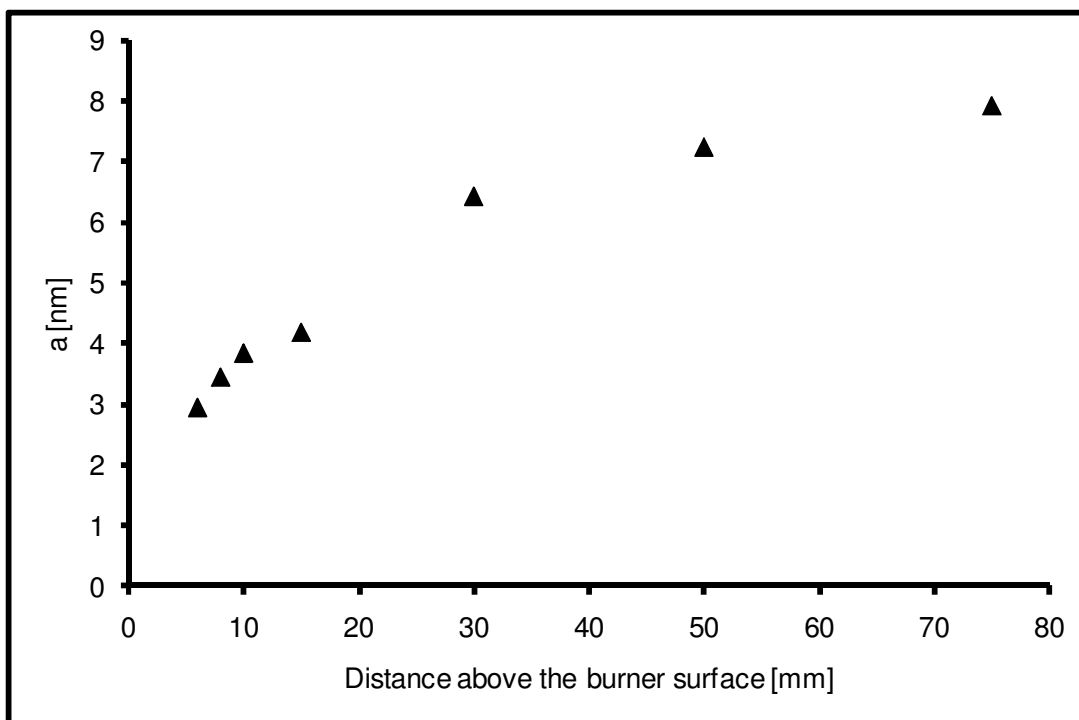


Figure 18: Mean cluster radius ( $a$ ) as a function of distance above the burner surface in a  $\rho v = 0.028 \text{ g/cm}^2 \cdot \text{s}$  stoichiometric laminar premixed  $\text{CH}_4/\text{L2}/\text{air}$  flame.

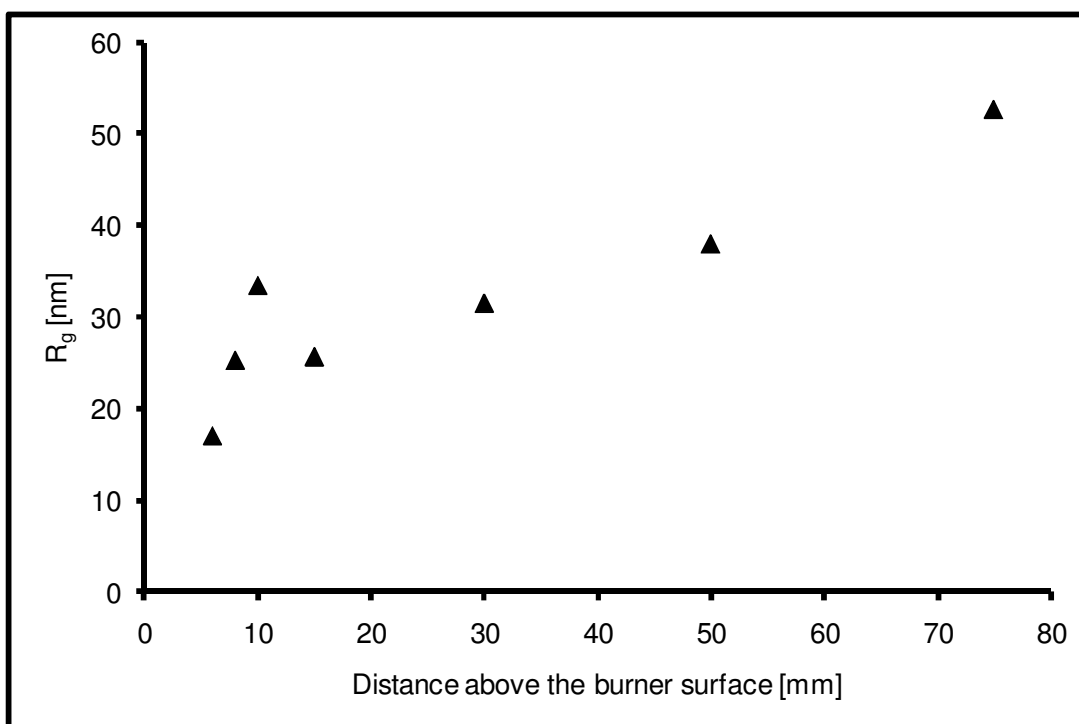
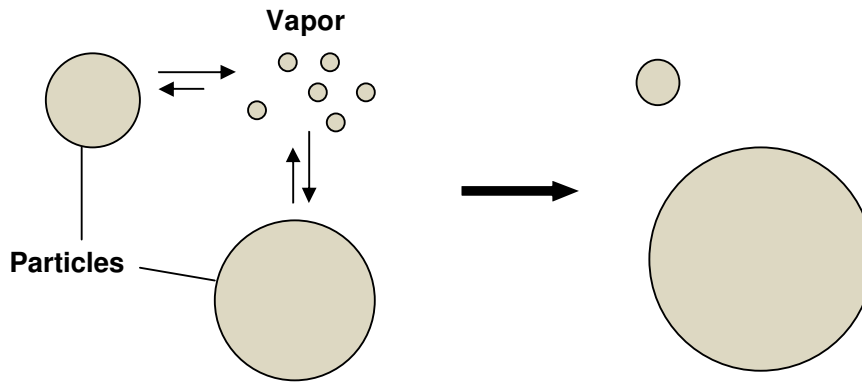


Figure 19: Mean radius of gyration ( $R_g$ ) of fractal aggregates as a function of distance above the burner surface in a  $\rho v = 0.028 \text{ g/cm}^2 \cdot \text{s}$  stoichiometric laminar premixed  $\text{CH}_4/\text{L2}/\text{air}$  flame.

In Figure 18 and Figure 19 it can be seen that not only the size of the silica particles is increasing with distance above the burner surface but also clusters inside fractal aggregates grow. This restructuring of fractal aggregates may be due to Ostwald ripening [20, 21] and due to combination of multiple clusters to one bigger cluster (sintering) inside fractal aggregates. Ostwald ripening results from the equilibrium between particles and their vapor consisting in this case of free  $\text{SiO}_2$  (g) molecules. This vapor is formed as a result of evaporation of particles that leads to equilibrium between particles and the vapor of their molecules together with the process of molecule attachment to particles. Since smaller particles are less stable due to a higher internal pressure compared to bigger particles, Ostwald ripening causes small particles to disappear and bigger particles to grow. This process occurs in general for both individual clusters and clusters inside fractal aggregates since most of the surface area of clusters inside fractal aggregates is exposed to the surroundings [26]. The process of Ostwald ripening is illustrated in Figure 20.



**Figure 20: Schematic overview of particle growth via the process of Ostwald ripening.**

The degree of branching of fractal aggregates is described by the fractal dimension,  $D$ . We determine the fractal dimension of the forming fractal aggregates by the standard method [22, 23, 24, 25] based on the dependence of the number of monomers in fractal aggregates on their gyration radius. The number of clusters in a fractal aggregate  $n_c$ , fits linearly with the ratio of the gyration radius to the radius of monomers in the logarithmic scale that allows for the determination of the fractal dimension, see equation (4).

$$n_c = \left( \frac{R_g}{a} \right)^D \quad (4)$$

From equation (4) we can deduce the fractal dimension, this is shown in Figure 21.

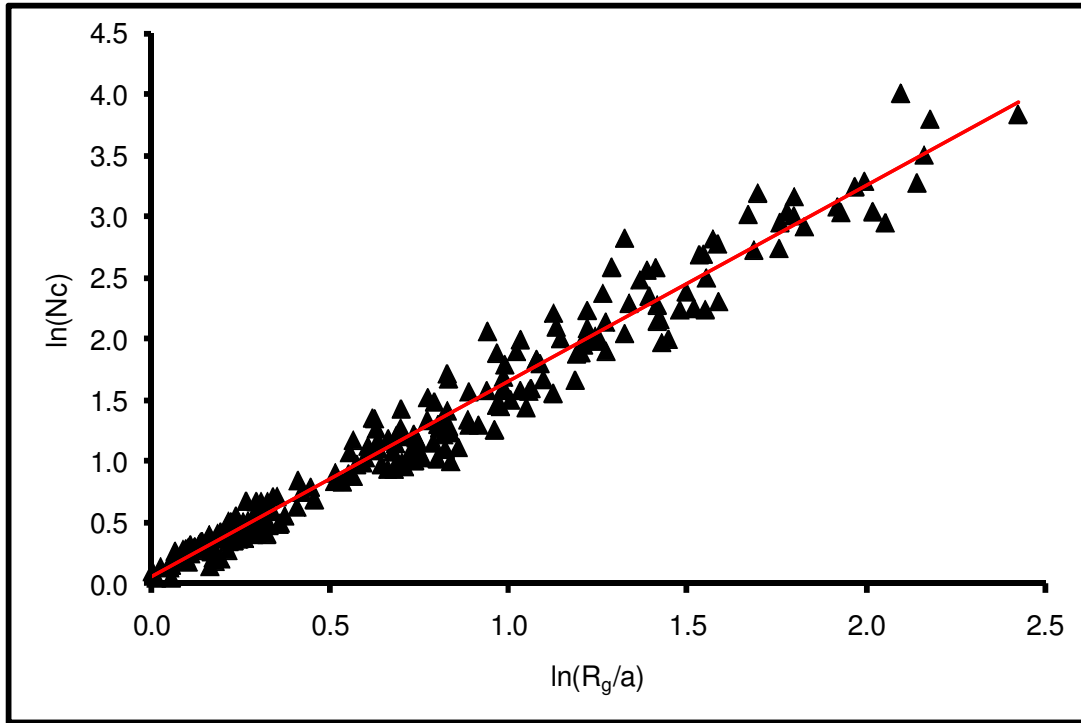


**Figure 21: Determination of the fractal dimension of fractal aggregates using the standard method.**

From the fit shown in the figure above, a fractal dimension of  $D=1.60$  ( $\pm 0.06$ ) is found. In paragraph 3.2.5, the fractal dimension is used as an input parameter to determine the growth of fractal aggregates. It should be noted that the fractal dimension is expected to increase with a decreasing initial siloxane concentration and an increasing temperature. The dependency of the initial siloxane concentration on fractal dimension (using the standard method) in the  $p_v=0.028$  g/cm<sup>2</sup>·s stoichiometric laminar premixed CH<sub>4</sub>/L2/air flame is currently being studied at the University of Groningen. The influence of temperature on the fractal dimension is discussed later in this paragraph.

As can be seen in Figure 18, the growth of clusters inside fractal aggregates appears to occur fast up to 30 mm for  $p_v=0.028$  g/cm<sup>2</sup>·s flames, while above 30 mm the cluster growth slows down. There may be two explanations for this behavior. The first involves the presence of free SiO<sub>2</sub> (g) molecules in the flame. In the reaction zone many free SiO<sub>2</sub> (g) molecules are formed creating a supersaturated SiO<sub>2</sub> vapor. This vapor is rapidly converted to nanoclusters via nucleation processes. It should be noted that the rate of Ostwald ripening is proportional to the number density of free SiO<sub>2</sub> molecules. Therefore, it proceeds faster in the lower regions of the flame near the reaction zone. The second explanation for the decrease in the rate of fractal aggregate restructuring involves sintering. When two equally sized particles are attached to each other sintering can be described with Frenkel's model. This model is valid for amorphous structures when sintering occurs via viscous flow. The structure of silica particles sampled in this thesis was analyzed using a high resolution TEM. The analysis yielded that the silica particles had an amorphous structure. In literature, the

structure of silica produced in flames is also reported to be amorphous [27]. Since the silica particles are amorphous, we may apply Frenkel's model. In Frenkel's model sintering of two particles occurs via equation (5) [28].

$$x^2 = \frac{3 \cdot \gamma(T) \cdot a_0 \cdot t}{2 \cdot \eta(T)} \quad (5)$$

where  $x^2$  is the square radius of the contact area (or the extent of sintering),  $\gamma$  is the surface tension,  $a_0$  the radius of the initial particles before sintering,  $t$  is the time after initial contact between the particles and  $\eta$  is the dynamic viscosity of the particles. The sintering time ( $t_s$ ) can be obtained when  $x=a$  ( $a$  is the cluster radius after sintering), and from  $2 \cdot V_0 = 2 \cdot (4 \cdot \pi \cdot a_0^3 / 3) = V = 4 \cdot \pi \cdot a^3 / 3$  it follows that  $a = 2^{1/3} \cdot a_0$  so after rearranging equation (5) we find equation (6).

$$t_s = \frac{2 \cdot 2^{2/3} \cdot a_0 \cdot \eta(T)}{3 \cdot \gamma(T)} \approx \frac{a_0 \cdot \eta(T)}{\gamma(T)} \quad (6)$$

According to equation (6) the sintering time increases with initial cluster radius, which is in correspondence with the observations made in Figure 17 and Figure 18. Clearly as described before, the sintering time, which is dependent on temperature (via the viscosity and the surface tension), influences the fractal dimension (increasing  $D$  with decreasing  $t_s$ ) of silica particles in the flame.

It should be noted that Frenkel's model is based on studies in which particles are in intimate contact with each other. This is the case in the restructuring of fractal aggregates at larger distances above the burner surface (see for example Figures 16 and 17). When considering the growth of clusters close to the burner surface via sintering mechanisms (i.e. cluster collision followed by sintering) the probability that two clusters stick to each other after a collision is important for the average growth rate of clusters in the flame. This probability is proportional to the reciprocal surface tension, the reciprocal dynamic viscosity, the contact time  $t_c$ , and the initial cluster radius [28], as can be seen from equation (7). It should be noted that this equation is also valid for the formation of fractal aggregates.

$$x_{\text{start}}^2 \sim \frac{a_0 \cdot t_c}{\gamma(T) \cdot \eta(T)} \quad (7)$$

At the initial contact of clusters a higher surface tension reduces the amount of liquid that wets the adjacent surface reducing the probability that clusters adhere. After the formation of a bridge between the clusters, surface tension pulls clusters together. With increasing surface tension the pulling force between clusters increases, reducing the sintering time [28]. The influence of surface tension may therefore either have an increasing or decreasing effect on the average cluster growth depending on which process (initial probability of adherence or sintering time) is dominant. An increased viscosity has a decreasing effect on the cluster growth rate in all regions of the flame. It should be noted that both surface tension

and viscosity decrease with temperature. In the next paragraph the influence of flame temperature on silica particle formation is discussed.

### 3.2.4 Influence of flame temperature on silica particle formation

To determine the influence of the temperature on the silica particle formation the mass flux of the flame is varied between  $\dot{m} = 0.008 \text{ g/cm}^2\cdot\text{s}$  and  $\dot{m} = 0.038 \text{ g/cm}^2\cdot\text{s}$ . The calculated flame temperatures at different positions in these flames are compared with measured temperatures. The temperatures were measured using an optical non-intrusive in-situ measurement technique with an accuracy of 50 K [29, 32]. Figure 22 shows calculated temperature profiles of several mass fluxes as solid lines and measured temperature profiles as dotted lines of the same color. The calculations assume that no heat losses occur to the surroundings, therefore the calculated temperatures remain constant in the post flame zone. In practice heat losses do occur, therefore the measured temperatures decrease downstream.

In Figure 22 it can be seen that the measured temperatures nearly overlap with the calculated temperatures near the burner surface. Further downstream heat losses increase and the difference between calculations and measurements become larger.

Based on calculated temperatures the residence times as a function of distance above the burner surface for 4 mass fluxes are shown in Figure 23. In this figure, it can be seen that higher mass fluxes lead to shorter residence times.

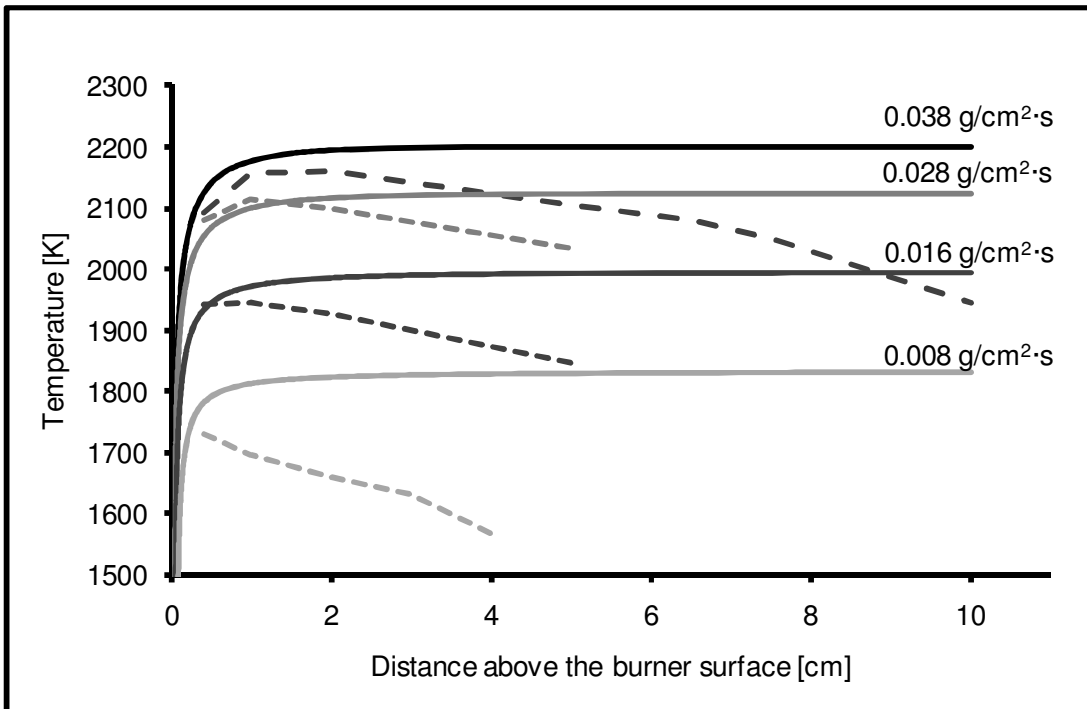
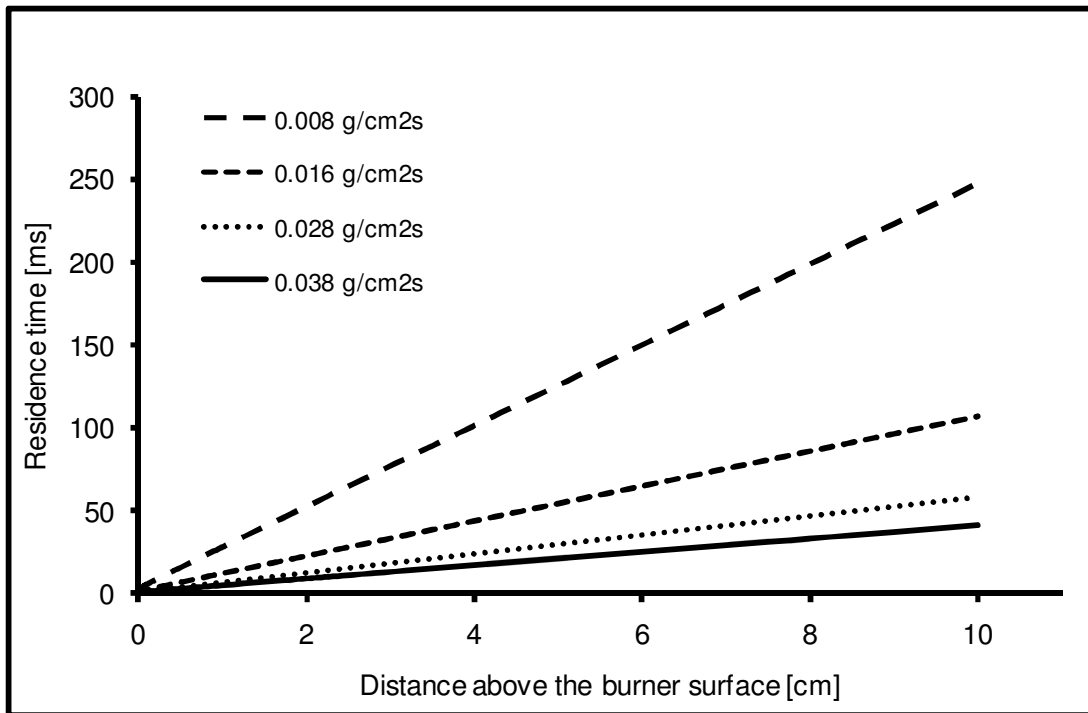


Figure 22: Calculated temperature profiles (solid lines) and measured temperature profiles (dotted lines of the same shade of grey) in stoichiometric laminar premixed  $\text{CH}_4/\text{air}$  flames with a measured accuracy of 50 K.

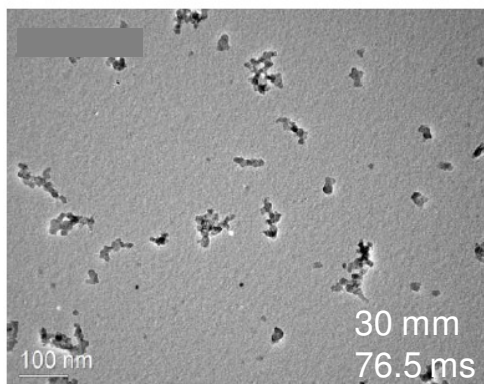
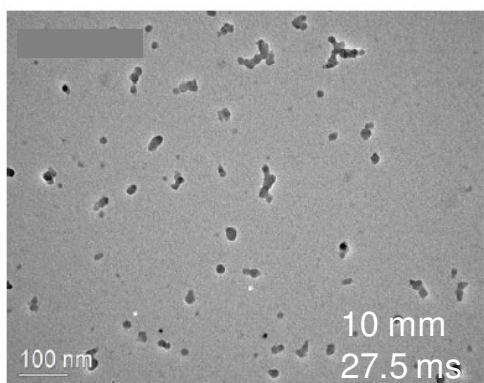
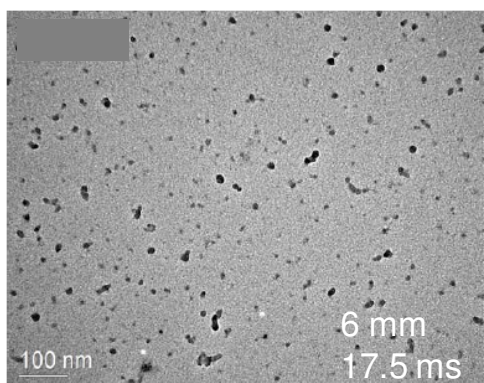
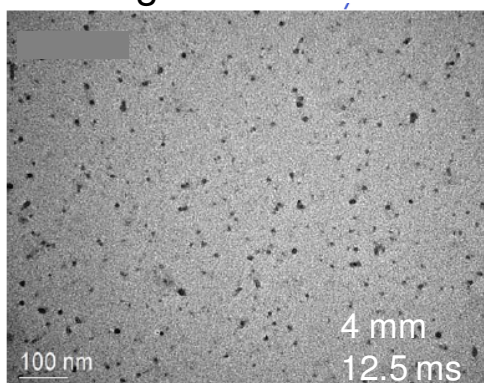


**Figure 23: Residence time as a function of distance above the burner surface in stoichiometric laminar premixed CH<sub>4</sub>/air flames with different mass fluxes.**

In Figure 24 TEM images are shown from samples taken from flames with  $\rho v = 0.008$  g/cm<sup>2</sup>·s and  $\rho v = 0.038$  g/cm<sup>2</sup>·s with an almost constant residence time and an L2 concentration of 19 g/m<sup>3</sup> in methane. To determine the influence of temperature on silica particle formation the flame temperature is varied over a range of about 400 K.



0.008 g/cm<sup>2</sup>·s



0.038 g/cm<sup>2</sup>·s

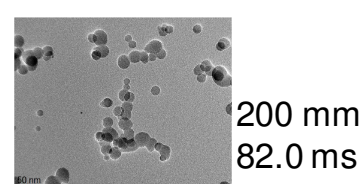
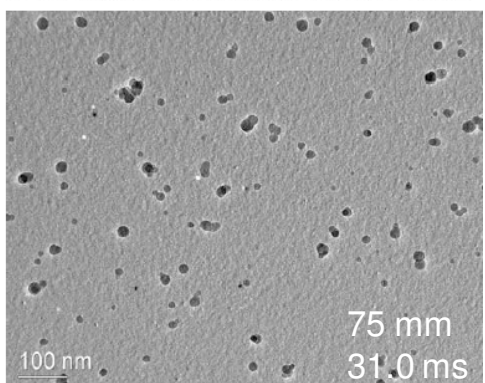
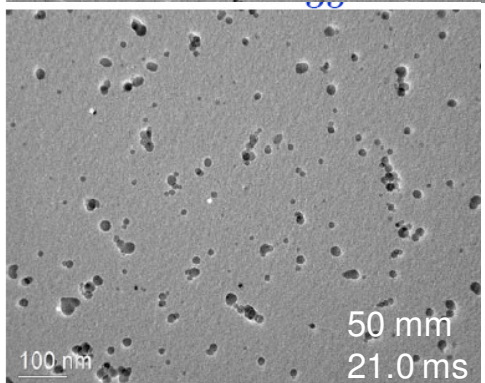
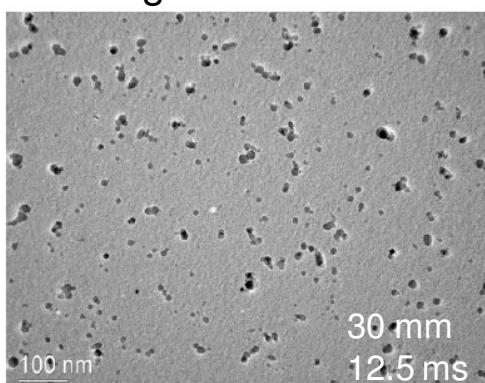


**Figure 24:** TEM images of silica sampled in a  $\rho v=0.008$  g/cm<sup>2</sup>·s stoichiometric laminar premixed CH<sub>4</sub>/L2/air flame on the left and  $\rho v=0.038$  g/cm<sup>2</sup>·s on the right. The image on the bottom right has the same scale as the other pictures for direct comparison of particle sizes.



As previously discussed in paragraph 3.2.3, the TEM images in Figure 24, show an increase in silica particle size as a function of residence time. Both individual clusters and clusters inside fractal aggregates grow. Also, in a comparison between the different mass flow rates in Figure 24 the cluster growth is faster at higher temperatures (i.e. the clusters are bigger at higher temperatures with the same residence time). The increased size of clusters may be due to a decreased viscosity or surface tension at higher temperatures. A decrease in viscosity increases the average cluster growth rate both for clusters inside fractal aggregates and individual clusters (see paragraph 3.2.3). Also, the size of particles in general is larger at higher temperatures, which may be caused by a decreased viscosity (see paragraph 3.2.3) or higher energy collisions. This increases the probability that clusters stick together after collisions resulting in larger clusters and aggregates. In paragraph 3.2.5 the average silica particle growth is described with growth models.

### **3.2.5 Silica particle formation models**

The combined experimental and theoretical studies of growth of silica particles in flames allow us to understand in more detail, the chain of processes leading to the formation of silica in flames. In the reaction zone of the flame siloxanes are quickly converted to  $\text{SiO}$  (g) and  $\text{SiO}_2$  (g) creating a supersaturated vapor. Nucleation of silica molecules causes nanoclusters to appear in the early stages of the flame. At high temperatures the nanoclusters will continue to grow into larger clusters by taking up free  $\text{SiO}_2$  (g) molecules.  $\text{SiO}$  (g) is further oxidized to  $\text{SiO}_2$  as  $\text{SiO}_2$  is removed from the gas phase. The partition between these species depends on temperature (analogous to  $\text{CO}/\text{CO}_2$ ). Growth of clusters also occurs via sintering. The rate of sintering depends on the temperature via the temperature dependence of the viscosity and surface tension (equation (5)). Fractal aggregates grow only due to collisions between particles. Whether cluster growth or fractal aggregate growth is the dominant process depends on the temperature and the concentration. An increased temperature favors the cluster growth process (via surface tension and viscosity) and an increased concentration favors the fractal aggregate growth process (via an increased number of collisions between particles).

In experimental burners and domestic appliances the temperature decreases downstream due to heat losses to the environment. Here different growth processes can be dominant at different positions in the flame depending on the temperature and concentration. Figure 25 shows a generic illustration [15] of the morphologies of particles at different positions in a flame. Note that the temperature profile is shown on the left of the picture. Typical sizes of clusters are in the order of several nm, fractal aggregates are of a size in the order of 100 nm and agglomerates form with a size up to 10  $\mu\text{m}$  [15].

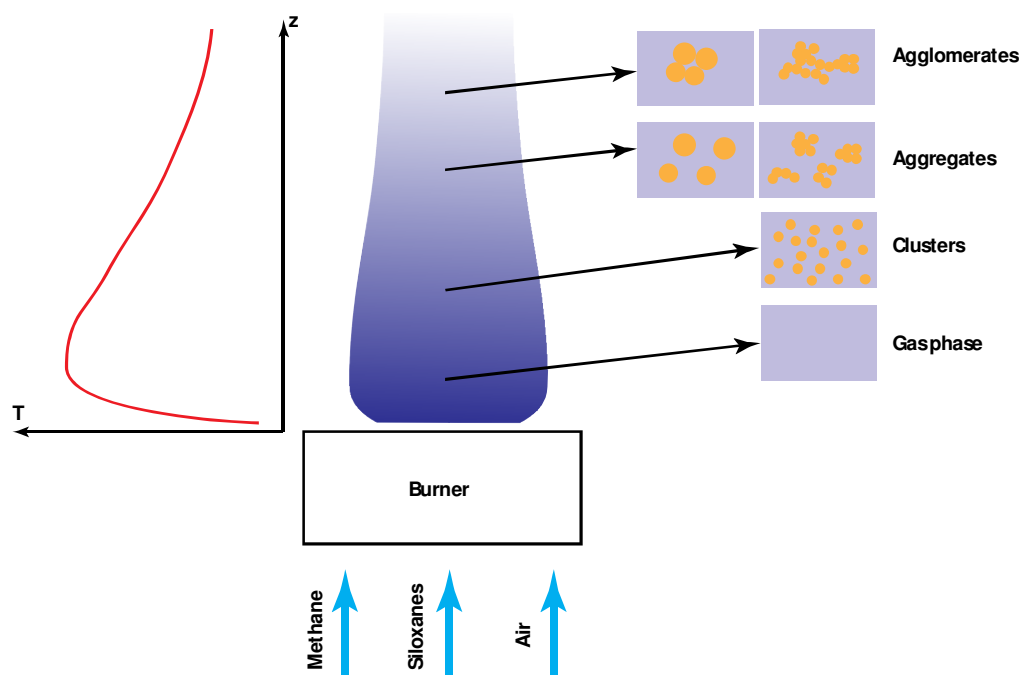


**Figure 25: Growth of silica downstream in an experimental burner [15].**

To describe the average growth of silica particles in a flame different processes of particle growth are bundled in simplified equations. Two regions are distinguished in a flame, the cluster growth region where only clusters are present and the fractal aggregate growth region where fractal aggregates are present. In the subparagraph 3.2.5.1 the cluster growth region is described and in subparagraph 3.2.5.2 the fractal aggregate growth region is described. Based on the experiments performed in this chapter we may assume that the position of the boundary between the cluster growth and fractal aggregate growth regions depends on flame temperature and concentration. In a particular flame system, the position of this boundary should be determined experimentally. An alternative is to perform a study in which temperature and initial siloxane concentration are varied to determine the position of the boundary. Such a study lies outside the scope of this thesis however.

It should be noted that in reality particle growth is a competition between formation of aggregates and the restructuring of these aggregates into clusters. The equations in the following paragraphs can therefore be considered approximations.

### **3.2.5.1 Cluster growth region**

The growth of silica clusters is first considered in flames. The cluster growth occurs in the so-called diffusion regime when the average distance between clusters is small compared to the mean free path of the clusters [33]. Furthermore, the diffusive motion of an individual cluster is considered to be in the binary collision approximation. In this approximation when a cluster interacts with only one buffer gas molecule it changes direction due to the collision and will traverse space between molecules in a straight trajectory. The binary collision

approximation is valid when the cluster radius is small compared to the mean free path of the surrounding gas molecules [26].

To describe cluster growth in this subparagraph, we follow the procedure of Ref. [26] where first the association rate of clusters,  $k_{as}$  in  $\text{m}^3/\text{s}$  at high temperatures is described by equation (8).

$$k_{as} = \frac{3}{n \cdot a} \sqrt{\frac{2 \cdot \pi \cdot T \cdot k_B \cdot N_A}{M}} \quad (8)$$

here  $n$  is the number density of gas molecules in  $\text{m}^{-3}$ ,  $a$  is the (nano)cluster radius in  $\text{m}$ ,  $T$  is de gas temperature in  $\text{K}$ ,  $k_B$  is the Boltzmann constant in  $\text{J/K}$ ,  $N_A$  is Avogadro's number in  $\text{mol}^{-1}$  and  $M$  is the average molecular mass of the surrounding gas molecules in  $\text{kg/mol}$ . To determine the overall average growth of liquid clusters due to sintering, balance equation (9) should be solved [26].

$$\frac{d\bar{n}}{dt} = \frac{1}{2} \cdot k_{as} \cdot n \cdot c \quad (9)$$

where  $\bar{n}$  is the average number of silica molecules in each cluster and  $c$  is the fraction of bound  $\text{SiO}_2$  molecules. The average number of cluster molecules  $\bar{n}$  is related to the cluster radius  $a$ , as  $\bar{n} = (a/r)^3$ , where  $r$  is the molecular radius ( $2.2 \cdot 10^{-10} \text{ m}$  for  $\text{SiO}_2$ ) [26]. The solution of the balance equation (9) gives the average number of  $\text{SiO}_2$  molecules in a cluster as can be seen in equation (10) [26].

$$\bar{n} = \frac{2}{3} \cdot n \cdot c \cdot k_{as}(a) \cdot t_s \quad (10)$$

here  $t_s$  is the elapsed time in which cluster sintering can occur. It should be noted that in equation (10) it is assumed that after cluster collisions the formation of a new cluster is instantaneous. Also, the probability that clusters adhere to each other after collisions is assumed to be 100%, in reality this probability depends upon the viscosity and surface tension of the particles (see also paragraph 3.2.3).

To perform a model to experiment comparison calculated sizes of clusters are compared with the experimentally determined sizes from the  $p_v=0.028 \text{ g/cm}^2 \cdot \text{s}$  stoichiometric laminar premixed  $\text{CH}_4/\text{L2}/\text{air}$  flame previously described in paragraph 3.2.3. The siloxane concentration for this flame was  $19 \text{ g/m}^3_n$  L2 in methane. As initial input particle size the radius of a single silica molecule ( $2.2 \cdot 10^{-10} \text{ m}$  [26]) is used. The temperature profile and velocity profile to determine the residence time in the flame were calculated using PREMIX. Figure 26 shows the calculated cluster size as a function of distance from the burner surface.

The experimentally determined cluster sizes in Figure 26 are almost an order of magnitude smaller than the modeled sizes. Apparently the  $p_v=0.028 \text{ g/cm}^2 \cdot \text{s}$  flame is mainly

in the fractal aggregate growth region and not in the cluster growth region. Therefore, the equations used to determine the cluster sizes may not be applied. The same conclusion can be drawn from Figure 15 and Figure 16 in which the TEM images taken in this flame show mainly fractal aggregates. The formulae in this paragraph to determine cluster growth are based on collisions between clusters. Also, the assumption is made that colliding clusters instantly form a new cluster. In order to study if the model to describe cluster growth is correct, sintering times should be short, i.e. the flame temperature should be sufficiently high so that growth is limited by collisions between clusters. Further research is needed to study if the model to describe cluster growth is correct in a higher temperature flame using the standard method to determine cluster sizes. Since the standard method used to determine the cluster sizes is time consuming this research has not been performed for this thesis. It should be noted that the  $p_v=0.028 \text{ g/cm}^2\cdot\text{s}$  flame has a maximum temperature of approximately 2100 K (also see Figure 22). This is above the melting point of silica, where one might expect cluster growth to be the dominant process. This further emphasizes that a more extensive study is needed to determine the boundary between the cluster growth region and fractal aggregate growth regions depending on temperature and concentration.

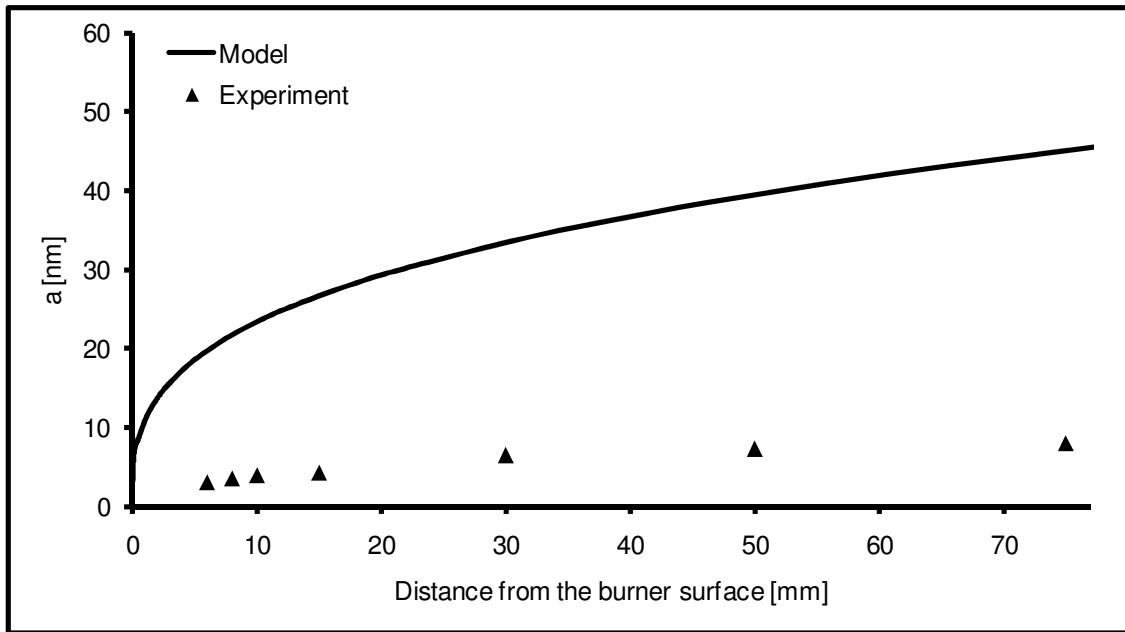


**Figure 26: Modeled cluster sizes as function of distance from the burner surface in a  $p_v=0.028 \text{ g/cm}^2\cdot\text{s}$  stoichiometric laminar premixed  $\text{CH}_4/\text{L2}/\text{air}$  flame.**

### 3.2.5.2 Fractal aggregate growth region

The next stage of growth takes place when the clusters leave the cluster growth region and enter the fractal aggregate growth region. Here collisions between clusters lead to the formation of fractal aggregates. The assumption is made that all clusters are of the same diameter whilst entering the cold flame region. This assumption is considered a rough

approximation therefore the next evaluations have a qualitative character and may be considered as estimations [26].

The growth of fractal aggregates is assumed to occur via the cluster-cluster mechanism [30, 31]. In this case clusters combine to form small aggregates and small aggregates combine to form larger aggregates or agglomerates. The growth of fractal aggregates can be described by using equation (11) which is similar to equation (10) but taking into account the fractal dimension of fractal aggregates [26].

$$\bar{n} = \frac{D+1}{2 \cdot D} \cdot n \cdot c_p \cdot k_{as}(a) \cdot \frac{R_g}{a} \cdot t \quad (11)$$

here,  $t$  is the residence time in the cold region of the flame and  $c_p$  is the fraction of silica particles. Note that this equation coincides with equation (10) if  $D=3$  [26].

The calculated sizes of fractal aggregates are compared with experimentally determined sizes from the  $p_v=0.028 \text{ g/cm}^2\cdot\text{s}$  stoichiometric laminar premixed  $\text{CH}_4/\text{L2}/\text{air}$  flame which was previously described in paragraph 3.2.3. The siloxane concentration for this flame was  $19 \text{ g/m}^3$  L2 in methane. In Figure 17 it can be seen that this flame is in the fractal aggregate growth region at all examined distances ( $\geq 6 \text{ mm}$ ) above the burner surface. The calculations were performed with an experimentally determined fractal dimension of  $D=1.6$  and an experimentally determined initial cluster radius of  $a=3 \text{ nm}$ . The temperature profile and velocity profile to determine the residence time in the flame were calculated using PREMIX. Figure 27 shows the comparison between the model and experimental values.

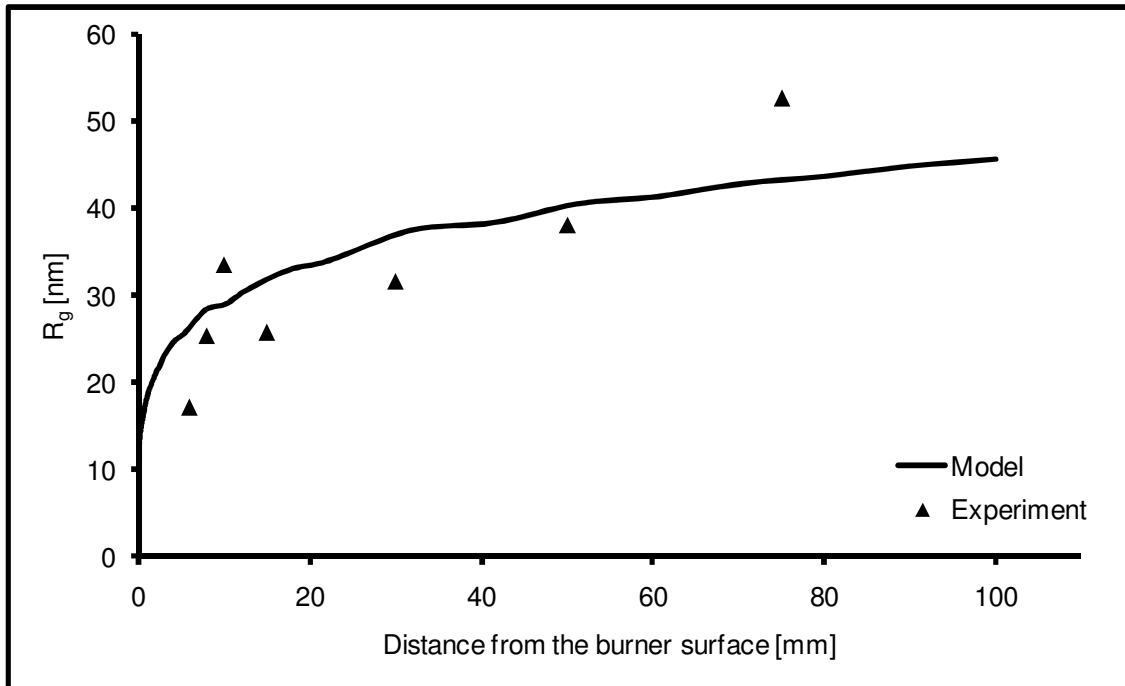


Figure 27: Model to experiment comparison of fractal aggregate sizes in a  $p_v=0.028 \text{ g/cm}^2\cdot\text{s}$  stoichiometric laminar premixed  $\text{CH}_4/\text{L2}/\text{air}$  flame.

In Figure 27 it can be seen that there is a good agreement between the model and the experimentally obtained sizes of fractal aggregates in the  $\rho v = 0.028 \text{ g/cm}^2\cdot\text{s}$  stoichiometric laminar premixed  $\text{CH}_4/\text{L2}/\text{air}$  flame.

No particles could be distinguished on TEM images from samples taken in flames with initial siloxane concentrations below  $2 \text{ g/m}^3$  in methane. Therefore as discussed before, in flames with siloxane concentrations similar to the concentrations found in biogases ( $5 - 400 \text{ mg/m}^3$  see chapter 2) no TEM imaging analysis can be performed. To determine the silica particle sizes in biogas/air flames the silica particle formation models are used. The data obtained in this manner will serve as input for deposition models (described in chapter 5). Furthermore, the developed insights and observed trends in silica particle formation when varying temperature, concentration and residence time will help to understand the obtained results from experiments with domestic appliances (described in chapter 4).

### 3.3 Summary and conclusions: particle formation in flames

In the silica yield experiment we found that all silicon converts to silica upon stoichiometric combustion. This result was expected based on thermodynamic equilibrium calculations. A large quantity of silica was found on the burner surface indicating that silica particles form relatively fast, which is confirmed by TEM analysis of samples taken at a height of 4 mm in a  $\rho v = 0.028 \text{ g/cm}^2\cdot\text{s}$  stoichiometric laminar premixed  $\text{CH}_4/\text{L2}/\text{air}$  flame on which silica particles were observed.

The siloxane concentration and temperature have a large influence on the morphology and size of silica particles in flames. At higher siloxane concentrations, silica particles favor the fractal aggregate structure and at lower concentrations, they favor the cluster structure. The silica particle size also increases with siloxane concentration. At higher temperatures, the sintering process occurs more rapidly resulting in a favor towards cluster structures. The average size of particles also increased at a higher temperature, which is attributed to a decreased viscosity and higher energy collisions between particles leading to a higher probability that particles stick together after collisions.

As a function of distance from the burner surface, silica particles increase in size. Clusters are formed near the burner surface and further downstream they combine in fractal aggregates. Both individual clusters and clusters inside fractals grow due to sintering and Ostwald ripening. This growth occurs rapidly at first and more slowly further downstream. The decrease in growth can be attributed to the decrease in the Ostwald ripening rate since less  $\text{SiO}_2 \text{ (g)}$  is present downstream. In addition, since silica particles grow and the temperature is decreasing downstream the sintering time increases, resulting in a reduced cluster growth.

## 4. Silica deposition in domestic appliances

---

In this chapter, experiments are described for the study of silica deposition in domestic appliances. The first experiments have been performed using a boiler with a lamella heat exchanger. Continued experiments were performed with a geyser to study CO formation due to clogging of silica.

Based on the gathered knowledge from the previous chapter, that the silica particle formation is dependent on concentration, residence time in the flame and temperature, estimations are made of the morphology and size of particles at siloxane concentrations found in biogases. These estimations will help clarify observations made in domestic appliances, which are operating on siloxane containing gases.

### 4.1 Experimental setups to study silica deposition in domestic appliances

#### 4.1.1 Intergas domestic boiler

The boiler used in the experimental work is an Intergas Kombi Kompakt HR 28/24 boiler which is shown in Figure 28. In this figure, the opened boiler is shown on the left and a detailed view of the lamella heat exchanger is shown on the right. Due to its narrow channels, the lamella heat exchanger type is considered the worst case in terms of susceptibility to clogging by silica. It should be noted that this boiler is widely used in the Netherlands.

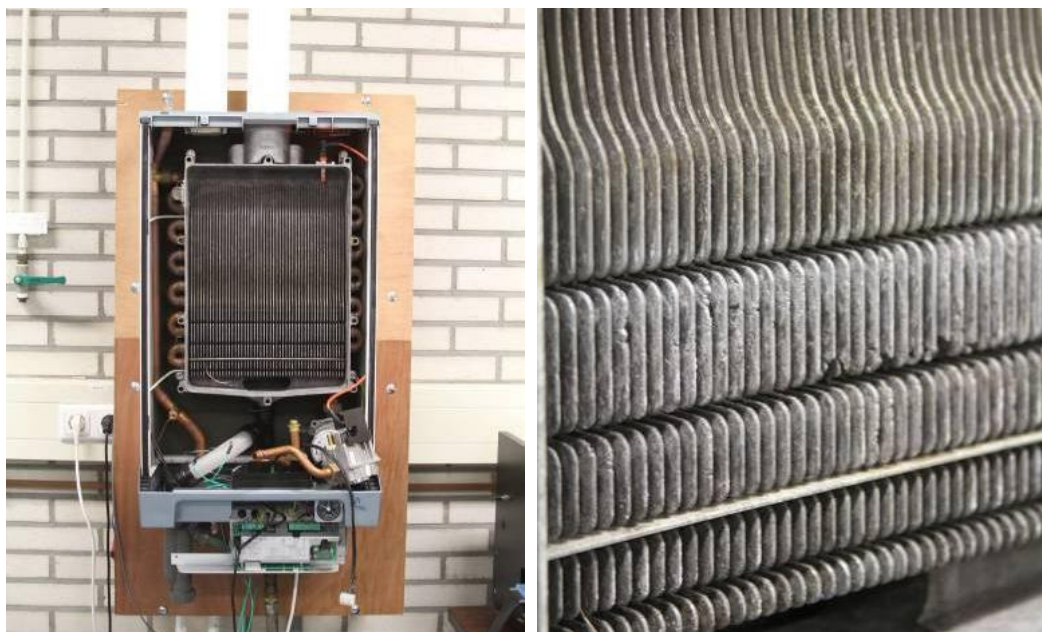


**Figure 28: The Intergas Kombi Kompakt HR 28/24 boiler opened on the left and a detailed view of the heat exchanger on the right.**

The Intergas boiler is a tankless, modulating and condensing boiler for both central heating and domestic hot water. The condense water is removed by means of a drain at the

base of the heat exchanger. The boiler is modular between 30% (stabilized flame) and 100% (free flame) of full load (2.5 m<sup>3</sup>/h maximum gas flow). The load of the appliance, which also influences the temperature of the flame, can be fixed during experiments. The equivalence ratio of the unburned natural gas/air mixture is typically around  $\phi=0.8$ .

The temperature profile in the heat exchanger of the Intergas boiler is measured using thermocouples (type K) at various positions in the heat exchanger. Thermocouples are also used to determine the temperature of the exhaust gases, the cold water supply and the hot water leaving the appliance. Based on the measured temperature difference between the hot and cold water the performance of the boiler can be determined.

The Intergas boiler has a combined ignition and ionization probe positioned close to the burner surface. This probe both ignites the natural gas/air mixture during startup and ensures the flame is still burning by measuring the ionization current through the flame. The working principle of the ionization probe as flame detector is based on the fact that ions in the flame conduct a small current from the ionization probe (6-7 microampere), when the ionization current has fallen below a limit value (1  $\mu$ A) the boiler is locked out. During experiments the ionization current is logged.

#### **4.1.2 Gas handling system for studying silica deposition in the Intergas boiler**

A schematic representation of the gas handling system for the domestic boiler setup is shown in Figure 29. The gas handling system shown in Figure 31 resembles the system shown in Figure 9 with the exception that the static mixer and the lab burner are replaced by the domestic boiler setup. Since the distance between the mixing facility and the boiler is >1 m it is expected that the gases with siloxanes form a homogeneous mixture. The gas handling system is used to introduce a fixed concentration of siloxanes in the natural gas supplied from the local grid. A fan in the boiler extracts air from the surroundings which is premixed with the natural gas (with or without siloxanes) near the burner surface. Bronkhorst EL-FLOW mass flow meters are used to determine the individual natural gas flows to the appliance.



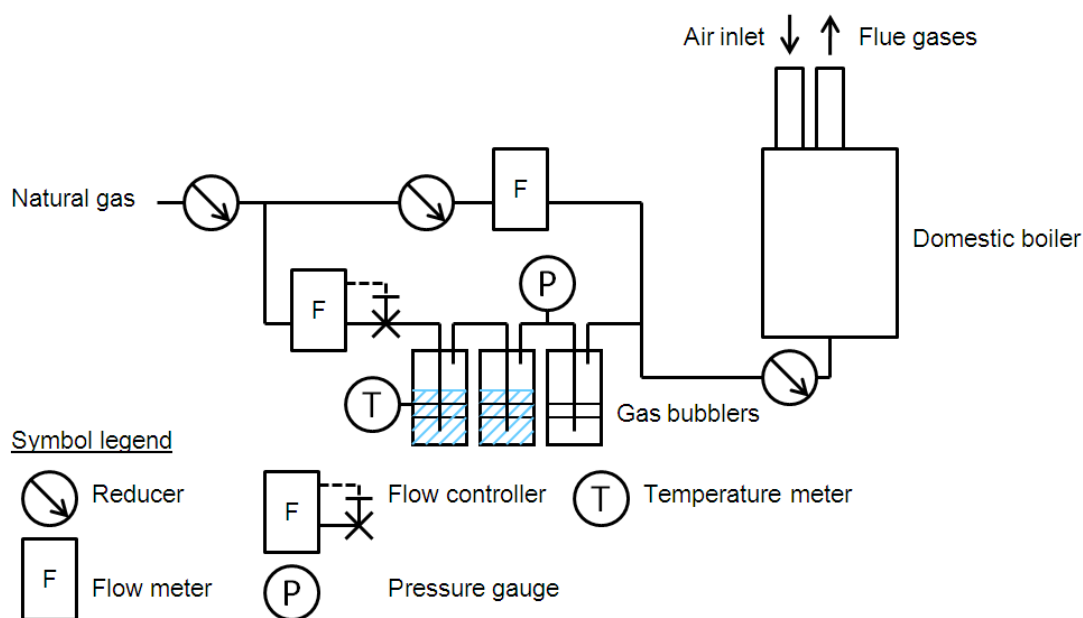


**Figure 29: Gas handling system for the domestic boiler system.**

#### 4.1.3 Vaillant domestic geyser

Most modern boiler appliances including the Intergas Kombi Kompakt boiler contain a zero pressure regulator, which keeps the air/gas ratio constant even if the total flow rate changes. This means that a modern boiler with a zero pressure regulator is not susceptible to reduced aeration due to clogging by silica. Older domestic gas geysers do not have a zero pressure regulator, instead they have partially aerated burners (partially premixed). In a partially aerated burner (such as a Bunsen burner), a portion of the stoichiometric air (also called primary air) is mixed with the fuel gas prior to combustion. The rest of the air (also called secondary air) enters the flame during combustion to complete the combustion process. Clogging of the heat exchanger by silica may increase the flow resistance and reduce the flow of secondary air to the burner. As a result, the mixture becomes fuel richer possibly causing an increased CO emission. To study CO emissions an experimental setup including a domestic gas geyser is used. The domestic geyser used in the experimental work is a Vaillant (MAG 325/7.3 TZWA 25) geyser. The temperature and the concentration of several compounds including CO and oxygen (with which the equivalence ratio can be determined) in the flue gases are monitored during experiments using a flue gas analyzer. In addition, the CO concentrations in the surroundings at several different points are measured continuously for safety reasons. A photograph of the geyser, a CO detector and the flue gas analyzer is shown in Figure 30.



## 4.2 Experimental results and discussion

### 4.2.1 Clogging of the lamella heat exchanger by silica deposition

To determine the impact of silica deposition on the general performance of the Intergas boiler, experiments were performed at different siloxane concentrations in natural gas. The siloxane concentrations used in the experiments were 0.088 g/m<sup>3</sup><sub>n</sub> (5.3 ppm) D5 and 0.163 (22.4 ppm), 0.764 (105.4 ppm) and 3.056 g/m<sup>3</sup><sub>n</sub> (421.8 ppm) L2. Each experiment was continued until 50 grams of silica was produced (according to calculations when assuming 100% conversion to silica). Based on a mass balance of silica over the appliance we found that at least 90% of silica deposits on the heat exchanger for each of the experiments (for details see Appendix IV). The load of the Intergas boiler was fixed, resulting in a steady state natural gas flow of approximately 30 dm<sup>3</sup><sub>n</sub>/min at the start of the experiments. During normal operation of the appliance, without siloxane admixture, the natural gas flow would remain constant in time. Figure 32 shows a graph with the results of the 0.764 g/m<sup>3</sup><sub>n</sub> L2 experiment, where the natural gas flow is plotted as function of the amount of silica produced. With increasing silica production and deposition in the heat exchanger the flow resistance increased resulting in decreased natural gas flow to the boiler. The duration of the 0.764 g/m<sup>3</sup><sub>n</sub> L2 experiment was approximately 58 h, after which a flow reduction of 8.1 dm<sup>3</sup><sub>n</sub>/min (or 26.6%) was observed. The results of the experiments using different concentrations are shown in Table 2.

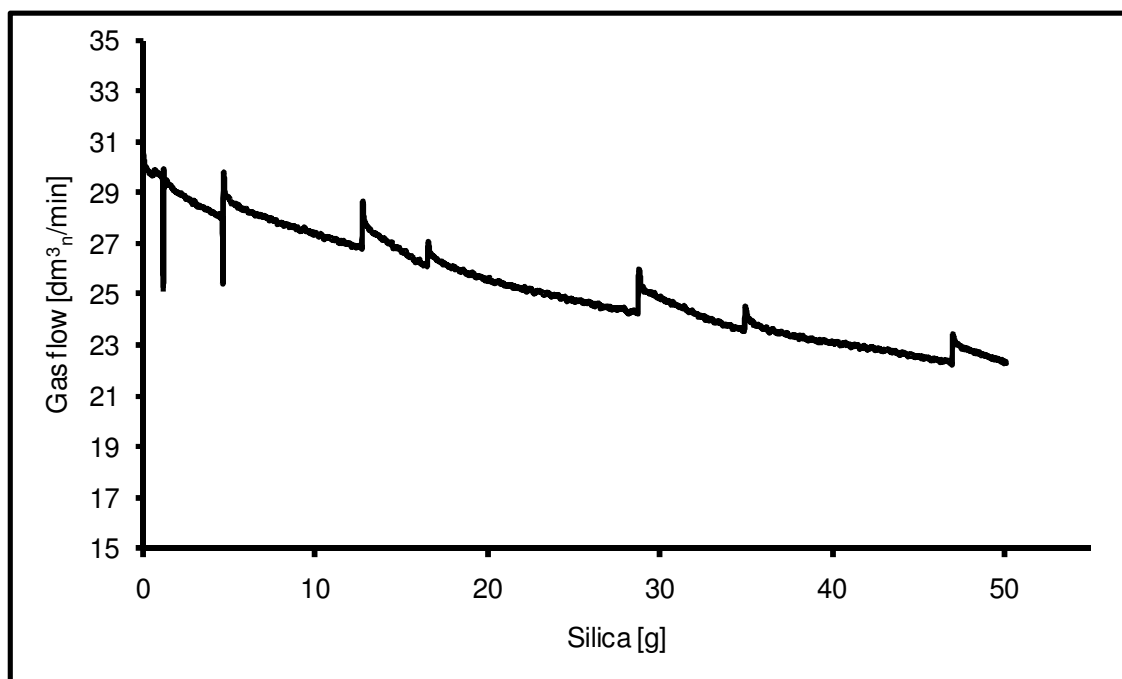


Figure 32: The flow of natural gas with a siloxane concentration of 0.764 g/m<sup>3</sup><sub>n</sub> L2 to the Intergas boiler as a function of the amount of silica produced.

**Table 2: Results of experiments with different siloxane (L2 and D5) concentrations in natural gas in the Intergas boiler. The total amount of silica produced is 50 gram.**

Siloxane [-]	Concentration [g/m <sup>3</sup> <sub>n</sub> ]	Time [h]	Flow start [dm <sup>3</sup> <sub>n</sub> /min]	Flow end [dm <sup>3</sup> <sub>n</sub> /min]	Flow reduction [%]
D5	0.088	440	29.1	23.1	20.6
L2	0.163	269	30.5	23.1	24.3
L2	0.764	58	30.4	22.3	26.6
L2	3.056	14.5	31.2	20.8	33.3

From Table 2 it can be seen that at higher concentrations of siloxanes in natural gas the flow reduction increased even though the same amount of silica was produced (50 g). The density of the silica layer that deposited on the heat exchanger may explain the difference in flow reduction between these experiments. If a fixed mass of silica deposits on an area in the heat exchanger the density will determine the layer thickness of the silica. A thicker layer increases the flow resistance more compared to a thinner layer. After experiments at high concentrations the silica layer appeared to have a low density (structure of loosely stacked powder or snow) and for low concentrations this density appeared high (structure of a paint layer). This is illustrated in Figure 33, where photographs taken of the heat exchanger after the 0.088 g/m<sup>3</sup><sub>n</sub> D5, 0.163 g/m<sup>3</sup><sub>n</sub> L2 and 0.764 g/m<sup>3</sup><sub>n</sub> L2 concentration experiments are shown from top to bottom respectively.



**Figure 33: Photographs taken of the Intergas lamella heat exchanger after experiments with different concentrations. From top to bottom the siloxane concentrations were  $0.088 \text{ g/m}^3_{\text{n D5}}$ ,  $0.163 \text{ g/m}^3_{\text{n L2}}$  and  $0.764 \text{ g/m}^3_{\text{n L2}}$ . For each experiment ~50 grams of silica was produced.**

To investigate whether the density of silica is decreasing with the siloxane concentration, the density of silica in the heat exchanger is determined for the  $0.163 \text{ g/m}^3_{\text{n}}$  and  $0.764 \text{ g/m}^3_{\text{n}}$  L2 concentration experiments at the Zernike Institute of Advanced Materials (University of Groningen). This is done by putting alumina cubes between the lamella of the heat exchanger during the experiments, which were removed carefully afterwards. These cubes are also shown in the lower two photographs of Figure 33: in total 15 cubes were placed at different position in the heat exchanger. The silica layer thickness was determined using spectroscopy techniques. In addition, the (dry) mass of silica on the cubes was accurately determined with a mass balance. Based on the area of the sides of the cubes, the silica

layer thickness and the mass of silica, the density can be calculated. The average density of silica in the  $0.163 \text{ g/m}^3_{\text{n}}$  L2 experiment was determined to be  $1.5 \text{ g/cm}^3$ , while the average density of silica in the  $0.764 \text{ g/m}^3_{\text{n}}$  L2 experiment was determined to be  $0.5 \text{ g/cm}^3$ . This large difference (factor 3) explains the difference in flow reduction observed in Table 2. At lower (or higher) initial siloxane concentrations the difference in density of the deposited silica layer may be even larger.

A possible explanation for the difference in density of the deposited silica may be the morphology of silica particles produced in the flame of the Intergas boiler. At high concentrations the silica particles may have mainly consisted of fractal aggregates whilst at low concentrations they mainly consisted of clusters (see chapter 3). Fractal aggregates and clusters would stack in a different manner during deposition on the heat exchanger. As illustrated in Figure 34 fractal aggregates stack more loosely (low density silica layer) and clusters stack more densely (high density silica layer). This would explain the differences in flow reduction and the observed structural differences of the silica layer between experiments at different concentrations. Note that the morphology of actual particles for the examined concentrations were not determined because the concentration was too low to be able to distinguish particles on the TEM grids (see also chapter 3).

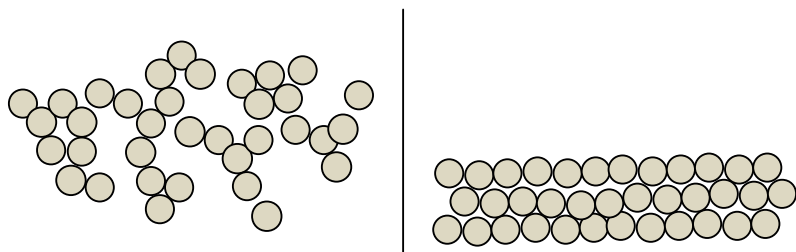


**Figure 34: Two-dimensional schematic overview of a loose layer of silica on the left and a dense layer of silica on the right. The loose layer consists of fractal aggregates and the dense layer consists of individual clusters. Note the difference in thickness between the layers.**

A second explanation for the difference in density of the deposited silica layer may be the size of the silica particles in the flue gases. At higher concentrations the particles would be bigger than at lower concentrations (see chapter 3). Small particles if sufficiently hot will easily sinter onto the relatively cold walls of the heat exchanger. Bigger particles sinter more slowly and may be frozen solid before the sintering process is complete. The bigger particles would therefore stack in a more randomly, creating a less dense silica layer. This behavior may be valid for both individual clusters and fractal aggregates.

It should be noted that the concentration of  $0.088 \text{ g/m}^3_{\text{n}}$  (5.3 ppm, see Table 2) D5 is close to the current specification of siloxanes for biogases in the Netherlands (which is 5 ppm). After 440 hours (much less than a year of normal operation of  $\sim 700 \text{ h}$ ), a natural gas flow reduction of 20.6 % was observed. Such a flow reduction results in a significantly reduced thermal output, which may render the appliance inept for domestic heating.

The reduction in the natural gas flow was observed to be similar to the reduction in thermal output of the Intergas boiler for each siloxane concentration. In other words, the

efficiency of the boiler remained the same. An efficiency decrease might have been expected since the silica layer in the heat exchanger contributes to the thermal resistance of the heat exchanger walls. On the other hand, the residence time of the hot gases in the heat exchanger increases due to the flow resistance caused by the silica layer. An increased residence time allows for a longer period of time in which heat can be exchanged. Apparently, the effect of the increased residence time on the efficiency of the boiler and the effect of the insulating silica layer cancel each other out.

For the Intergas boiler most of the produced silica particles deposit on the heat exchanger and almost no silica particles are expelled into the surroundings (discussed in Appendix IV). This is not the case for some other domestic appliances. With gas cookers, for example all combustion products are expelled into the interior, including any formed silica particles. Since these particles are very small ( $<100$  nm, see also chapter 3) they may be harmful for end users. Further research is necessary in order to determine the contribution of these particles on an environmental or health burden at different concentrations. However, this research lies outside the scope of this thesis.

#### 4.2.2 Effect of siloxanes on the ionization probe

During the different experiments with siloxanes in natural gas, the ionization current of the ionization probe in the Intergas boiler was measured. When the Intergas boiler was operating on siloxane containing natural gas the ionization current decreased over time. Figure 35 shows a graph with the ionization current as a function of time for the  $3.056 \text{ g/m}^3_{\text{n}}$  L2 experiment.

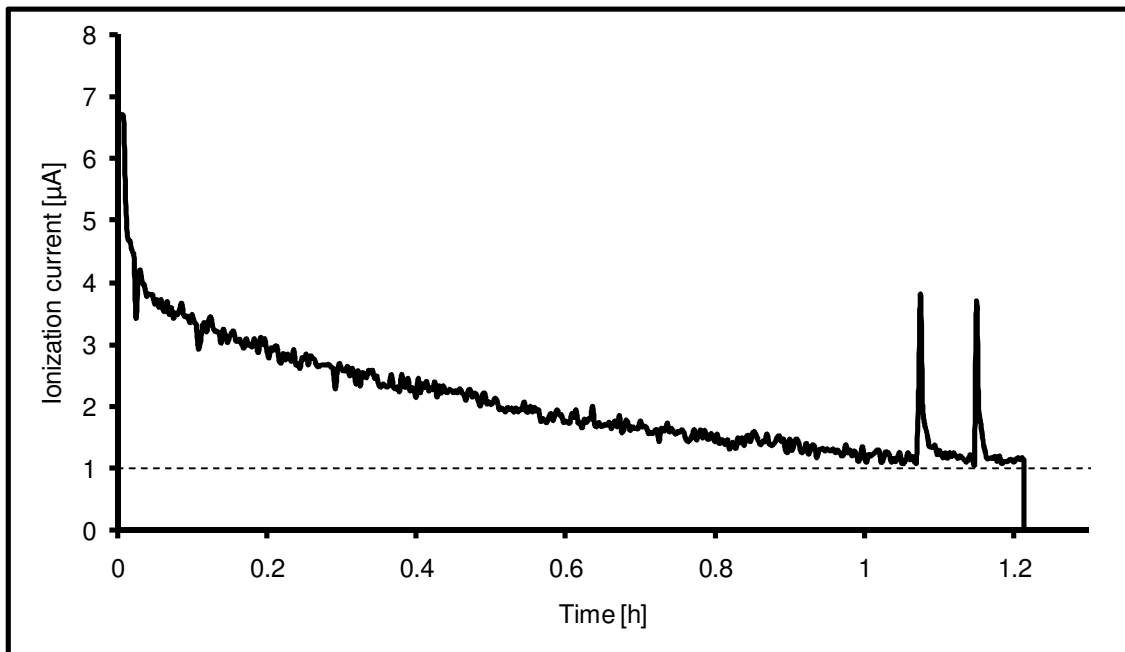
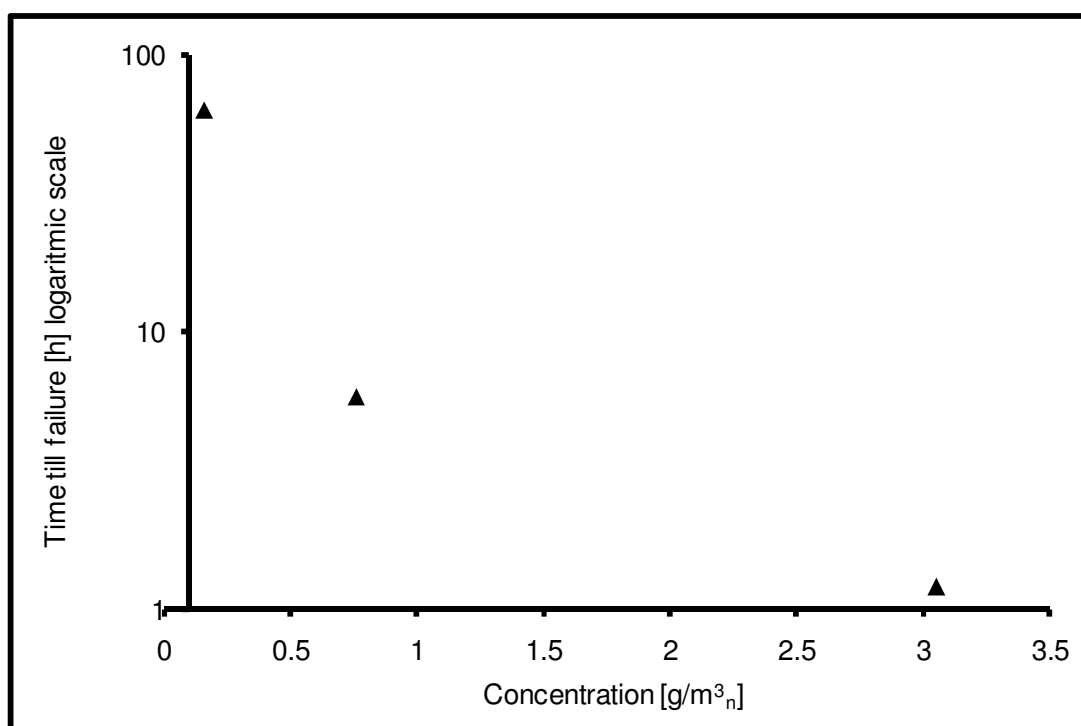


Figure 35: Ionization current as a function of time for the experiment with a concentration of  $3.056 \text{ g/m}^3_{\text{n}}$  L2 in natural gas. The dotted line shows the critical value at which the appliance fails.

In Figure 35 it can be seen that the ionization current reduces over time, until the critical value ( $1\ \mu\text{A}$ ) is reached, below this value the appliance shuts itself down by closing the natural gas supply. Upon failure of the ionization probe, it was removed and the tip was observed to be covered with a layer of silica. Figure 36 shows a photograph made of an ionization probe covered with silica. Each time after a failure of the ionization probes, a new probe was installed or the old probe was cleaned using a steel brush. After cleaning the measured ionization currents were similar to the values before siloxanes were added. This suggests that the silica layer on the ionization probe has an insulating effect, preventing the correct measurement of the ionization current. The time till failure for the experiments performed with siloxane concentrations of  $0.163$  (22.4 ppm),  $0.764$  (105.4 ppm) and  $3.056\ \text{g/m}^3_n$  (421.8 ppm) L2 is shown in Figure 37 and Table 3.



**Figure 36:** Ionization probe from the Intergas boiler covered with silica.



**Figure 37:** Time till failure of the ionization probe as a function of initial siloxane concentration.



**Table 3: Time till failure of the ionization probe.**

Siloxane [-]	Concentration [g/m <sup>3</sup> <sub>n</sub> ]	Time till failure [h]
L2	0.163	63
L2	0.764	5.8
L2	3.056	1.2

Note in Figure 37 and Table 3 that the time till failure decreases as the concentration increases but not linearly, there may be two explanations for this non-linear behavior. The first explanation is that the thickness of the silica layer on the ionization probe increases with concentration because the density of the layer is decreasing even though the same amount of silica is on the probe. The second explanation may be that siloxanes or combustion products of siloxanes influence the ionization current itself. This influence would increase with concentration. In Figure 38 a graph is shown with the ionization current as a function of time. The siloxane containing methane flow was switched off for a short period of time twice, which resulted in the two peaks shown in Figure 38. Since the ionization current does not remain the same but switches back to much higher values the siloxanes themselves must have a direct influence on the ionization current. This effect was observed to increase with the siloxane concentration. Since not much is known about the chemical mechanisms for the combustion of siloxanes further research is necessary to study the influence of siloxanes on ions in flames. This study lies outside the scope of this thesis however.

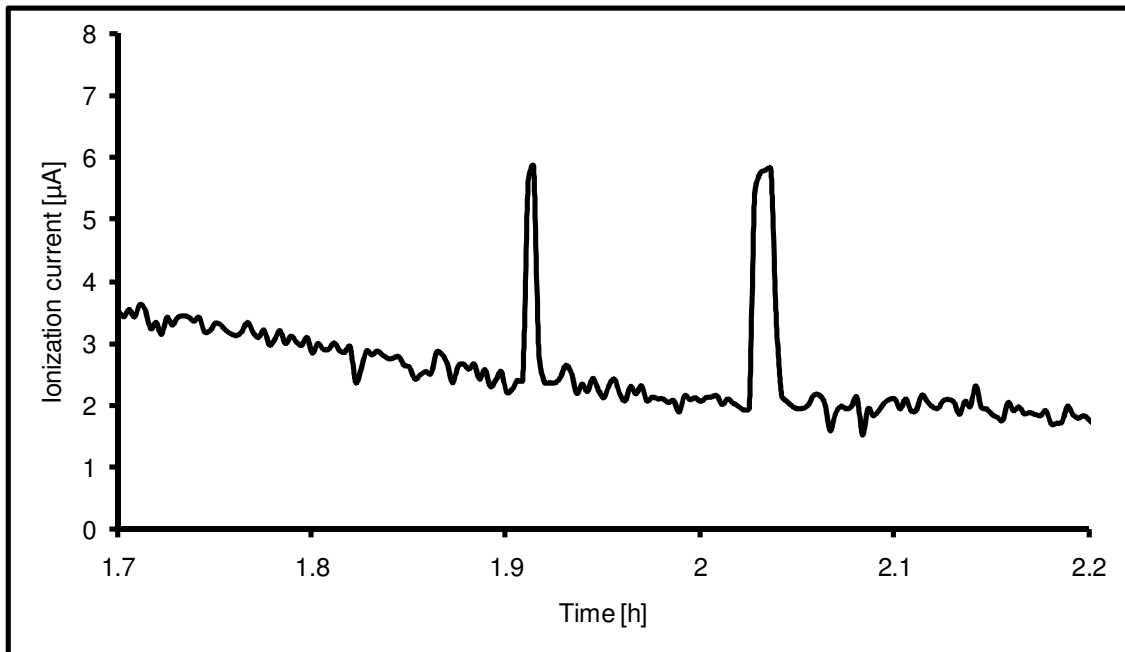


**Figure 38: Ionization current as a function of time for the experiment with a concentration of 3.056 g/m<sup>3</sup><sub>n</sub> L2 in natural gas. The two peaks correspond to switching siloxanes off and on again twice.**

#### 4.2.3 Influence of silica clogging on CO emissions in a domestic geyser

To determine the influence of clogging by silica particles on the CO emissions of a domestic geyser, experiments were performed with a siloxane concentration of  $1.507 \text{ g/m}^3_{\text{n}}$  L2 in the natural gas flow to the Vaillant geyser. Figure 39 shows the natural gas flow to the geyser as a function of time. The natural gas flow is decreasing due to clogging of the heat exchanger by silica particles, which caused an increased flow resistance through the heat exchanger of the geyser.

Due to the clogging of the heat exchanger the aeration of the geyser was reduced. This resulted in an increase of the equivalence ratio causing increased CO emissions of the appliance. The CO emission measured with the flue gas analyzer above the heat exchanger of the geyser is shown in Figure 40 as a function of time.

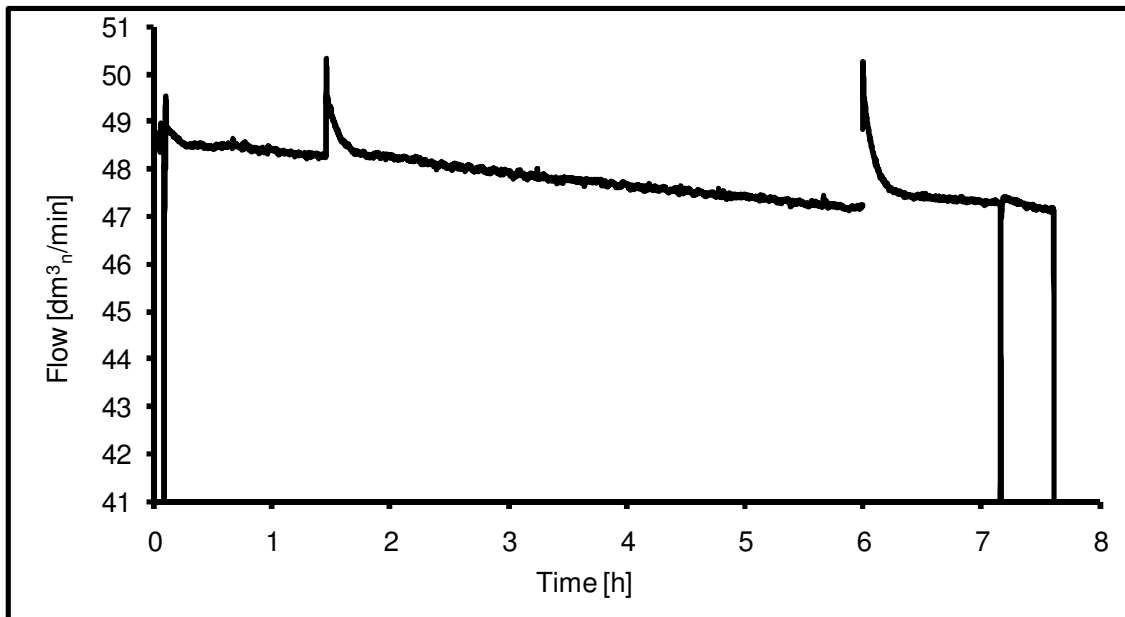
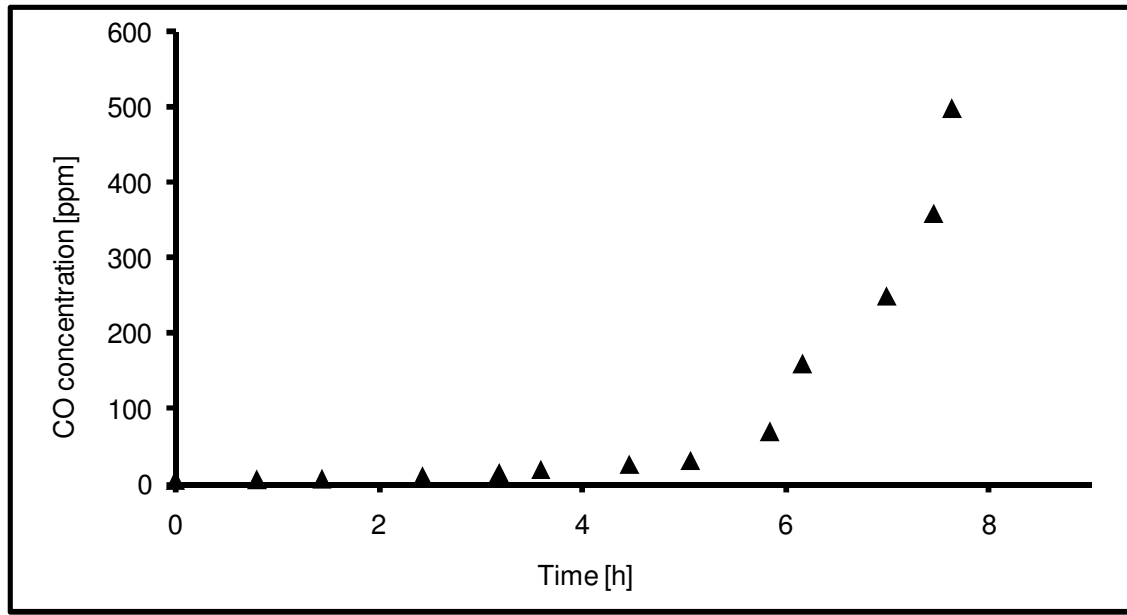


Figure 39: Natural gas flow to the Vaillant geyser as a function of time. The siloxane concentration is  $1.507 \text{ g/m}^3_{\text{n}}$  L2 in natural gas.



**Figure 40: Natural gas flow to the Vaillant geyser as a function of time. The siloxane concentration is  $1.507 \text{ g/m}^3_{\text{n L2}}$  in natural gas.**

In Figure 40 it can be seen that the CO emission rises exponentially up to 500 ppm after 7.5 hours. At this point the CO concentration in the surroundings was 25 ppm (above the permissible exposure limit) and for safety reasons the experiment was aborted. It should be noted that the equivalence ratio increased linearly during the experiment.

#### **4.3 Summary and conclusions: silica deposition in domestic appliances**

Experiments with different siloxane concentrations in the Intergas boiler have yielded that increasing deposition of silica in the heat exchanger results in a decrease of the natural gas flow to the appliance. This decrease in flow is attributed to an increased flow resistance caused by the clogging effect of silica particles in the heat exchanger. The thermal output of the appliance was observed to decrease proportionally with the flow. This indicates that the efficiency of the appliance is constant despite the added thermal resistance of a silica layer in the heat exchanger. Due to the clogging effect of silica the residence time of combustion products in the appliance increased, cancelling out the effect of an increased thermal resistance in terms of efficiency.

The flow resistance caused by silica was observed to be non-linear with siloxane concentration: increasing the siloxane concentration increased the clogging in the heat exchanger even though the same amount of silica was produced. A possible explanation of this difference is given by the observed change in the density of the silica layer: for  $0.163 \text{ g/m}^3_{\text{n L2}}$  an average density of  $1.5 \text{ g/cm}^3$  and for  $0.764 \text{ g/m}^3_{\text{n L2}}$  an average density of  $0.5 \text{ g/cm}^3$  was found. This density difference of a factor 3 influences the flow resistance of the flue gases in the appliance via the layer thickness. A difference in the morphology (clusters

opposed to fractal aggregates) or the size of the silica particles may have caused the difference in density.

Although nearly all the particles deposit inside the heat exchanger of the Intergas boiler, it should be noted that this is not the case for some other domestic appliances. Since silica particles can be assumed to be sufficiently small ( $<100$  nm) they may contribute to an environmental or health burden. Further research is necessary to determine the impact of these particles on the environment and public health.

The measured ionization current decreased as more silica was produced during experiments. When the critical value of ionization current was reached the Intergas boiler automatically turned off. The time till failure of the ionization probe did not linearly scale with concentration. This may be caused by the density of the silica layer on the tip of the ionization probe, which decreases with siloxane concentration. This silica layer is believed to be one of the factors causing the reduction of ionization current over time. The other factor can be the effect of siloxanes or their combustion products on the flame ions, these appear to have a decreasing effect on the ionization current itself.

In an experiment with a domestic geyser appliance operating on siloxane containing natural gas the CO emissions were observed to increase exponentially up to 500 ppm inside the boiler and 25 ppm in the surroundings (above the permissible exposure limit). This increase in CO emission is attributed to an increased flow resistance caused by silica particles in the heat exchanger. Further research is necessary in order to determine how the CO emissions of the geyser scale with siloxane concentration.

## 5. Silica particle deposition model

In this chapter, a model to predict the deposition of silica particles in a heat exchanger is described. The model is applied to the lamella heat exchanger (worst case in terms of susceptibility to clogging) of the Intergas boiler for comparison with the experimental results of chapter 4, this way the accuracy of the model can be examined. The maximum allowable silicon content in biogases can be determined for this application using the model, by extrapolating the short-term practical tests of chapter 4. This will remove the necessity of performing time consuming long-term tests (order of years) with domestic appliances to determine specifications for siloxanes in biogases. The model can also be modified for application to other types of heat exchangers and appliances.

### 5.1 Temperature profile in the heat exchanger

In this paragraph the temperature profile in the Intergas lamella heat exchanger is modeled. The temperature profile is needed to determine the residence time of the flue gases in the heat exchanger and for thermophoresis (see paragraph 5.2). Figure 41 shows a schematic overview of the lamella heat exchanger in the Intergas boiler, with a side view on the left and a detailed view of the lamella from above on the right.

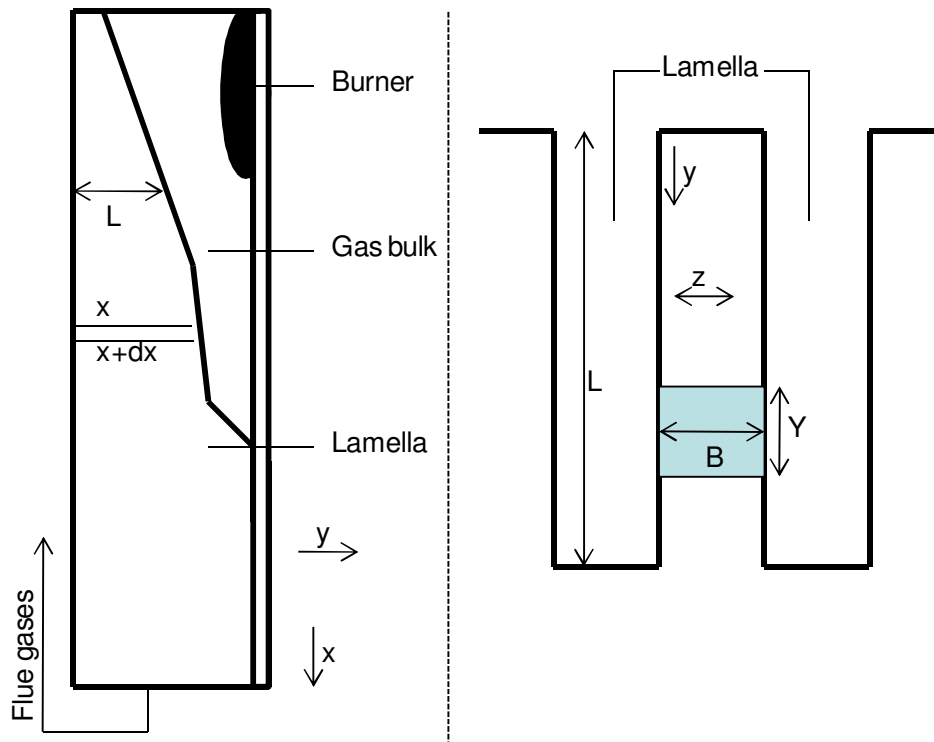


**Figure 41: Schematic overview of the lamella heat exchanger from the side on the left and a detailed overview of the lamella from above on the right. The x, y and z direction are depicted in the pictures.**

In Figure 41 the directions x, y and z are shown, the flue gases flow in the x direction (laminar flow). The blue cube in the right of Figure 41 depicts the volume with the dimensions  $dx \cdot Y \cdot B$  for which the temperature calculations are performed. We assume that most of the heat is exchanged in between the different lamella (50 in total), which is in the z direction. Notice that the length L of the lamella is increasing downstream and that flue gases are supplied to the lamella via the gas bulk, which has an almost constant temperature. Because hot flue gases are supplied as the lamella increase in length, a temperature profile exists not only in the x direction but also in the y direction. Equation (12) is used to determine the temperature profile in the x direction [34].

$$dQ = 2 \cdot U \cdot (T_h - T_c) \cdot dx \cdot Y = -(\phi_m \cdot C_p)_h \cdot dT_h = -(\phi_m \cdot C_p)_c \cdot dT_c \quad (12)$$

here, Q is the heat flow in W,  $\Phi_m$  is the mass flow rate of the flue gases or the water in kg/s,  $C_p$  is the specific heat in  $J \cdot kg^{-1} \cdot K^{-1}$ , U is the overall heat transfer coefficient in  $W \cdot m^{-2} \cdot K^{-1}$ ,  $T_h$  is the average temperature of the flue gases in K and  $T_c$  is the average temperature of the water in K. The subscripts c and h stand for cold and hot referring to the cold water and the hot flue gases of the heat exchanger. In equation (12), the second term describes the conductive heat transfer from the flue gases to the water, the third term describes the convective heat transfer due to the flow of the flue gases and the fourth term describes the convective heat transfer due to the flow of water.

The overall heat transfer coefficient U in equation (12) combines all the thermal resistances through which heat exchange occurs. In the Intergas boiler the heat is exchanged from the flue gases through the alumina heat exchanger to water inside copper pipes (shown in Figure 42).

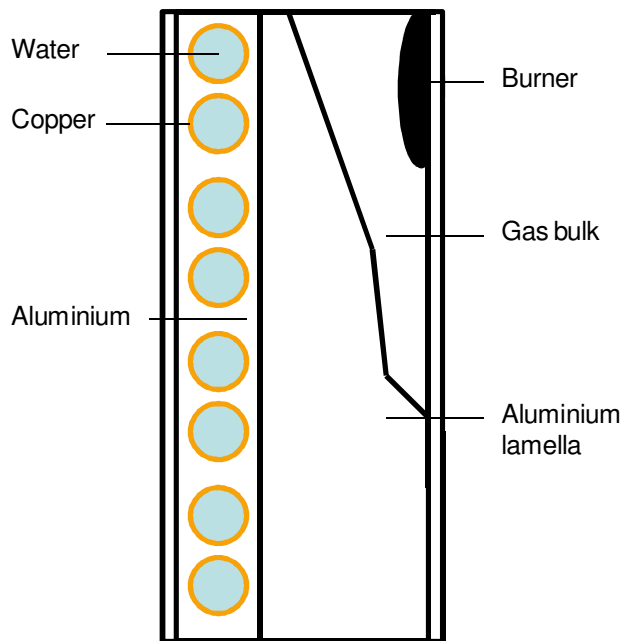


**Figure 42: Schematic overview of the lamella heat exchanger. The position of the copper tubes through which water flows is shown in the figure.**

Equation (13) is used to determine the overall heat transfer coefficient.

$$U = \frac{1}{\frac{1}{h_{flue}} + \frac{d_{al}}{k_{al}} + \frac{d_{cu}}{k_{cu}} + \frac{1}{h_{H_2O}}} \quad (13)$$

where  $h_{flue}$  is the heat transfer coefficient for the flue gases in  $W \cdot m^{-2} \cdot K^{-1}$ ,  $h_{H_2O}$  is the heat transfer coefficient for the water in  $W \cdot m^{-2} \cdot K^{-1}$ ,  $d_{al}$  is the thickness of the alumina layer in m,  $d_{cu}$  is the thickness of the copper layer in m,  $k_{al}$  is the thermal conductivity coefficient for alumina and  $k_{cu}$  is the thermal conductivity coefficient for copper. The thickness of the copper layer is estimated to be 1 mm and the thickness of the alumina layer is estimated to be 10 mm on average (depends on position in the heat exchanger). The heat transfer coefficient for the flue gases is determined using the definition of the Nusselt number (Nu) shown in equation (14) [36].

$$Nu = \frac{D_h \cdot h_{flue}}{k_{flue}} \quad (14)$$

here,  $D_h$  is the hydraulic diameter of the square or rectangular cross section of the lamella in m and  $k_{flue}$  is the thermal conductivity of the flue gases in  $W \cdot m^{-1} \cdot K^{-1}$ . Nusselt numbers for fully developed laminar flow are used from Ref. [34] in which the geometry of the cross section is taken into account. The calculated Reynolds numbers vary between 400 and 900, depending on the position in the heat exchanger, which is well in the laminar flow regime. The heat transfer coefficient for water is determined using the empirical Dittus-Bölder correlation shown in equation (15) [36].

$$Nu = \frac{D_h \cdot h_{H_2O}}{k_{H_2O}} = 0.027 \cdot Re^{0.8} \cdot Pr^{0.33} \quad (Re > 10^4, Pr \geq 0.7) \quad (15)$$

where,  $k_{H_2O}$  is the thermal conductivity coefficient for water in  $W \cdot m^{-1} \cdot K^{-1}$ ,  $Re$  is the dimensionless Reynolds number and  $Pr$  is the dimensionless Prandtl number. The Dittus-Bölder correlation is valid for Reynolds numbers above  $10^4$  and Prandtl numbers above or equal to 0.7. The Reynolds number for the water flowing in the copper tubes is  $\sim 2 \cdot 10^4$  and the Prandtl number is  $\sim 3.5$ , both dimensionless numbers are dependent on temperature. The values for the thermal conductivities ( $k_{flue}$ ,  $k_{al}$ ,  $k_{cu}$  and  $k_{H_2O}$ ) used in the calculations of are shown in appendix VI as a function of temperature. In appendix VI the specific heat of both water and the flue gases are also shown as a function of temperature.

For each cross section of the heat exchanger equation (16) is valid [34], for the counter flow configuration of the Intergas heat exchanger.

$$-(\phi_m \cdot C_p)_h \cdot (T_h - T_{h,in}) = -(\phi_m \cdot C_p)_c \cdot (T_c - T_{c,in}) \quad (16)$$

Since  $k$ ,  $h$  and  $C_p$  are dependent on temperature equation (12) and equation (16) are combined and solved numerically (using Excel) with small steps in the  $x$  direction (365 steps of 1 mm). Depending on the temperature in each section the values for  $k$ ,  $h$  and  $C_p$  are determined (see appendix VI). The boundary conditions are the initial temperatures of the flame (calculated with PREMIX) and the temperature of the water leaving the appliance (measured with a type K thermocouple). The temperature profile in the  $y$  direction is determined by performing the calculations in the  $x$  direction with multiple small steps in the  $y$  direction. The amount of heat exchanged in the  $z$  direction is assumed to be much larger than the heat exchanged in the  $y$  direction, therefore the heat exchange in the  $y$  direction is neglected.

The temperature profiles in the  $y$  direction for different distances from the top of the heat exchanger are compared with experimentally determined temperature profiles in the Intergas boiler. This comparison is discussed in detail in Appendix V and one example is shown in Figure 43 for  $x=200$  mm.

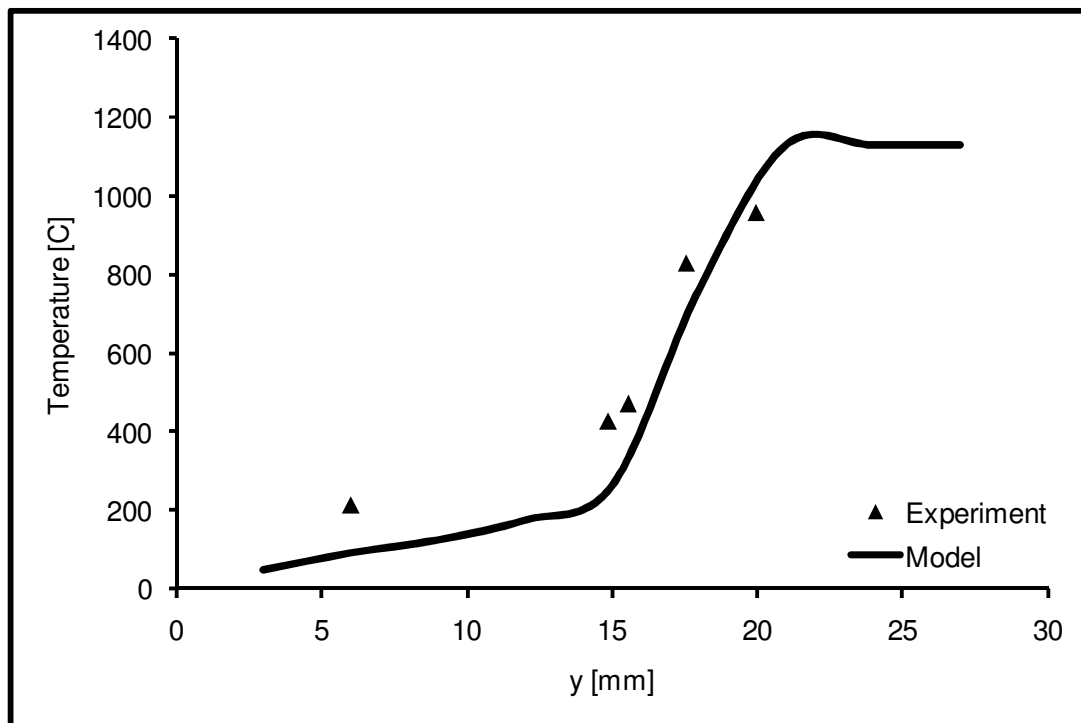


**Figure 43: Model to experiment comparison with the temperature between the lamella of the Intergas boiler in the  $y$  direction for  $x=200$  mm.**

The difference between the modeled temperature profiles and the measured temperature profiles are sufficiently small for our purpose. In Figure 43, it can be seen that the temperature for low values of  $y$  is underestimated in the model and for high values of  $y$  the temperature is overestimated. This difference between model and experiment is attributed to the assumption that no heat exchange occurs in the  $y$  direction. In reality heat exchange



does occur in the y direction and therefore this assumption is a rough approximation. It should be noted that the temperature profile and deposition model have an estimative character.

## 5.2 Thermophoresis and diffusion

Along the heat exchanger the flue gases are cooled by the lamella and the silica particles are transported to the wall via thermophoresis and diffusion. Thermophoresis is the force that drives particles from high to low temperature regions. The drift velocity of particles ( $c_t$  in m/s) due to thermophoresis can be calculated using equation (17), which is valid if the mean free path of the surrounding gas molecules is much larger than the diameter of the particles (this is the case for the conditions in the heat exchanger if particles are  $< \sim 500$  nm) [38].

$$c_t = \frac{-3 \cdot \eta \cdot \nabla T}{4 \cdot \rho (1 + \pi \cdot \alpha / 8) \cdot T} \quad (17)$$

where  $\alpha$  is the dimensionless accommodation coefficient (usually around 0.9 [38]). Note that the thermophoretic drift velocity is independent of particle size in this regime. This indicates that the deposited mass per area in the heat exchanger is independent on particle size if thermophoresis would be the only deposition mechanism.

For diffusion of silica particles to the heat exchanger walls we use Fick's law of diffusion in which the particle flux ( $J$  in  $m^{-2} \cdot s^{-1}$ ) is determined with equation (18).

$$J = -D \cdot \nabla N_p \quad (18)$$

here,  $D$  is the diffusion coefficient in  $m^2/s$  and  $N_p$  is the silica particle concentration in  $m^{-3}$ . The diffusion coefficient is determined with equation (19) [38].

$$D = \frac{C \cdot k_b \cdot T \cdot \rho}{3 \cdot \pi \cdot \eta \cdot d_p} \quad (19)$$

where,  $d_p$  is the particle diameter in m and  $C$  is a correction factor which is 1 if the particle diameter is much larger than the mean free path of molecules and becomes large if the mean free path is much larger than particle diameter. In calculations the values for  $C$  are extracted from Ref. [38].

### 5.3 Deposition model

For the disappearance rate of silica particles we can write equation (20) [37].

$$\frac{dN_p}{dt} = -\nabla(D \cdot \nabla N_p - c_t \cdot N_p) + v \cdot \nabla N_p - R \quad (20)$$

In equation (20) the first term on the right side of the equation is the diffusion term, the second term on the right is the thermophoretic velocity of silica particles, the third term is the convection term and the fourth term describes the disappearance of particles due to growth (chapter 3). In the model we assume that convection only takes place in the direction of the bulk flow (x direction), that thermophoresis only takes place in the z direction (temperature gradient in the z direction >> than in the x and y direction) and we assume steady state (the term  $dN_p/dt = 0$ ). Based on these assumptions, the model calculates the mass of particles which deposit on different areas of the heat exchanger. The results of these model calculations are currently in development at the Zernike Institute of Advanced Materials (University of Groningen). To be able to make a qualitative estimation of the deposition of silica particles a simplified model is presented in this thesis. In the simplified model diffusion and thermophoresis are considered as first order differential equations and both are considered to only occur in the z direction.

To be able to perform a model to experiment comparison the simplified deposition model is applied to an L2 concentration of  $0.163 \text{ g/m}^3_n$  over a period of time in which 50 grams of silica is produced. The calculated layer thicknesses at different values for x are shown in Figure 44. For the calculations a density of  $1.5 \text{ g/cm}^3$  is used which is equal to the experimentally determined density for this siloxane concentration.

From Figure 44 it can be seen that the silica layer thickness is the largest at the top of the lamella. Further to the back wall there is almost no silica deposition according to these calculations. An increased amount of deposition near the top of the lamella was also observed during experiments. This can also be seen on the photographs of Figure 33 (chapter 4).

The calculated layer thickness appears to be more or less constant up to a value of  $x=190 \text{ mm}$ , after that the silica layer increases in thickness. There are several reasons for this behavior. The temperature in the heat exchanger decreases downstream resulting in an increased particle concentration and residence time. In addition, the lamella decrease in thickness in the x direction so there is more volume available for the flue gases downstream, which also increases the residence time. An increased residence time allows for more time in which thermophoresis and diffusion can occur. From equation (20) it can be seen that with an increasing particle concentration the thermophoresis and diffusion terms increase resulting in a thicker silica layer. A thicker silica layer was also observed (at  $x \sim 240 \text{ mm}$ ) during the experiment with an L2 concentration of  $3.056 \text{ g/m}^3_n$ , see also Figure 45.

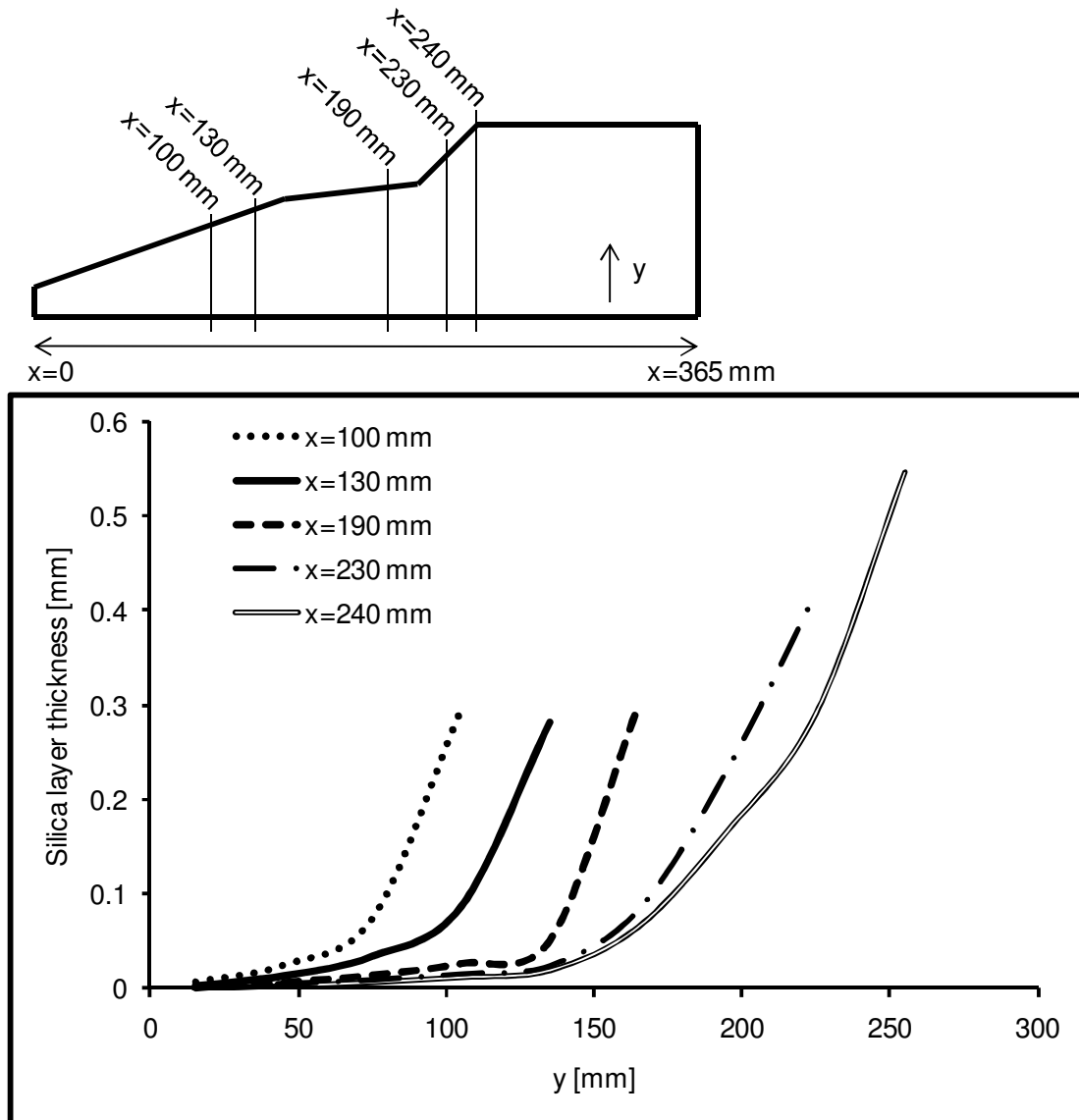


**Figure 44: Calculated layer thicknesses at different values for  $x$ . Note from the schematic overview of the lamella above that the lamella increase in length as a function of  $x$ .**

The silica particles sizes were calculated by making the assumption that up to  $x=30$  mm cluster growth was the main growth process. In this area of the heat exchanger, the cluster growth equations of paragraph 3.2.5.1 were used. For  $x>30$  mm the fractal aggregate equations described in paragraph 3.2.5.2 were used. The determined particle sizes for the  $0.163 \text{ g/m}^3$  L2 concentration experiment were 5 nm for the clusters and up to 30 nm for the fractal aggregates. Since it is unknown where the cluster growth region ends and the fractal aggregate region starts these values can be considered as approximations. In a comparison between thermophoretic and diffusive deposition more than 99% of the silica particles were determined to deposit by thermophoresis. Since thermophoresis is independent of particle size more accurate values for particle sizes are not necessary. These silica particles are sufficiently small however, to contribute to a health or environmental burden.

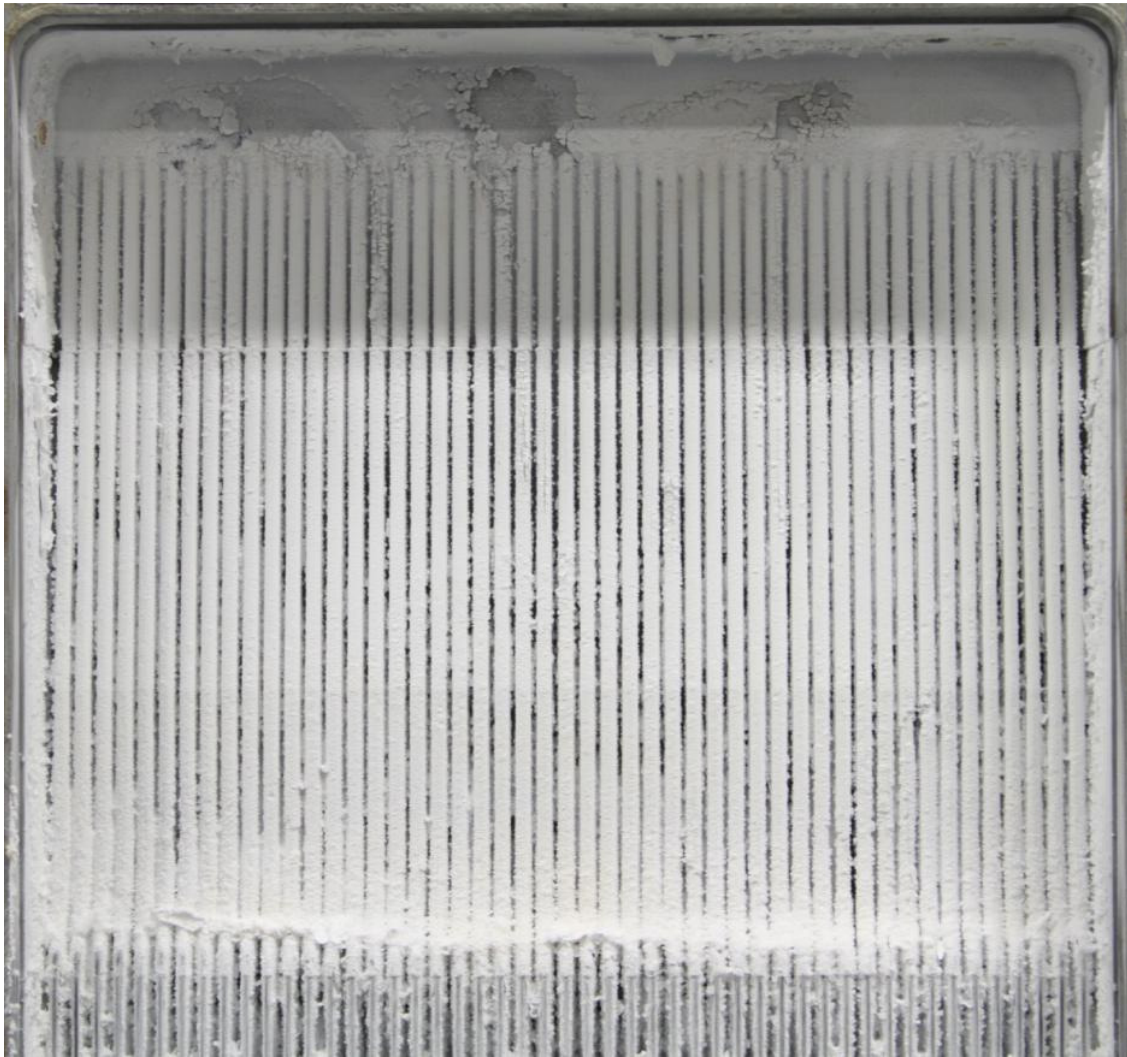


**Figure 45: Photograph taken of the Intergas lamella heat exchanger after experiments with an L2 concentration of  $3.056 \text{ g/m}^3_{\text{n}}$ . Note that at the bottom of the photograph ( $x \sim 240 \text{ mm}$ ) the lamella are almost completely clogged with silica.**

As described before, the density of the silica on the alumina cubes placed in the Intergas heat exchanger were determined for the experiments with L2 concentrations of  $0.163 \text{ g/m}^3_{\text{n}}$  and  $0.764 \text{ g/m}^3_{\text{n}}$ . For the  $0.764 \text{ g/m}^3_{\text{n}}$  L2 concentration, the determined densities were more or less the same for each of the examined cubes ( $\sim 0.5 \text{ g/cm}^3$ ). It should be noted that the silica layer on the cubes were damaged for many of the examined samples. For the  $0.163 \text{ g/m}^3_{\text{n}}$  L2 concentration experiment, all the cubes were intact. The experimentally determined densities of the silica layer on each of the cubes shown in Figure 46.

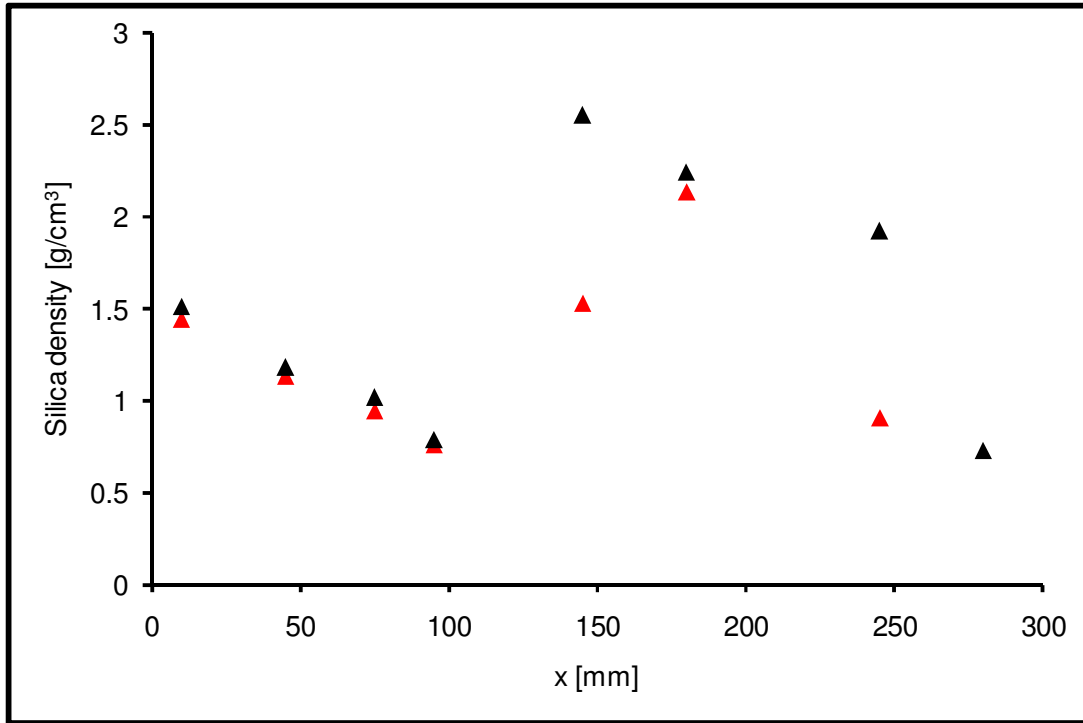


**Figure 46: Experimentally determined densities of silica on the alumina cubes placed in the Intergas heat exchanger for the  $0.163 \text{ g/m}^3$  L2 concentration experiment. The markers of the duplo measurements are colored red.**

In Figure 46 it can be seen that up to  $x=100 \text{ mm}$  the density of silica in the heat exchanger appears to decrease linearly. This may be because the silica particles in the heat exchanger are growing or because their morphology is changing downstream, which would cause the density to decrease (chapter 3). Note that the result of each duplo (red markers) measurement is similar up to  $x=100 \text{ mm}$ . When  $x>100 \text{ mm}$  the results seem less accurate. Some densities are above the bulk density of silica ( $\sim 2.3 \text{ g/cm}^3$  [16]), which is possibly due to contaminants like aluminum or aluminum oxide in the silica layer. If we remove the less accurate data points ( $x=145 \text{ mm}$ ,  $x=180 \text{ mm}$  and  $x=245 \text{ mm}$ ) and use the density profile as input for the deposition model we obtain the graph in Figure 47, assuming that the density is constant around  $0.75 \text{ g/cm}^3$  for  $x>100 \text{ mm}$ . The calculated layer thicknesses in Figure 47 are the values found at the top of the lamella ( $y=L$ ), which is at the same position where the aluminum cubes were placed. In Figure 47, the experimentally determined layer thicknesses are compared to the calculated layer thicknesses.

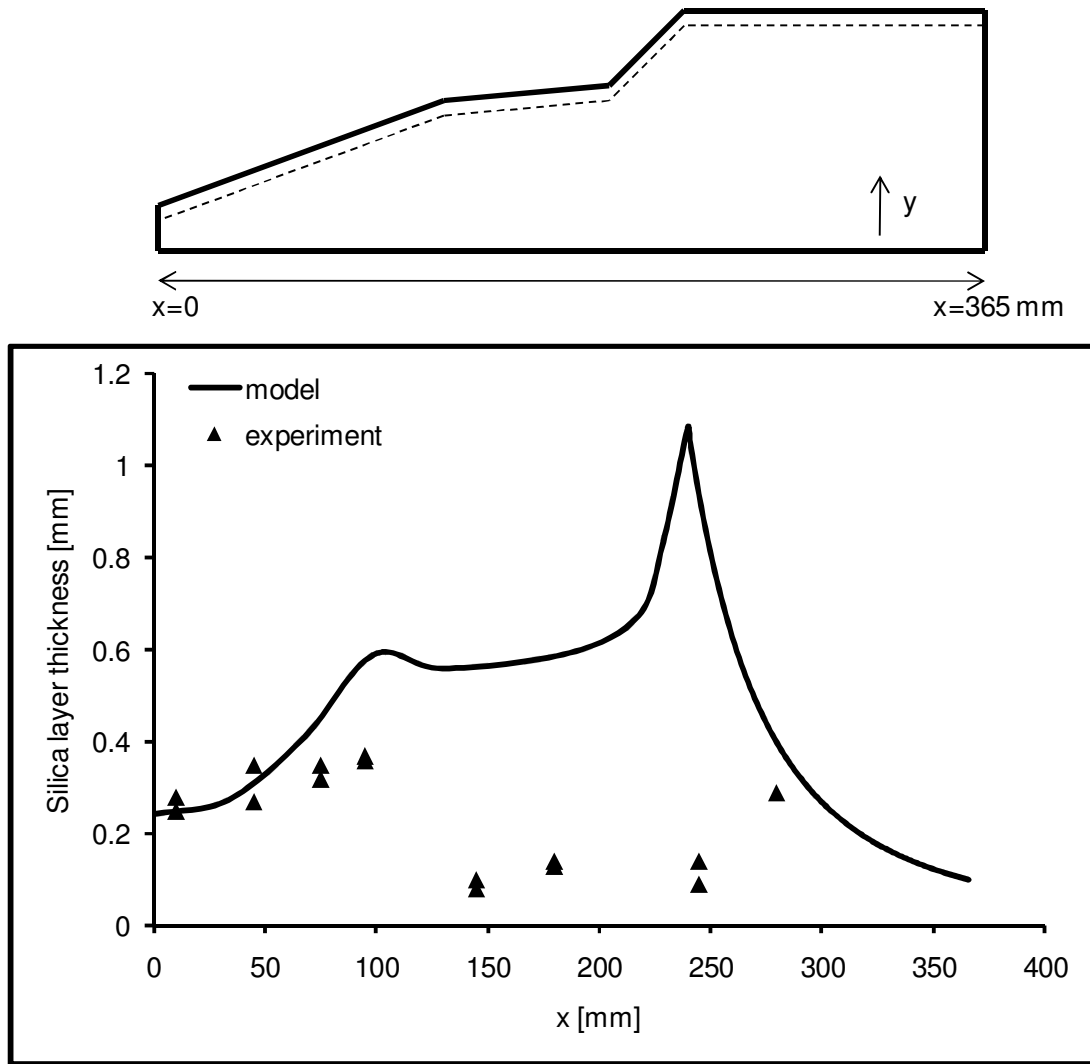


**Figure 47: Calculated layer thicknesses (solid line) compared to experimentally determined layer thicknesses (triangles). The schematic above is scaled in  $x$  to the graph below, the dotted line shows the position on the lamella where the layer thicknesses are determined.**

Figure 47 shows that the calculations and experimental values are similar up to  $x=100$  mm. The experimentally determined silica layer thickness at  $x=280$  mm is also close to the calculated value. The other three experimentally determined points ( $x=145$  mm,  $x=180$  mm and  $x=245$  mm) are not even near the calculated values. Note that these points are the same as the points where the density could not be determined accurately, which may be one of the reasons for the difference in layer thickness between model and experiment. Besides the possibility of an inaccuracy in the measurement it is unknown why the model and experiment differ so much from each other between  $x=100$  mm and  $x=250$  mm. Further research is necessary to find the cause for the difference. Note however that at higher concentrations the increased layer thickness around  $x \sim 240$  was also observed in an experiment (Figure 45).

The right peak in the layer thickness in the graph of Figure 47 at  $x = \sim 240$  mm is attributed to a decreased temperature and increased residence time in that area, as described before. The increase in the layer thickness up to  $x = 100$  mm is attributed to the decreasing concentration downstream (Figure 46).

According to calculations, the total amount of silica that deposits on the heat exchanger is around 90%, independent on the siloxane concentration. The reason that the yield of deposition is independent on siloxane concentration is that thermophoresis is the main deposition mechanism. As described before the particle size (which is dependent on the siloxane concentration) is independent on thermophoresis. Furthermore since particles are sufficiently small ( $< 1\mu\text{m}$ ) the assumption is made that inertial deposition does not occur. The calculated yield of deposition is similar to the experimentally determined yield of deposition, which was  $\sim 95\%$  (Appendix IV).

#### **5.4 Summary and conclusions: silica deposition model**

With the simplified model used to determine the layer thickness as a function of position in the Intergas heat exchanger, trends could be observed. An example of such a trend is that a large quantity of silica would deposit on top of the different lamella in the heat exchanger according to calculations. Near the back wall of the lamella heat exchanger almost no deposition was expected based on these calculations. In experiments with the Intergas boiler with different siloxane concentrations, these trends were also observed.

Another observed trend was that a large amount of silica would deposit in the middle of the heat exchanger. This would be the case because of an increased residence time (due to a decreased temperature and an increasing volume downstream) allowing for more time for deposition by thermophoresis and diffusion. In addition the increased temperature would result in an increased silica particle concentration further increasing the amount of deposition. In a high siloxane concentration ( $3.056 \text{ g/m}^3$  L2 in natural gas) experiment a large amount of silica was also observed to deposit in the middle of the heat exchanger. With the experiments in which the layer thickness and density of the silica layer were determined using alumina cubes, no increased amount of silica was determined to deposit in the middle of the heat exchanger. Further research is necessary to find the reason for the difference between the results of the high and low siloxane concentration experiments and the difference between model and experiment. In addition, to be able to make a proper quantitative analysis of the silica deposition as function of position thermophoresis for one, should be modeled with second order differential equations. Furthermore, the heat exchange in the y direction, which is neglected in our simplified model, should be taken into account for more accurate results.

The calculated silica yield of deposition was  $\sim 90\%$  in comparison to the  $\sim 95\%$  determined experimentally. This yield of deposition is independent on concentration because thermophoresis is the main deposition mechanism ( $> 99\%$  deposition due to thermophoresis). Thermophoresis is independent on particles size for small particles and therefore also independent on concentration (which influences the particle sizes).

## 6. Recommendations for future work

---

Some topics discussed in this thesis require further attention in order to remove uncertainties in the process of developing siloxane specifications for domestic appliances. One such a topic is the need to determine the impact of siloxanes on more (types of) domestic appliances. An example of such an appliance is the gas cooker, with gas cookers all combustion products are expelled into the interior, including any formed silica particles. Since these silica particles can be assumed to be sufficiently small ( $<100$  nm) they may contribute to an environmental or health burden. Further research is necessary in order to determine the extend of these burdens.

In this thesis the Intergas boiler with the lamella heat exchanger was assumed to be worst case in terms of susceptibility to clogging. This assumption should be tested by performing experiments with domestic boilers containing other types of heat exchangers (tube, finned tube, plate heat exchanger, etc.). These experiments could be performed at relatively low siloxane concentrations to determine if the flow resistance and time till failure due to the ionization probe still scale non-linearly at low concentrations ( $<5$  ppm).

In other domestic boilers the position of the ignition and ionization probes may differ, rendering them more or less sensitive to siloxane containing biogases. Also in modulating boilers, the thermal load of the appliance may influence the time till failure of the ionization probe. Further research is necessary to determine which ionization probe under which conditions fails first.

The geyser experiments in this thesis were performed at one siloxane concentration. Experiments with lower siloxane concentrations are necessary in order to determine how the CO emissions of the geyser scale with siloxane concentration.

The simplified silica yield model presented in this thesis should be expanded to perform a quantitative analysis of the silica deposition as function of position in heat exchangers. Thermophoresis (and diffusion) for example should be modeled with second order differential equations. The heat exchange in the y direction between lamella, which is neglected in the simplified model, should be taken into account for more accurate results.



## References

---

- [1] J. Holstein, specialist green gases, DNV KEMA, personal communication, September 27, 2012
- [2] R. Dewil, L. Appels, J. Baeyens, *Energy use of biogas hampered by the presence of siloxanes*, Energy Conversion and Management 47 (2006) 1711-1722
- [3] M. Hagmann, E. Heimbrand, P. Hentschel, *Determination of siloxanes in biogas from landfills and sewage treatment plants*, International Waste Management and Landfill Symposium 7, Cagliari, Italy (2001)
- [4] M. Portmann, *Siloxane in der Umwelt und im Klärgas*, AWEL Amt, Baudirektion Kanton Zürich (2009)
- [5] P. Huguen and G. Le Saux, *Perspectives for a european standard on biomethan: a Biogasmax proposal*, Biogasmax, Integrated Project No 019795 (2010)
- [6] K. Oshita, Y. Ishihara, M. Takaoka, N. Takeda, T. Matsumoto, S. Morisawa and A. Kitayama, *Behaviour and adsorptive removal of siloxanes in sewage sludge biogas*, Water Science & Technology-WST 61.8 (2010)
- [7] S. Rasi, *Biogas Composition and Upgrading to Biomethane*, Jyväskylä studies in biological and environmental science 202 (2009)
- [8] Martin Schweigkofler, Reinhard Niessner, *Removal of siloxanes in biogases*, Journal of Hazardous Materials B83 (2001) 183-196
- [9] S. Gersen, *Experimental study of the combustion properties of methane/hydrogen mixtures*, Proefschrift, Wiskunde en Natuurwetenschappen, Rijksuniversiteit Groningen (2007)
- [10] V.M. van Essen, *Fundamental limits of NO formation in fuel-rich premixed methane-air flames*, Proefschrift, Wiskunde en Natuurwetenschappen, Rijksuniversiteit Groningen (2007)
- [11] A.V. Sepman, *Effects of burner stabilization on nitric oxide formation and destruction in atmospheric pressure flat premixed flames*, Proefschrift, Wiskunde en Natuurwetenschappen, Rijksuniversiteit Groningen (2006)
- [12] G.P. Smith, D.M. Golden, M. Frenklach, N.W. Moriarty, B. Eiteneer, W. Goldenberg, C.T. Bowman, R. Hanson, W.C. Gardiner, V. Lissianski and Z. Qin, [http://www.me.berkeley.edu/gri\\_mech/](http://www.me.berkeley.edu/gri_mech/)
- [13] R.J. Kee, F.M. Rupley and J.A. Miller, *CHEMKIN II: A Fortran Chemical Kinetics Package for the Analysis of Gas-Phase Chemical Kinetics*, Sandia National Laboratories, Report No.SAND89-8009 (1989)
- [14] H.K. Chagger, D. Hainsworth, P.M. Patterson, M. Pourkashanian and A. Williams, *The formation of SiO<sub>2</sub> from hexamethyldisiloxane combustion in counterflow methane-air flames*, Twenty-Sixth Symposium (International) on Combustion/The Combustion Institute (1996) 1859-1865
- [15] A.V. Mokhov, *Silica formation from siloxanes in biogas: novelty or nuisance?*, ver. 3, International Gas Union Research Conference 2011 paper, Seoul (2011)

- [16] *CRC Handbook of Chemistry and Physics*, 85<sup>th</sup> edition, CRC Press: Boca Raton, p 3-522 (2004-2005) 9917
- [17] J. Lee, I. Altman and M. Choi, *Design of thermophoretic probe for precise particle sampling*, *Aerosol Science* 39, 418-431 (2008)
- [18] D. Boldridge, *Journal of Aerosol Science*, 44 (2010) 1821
- [19] C. Oh and C.M. Sorensen, *Colloid Interface Science*, 193 (1997) 17
- [20] W. Ostwald, *Zeitschrift Physikalische Chemie*, 22 (1897) 289
- [21] W. Ostwald, *Zeitschrift Physikalische Chemie*, 34 (1900) 495
- [22] Mandelbrot B. B., *The Fractal Geometry of Nature*, Freeman, San Francisco (1982)
- [23] R. Jullien and R. Botet, *Aggregation and Fractal Aggregates*, World Scientific, Singapore (1987)
- [24] D. Avnir, *The Fractal Approach to Heterogeneous Chemistry: Surfaces, Colloids, Polymers*, Wiley, Chichester (1989)
- [25] T. Vicsek, *Fractal Growth Phenomena*, World Scientific, Singapore (1989)
- [26] B.M. Smirnov, M. Dutka, M. van Essen, S. Gersen, P. Visser, D. Vainchtein, J.Th.M. De Hosson, H.B. Levinsky and A.V. Mokhov, *Growth of fractal structures in flames with silicon admixture*, *EPL*, 98 (2012) 66005
- [27] M.L. Eggersdorfer, D. Kadau, H.J. Herrmann and S.E. Pratsinis, *Aggregate morphology evolution by sintering: Number diameter of primary particles*, *Journal of Aerosol Science* 46 (2012) 7 – 19
- [28] S.F. Miller and D.P. Kalmanovitch, *Relation of Slag Viscosity and Surface Tension to Sintering Potential*, Pennsylvania State University's Department of Material Sciences (Fuel Science) and The University of North Dakota Energy and Mineral Research Center (1988)
- [29] D.A. Stephenson and R.J. Blint, *Theoretical Fitting of Computer Processed Laser Raman-Spectra from Methane-Air and Propane-Air Flames*, *Applied Spectroscopy* 33(1) (1979) 41-45
- [30] P. Meakin, *Physical Review Letters* 51 (1983) 1119
- [31] M. Kolb, R. Botet and R. Julien, *Physical Review Letters* 51 (1983) 1123
- [32] M.D. Allendorf, J.R. Bautista and E. Potkay, *Temperature-Measurements in a Vapor Axial Deposition Flame by Spontaneous Raman-Spectroscopy*, *Journal of Applied Physics* 66(10) (1989) 5046-5051
- [33] B.M. Smirnov, *Physics Uspekhi*, 54 (2011) 691
- [34] B. van Esch, C. van de Geld and E. Van Kemenade, *Procestechische Constructies 1 4B660*, Faculteit Werktuigbouwkunde, Technische Universiteit Eindhoven, <http://www.scribd.com/doc/58443886/PTC100> (2000)
- [35] J.H. Lienhard IV and J.H. Lienhard V, *A heat transfer textbook*, third edition, Phlogiston Press, Cambridge, Massachusetts (2008)
- [36] L.P.B.M. Janssen and M.M.C.G. Warmoeskerken, *Transport Phenomena Data Companion*, third edition, VSSD, Delft (1987)
- [37] J.L. Liu, *Convection-Diffusion-Reaction Model*, Department of Applied Mathematics, National University of Kaohsiung (2007)

- [38] S.K. Friedlander, *Smoke, Dust, and Haze Fundamentals of Aerosol Dynamics*, second edition, Oxford University Press, Oxford, New York (2000)

## Appendix I: Gravimetric determination of siloxane concentrations

The concentrations of siloxanes L2, D4 and D5 in the methane flow leaving the gas bubblers have been experimentally determined via the gravimetric method in triplo. From the results the concentrations ( $C_{exp}$ ) have been calculated using equation (3) (paragraph 3.1.2). The experimental results are compared with theoretical concentrations ( $C_{theory}$ , calculated with equation (2) from paragraph 3.1.2) for a saturated siloxane vapor at 25 °C. For L2, D4 and D5 the results of the experiments are shown in Table 4, Table 5 and Table 6 respectively.

**Table 4: Gravimetric determination of the L2 concentration in methane.**

Number [-]	Mass L2 [g]	Time [min]	$\phi_v$ [m <sup>3</sup> <sub>n</sub> /min]	T <sub>exp</sub> [°C]	P <sub>exp</sub> [Pa]	C <sub>exp</sub> [g/m <sup>3</sup> <sub>n</sub> ]	C <sub>theory</sub> [g/m <sup>3</sup> <sub>n</sub> ]
1	1.40	5.0	$1.895 \cdot 10^{-3}$	21.2	263000	147.8	154.6
2	2.39	5.0	$3.065 \cdot 10^{-3}$	21.5	263000	156.0	154.6
3	2.27	5.0	$3.063 \cdot 10^{-3}$	21.2	263000	148.2	154.6
Average	-	-	-	-	-	150.7	154.6

**Table 5: Gravimetric determination of the D4 concentration in methane.**

Number [-]	Mass D4 [g]	Time [min]	$\phi_v$ [m <sup>3</sup> <sub>n</sub> /min]	T <sub>exp</sub> [°C]	P <sub>exp</sub> [Pa]	C <sub>exp</sub> [g/m <sup>3</sup> <sub>n</sub> ]	C <sub>theory</sub> [g/m <sup>3</sup> <sub>n</sub> ]
1	1.64	510	$6.63 \cdot 10^{-4}$	22.3	331000	4.85	5.60
2	1.63	497	$6.56 \cdot 10^{-4}$	22.4	331000	5.00	5.60
3	1.66	455	$6.57 \cdot 10^{-4}$	22.1	331000	5.55	5.60
Average	-	-	-	-	-	5.13	5.60

**Table 6: Gravimetric determination of the D5 concentration in methane.**

Number [-]	Mass D5 [g]	Time [min]	$\phi_v$ [m <sup>3</sup> <sub>n</sub> /min]	T <sub>exp</sub> [°C]	P <sub>exp</sub> [Pa]	C <sub>exp</sub> [g/m <sup>3</sup> <sub>n</sub> ]	C <sub>theory</sub> [g/m <sup>3</sup> <sub>n</sub> ]
1	1.10	158.6	$5.67 \cdot 10^{-3}$	19.6	223000	1.22	2.00
3	0.62	90	$5.67 \cdot 10^{-3}$	20.0	223000	1.21	2.00
2	0.60	90	$5.67 \cdot 10^{-3}$	19.6	223000	1.18	2.00
Average	-	-	-	-	-	1.20	2.00

In Table 4 and Table 5, it can be seen that the theoretical concentrations are slightly higher than the average experimentally determined concentrations for siloxanes L2 and D4. This difference may be due to the temperatures during experiments. These temperatures were lower for each experiment than the 25 °C at which the theoretical concentration was determined. At lower temperatures the saturation concentration decreases resulting in a reduced concentration during experiments. It should also be noted that an analog pressure gauge was used with an approximated accuracy of 5000 Pa. Taking into account the differences in temperature between calculations and theory and the experimental

uncertainties we assume that all methane leaving the gas bubblers is saturated with siloxanes for L2 and D4.

In Table 6, it can be seen that the concentration of D5 varies more from the theoretically expected value. This relatively large difference cannot be contributed to experimental uncertainties. Furthermore in a set of experiments with varying flows through the gas bubblers the experimentally determined concentration remained between 60-65% of the theoretical expected value ( $T=19-22\text{ }^{\circ}\text{C}$ ). This suggests that the methane leaving the gas bubblers is saturated. For experiments performed in this thesis the experimentally determined concentrations are used. Therefore the difference between theoretical values and experimental values do not compromise any of the obtained results. Possibly the difference can be attributed to the D5 vapor pressure being more sensitive to temperature variations. Further research is necessary to verify if this is the case.

## Appendix II: Optimization of the sampling probe design

The first design of the sampling probe in the thermophoretic sampling system was simple. A hole with a notch in the tip of the probe assured the TEM grid could be fixed into place using a cover plate. Some preliminary experiments were performed with thermophoretic sampling of silica particles in a flame using the first probe design. A flame with flow rate  $p \cdot v = 0.028 \text{ g} \cdot \text{cm}^{-2} \cdot \text{s}^{-1}$  ( $T_{\text{max}} = 2120 \text{ K}$ ) and a L2 concentration of  $191 \text{ g/m}^3_n$  was used. Even though this is considered a high concentration of siloxanes a modest amount of silica particles were found on the grids after TEM analysis. Also all particles found were large fractal aggregates instead of smaller individual clusters or primary particles, even at 4 mm above the burner surface. At this height individual particles would be expected, since insufficient time has elapsed for the formation of fractal aggregates. Furthermore the influence of concentration and sampling time were negligible. This behavior was previously discovered by J. Lee et al. [17] who contributed it to a faulty probe design. Therefore a new probe design was developed, the new probe design compared to the old is shown in Figure 48.

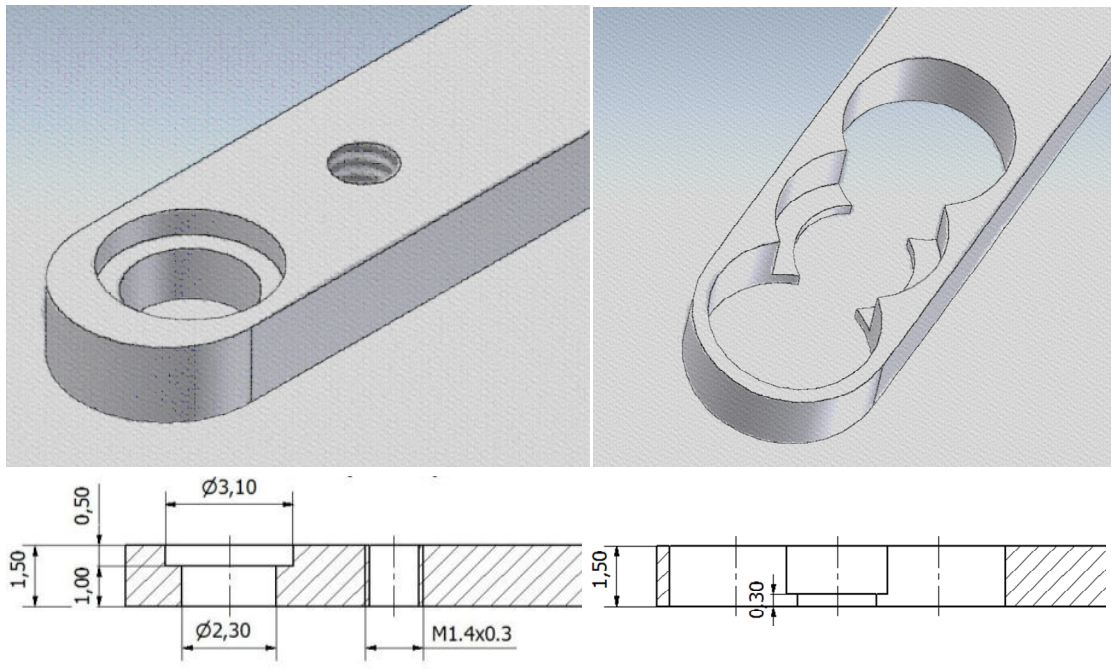


**Figure 48: Schematic of the old probe design on the left and the new probe design on the right.**

With silica sampling the flow lines of hot flue gases are such that molecules, and particles up to  $1 \mu\text{m}$ , move around the probe creating a stagnant zone. The concept of thermophoretic sampling is that particles that flow along the flow lines are pulled towards the grid through the stagnant zone due to the temperature difference of the hot flue gases and the cold grid. The stagnant zone of the old sampling probe is probably too big for most particles to cross. The new probe has been designed in such a way that the flow lines are

closer to the grid which reduces the volume of the stagnant zone significantly. The grid has also been lowered which further reduces the volume of the stagnant zone. This has been done by drilling holes where the combustion gases can move through near the grid. The new probe has been tested with the same flame ( $p \cdot v = 0.028 \text{ g} \cdot \text{cm}^{-2} \cdot \text{s}^{-1}$ ) and L2 concentration ( $191 \text{ g/m}^3_n$ ) as the old probe. The TEM images of grids sampled with the new and the old probe are compared in Figure 49 for heights of 4 and 8 mm above the burner surface.

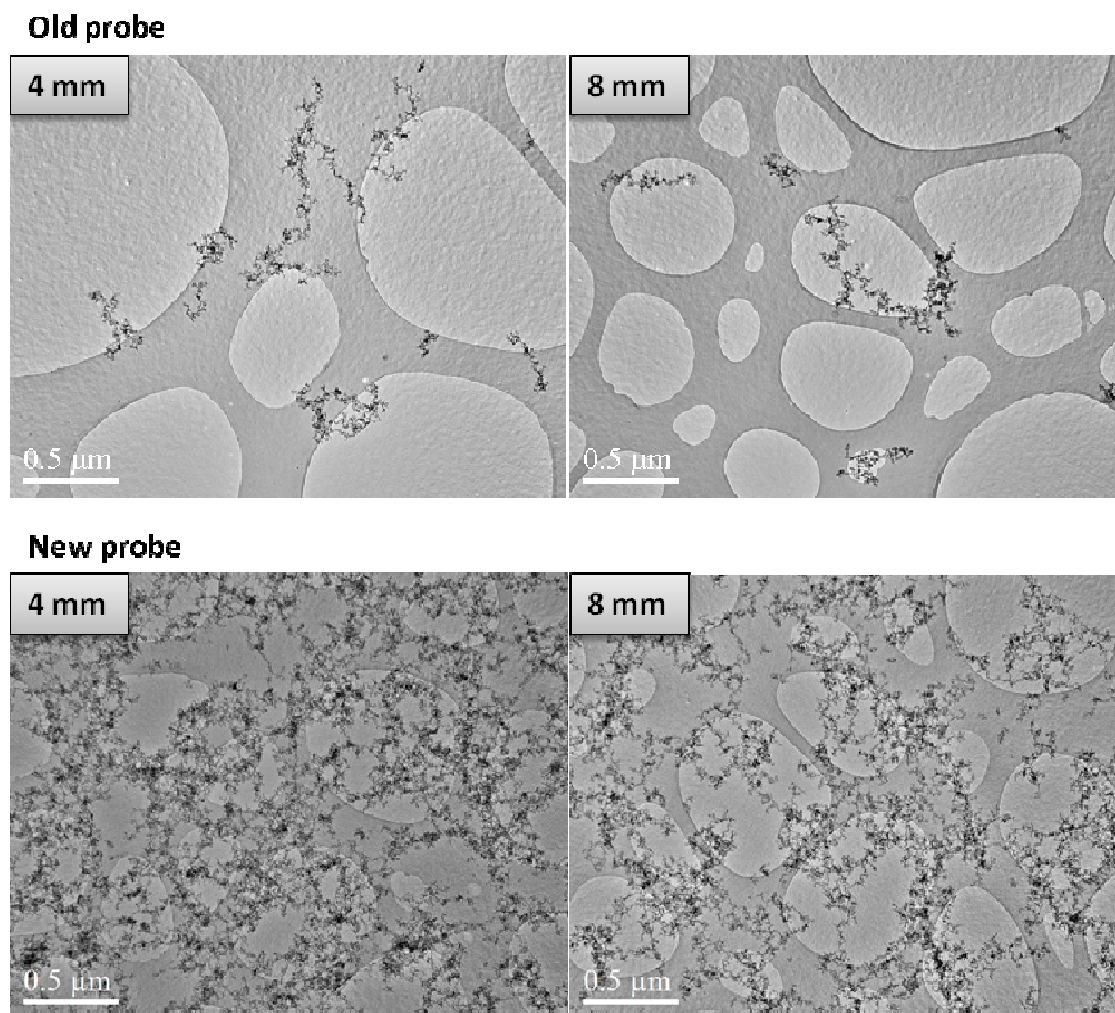


**Figure 49: TEM images of grids sampled with the old probe above and the new probe below for heights of 4 and 8 mm.**

The difference between the TEM images from grids sampled with the old probe and the new probe are clearly visible. With the new probe the amount of particles that stick to the grid is significantly increased, the number density on this grid is so large that individual particles can no longer be distinguished. By reducing the concentration of siloxanes we have shown in paragraph 3.2.2 that individual particles are distinguishable. Therefore the newly designed probe is assumed to sample particles which are representative for particles in the flame in terms of morphology and size.

### Appendix III: The TEM image processing

---

The pre-processing and analysis of TEM images was performed as described in Ref. [18]. The pre-processing consisted of: 1) converting a grayscale image using a double-threshold technique with manual selection of narrow and wide range of intensity values; 2) morphological opening of binary image to remove residual noise; and 3) examination to verify the identification of particles boundaries, with manual adjustments where necessary. Figure 50 shows an example of typical TEM image used in this study [26].

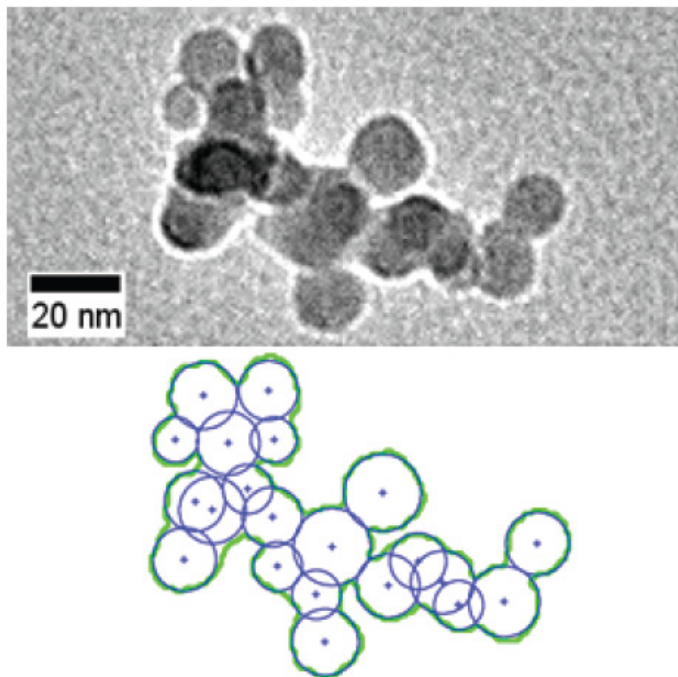


**Figure 50: TEM image showing a typical aggregate before (above) and after (below) image pre-processing and manual primary particle identification [26].**

The software allows us to automatically determine the projected area of aggregate and its maximal size. Positions of the clusters with respect to the geometric centre of the aggregate were manually measured to determine its radius of gyration  $R_g$ . Also, the software allowed for the determination of the cluster sizes after the manual measurement of their positions. The fractal aggregates with unidentified clusters were rejected from the analysis. In total, the diameters of more than 10000 clusters in approximately 1700 fractal aggregates were measured. The mean cluster radius  $a$ , was calculated for each sample which contained between 1000 and 2000 clusters. The shape of the distribution of diameters of clusters in every sample is close to that of the log-normal distribution with a standard deviation of approximately 20-25% of the mean cluster diameter [26].



## Appendix IV: Silica mass balance over the Intergas domestic boiler

Silica particles which do not deposit on the heat exchanger of the Intergas boiler may be expelled into the exterior. Also silica particles may be removed via the siphon used as a drain for the condense water. To determine where most of the particles end up, experiments are performed in which a HEPA filter is installed in the chimney of the appliance and the water from the siphon is filtered. A photograph taken of the Intergas boiler with the HEPA filter installed is shown in Figure 51. The siloxane concentration in the first experiment was determined to be  $0.328 \text{ g/m}^3_{\text{n L2}}$  in natural gas. After 102 hours of operation, 37.9 grams of silica were produced of which 2.3 grams (6.1 %) were found in the HEPA filter and 0.2 grams (0.5 %) were found in the water siphon. For a second experiment with a concentration of  $0.974 \text{ g/m}^3_{\text{n L2}}$  in natural gas, 5.4 grams of silica were produced of which 0.3 grams (5.6 %) were found in the HEPA filter. These results indicate that most of the silica in the Intergas boiler deposits on the heat exchanger independent of the siloxane concentration. This is in correspondence with the expectations, since the produced silica particles are all smaller than  $1 \mu\text{m}$  and no inertial deposition occurs, the main deposition mechanism is thermophoresis (see chapter 5). With thermophoresis the fraction of particles that deposit on a surface is independent on the particle size (for small particles).



Figure 51: Photograph of the Intergas boiler with a HEPA filter in the exhaust gas pipe.

## Appendix V: Temperature profile in the Intergas boiler

The temperature profiles in the y direction for different values of x in the Intergas boiler are calculated and measured with thermocouples. The comparison of these measurements and calculations are shown as graphs in Figure 52 for x=140 mm, Figure 53 for x=200 mm and Figure 54 for x=240 mm. The load of the appliance was fixed to 84% of full load, which corresponds to a natural gas flow of 1.8 m<sup>3</sup>/h. In general there is a good agreement between measurements and calculations for the temperature profile in the y direction for different values of x. The biggest difference in temperature between calculations and measurements of ~200 °C can be seen in Figure 52. This difference can be contributed to the neglecting of the heat transfer in the y direction. This would result in an overestimation of the temperature for high values of y and an underestimation for low values of y. This behavior can be seen in each of the figures below.

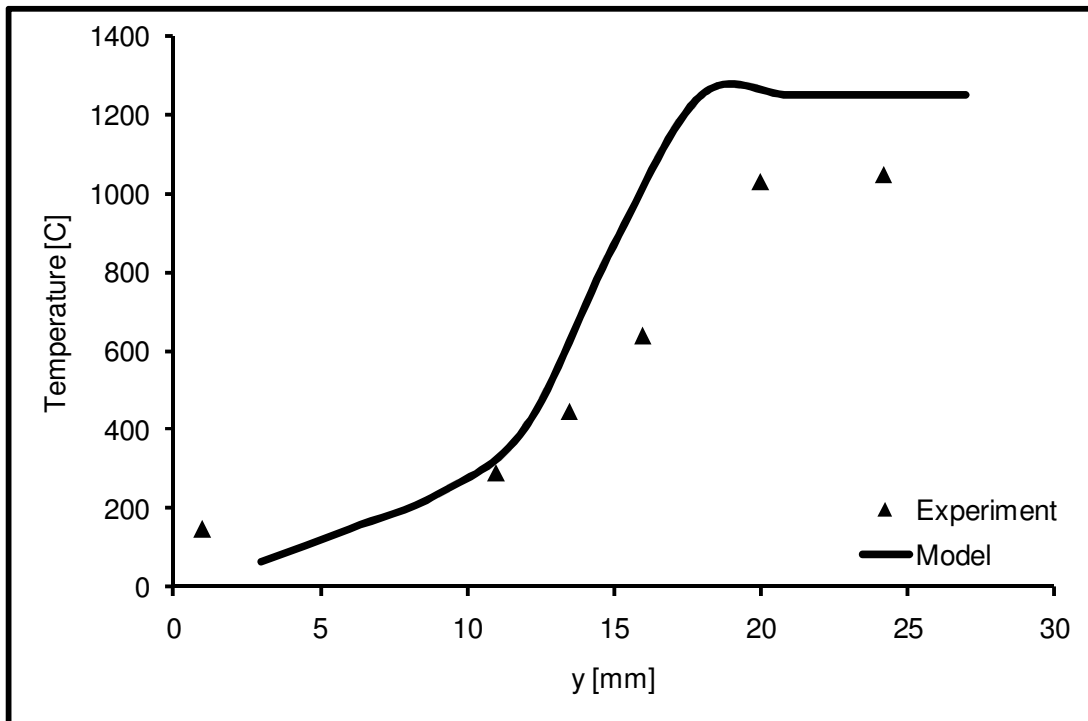


Figure 52: Model to experiment comparison with the temperature between the lamella of the Intergas boiler in the y direction for x=140 mm.

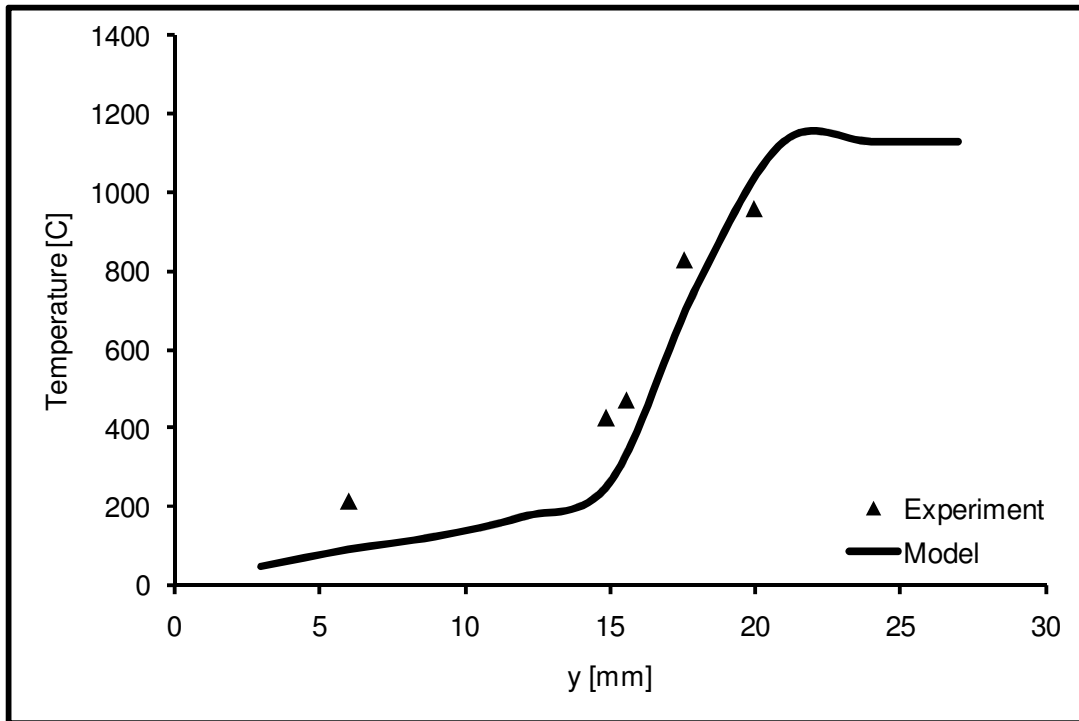


Figure 53: Model to experiment comparison with the temperature between the lamella of the Intergas boiler in the y direction for x=200 mm.

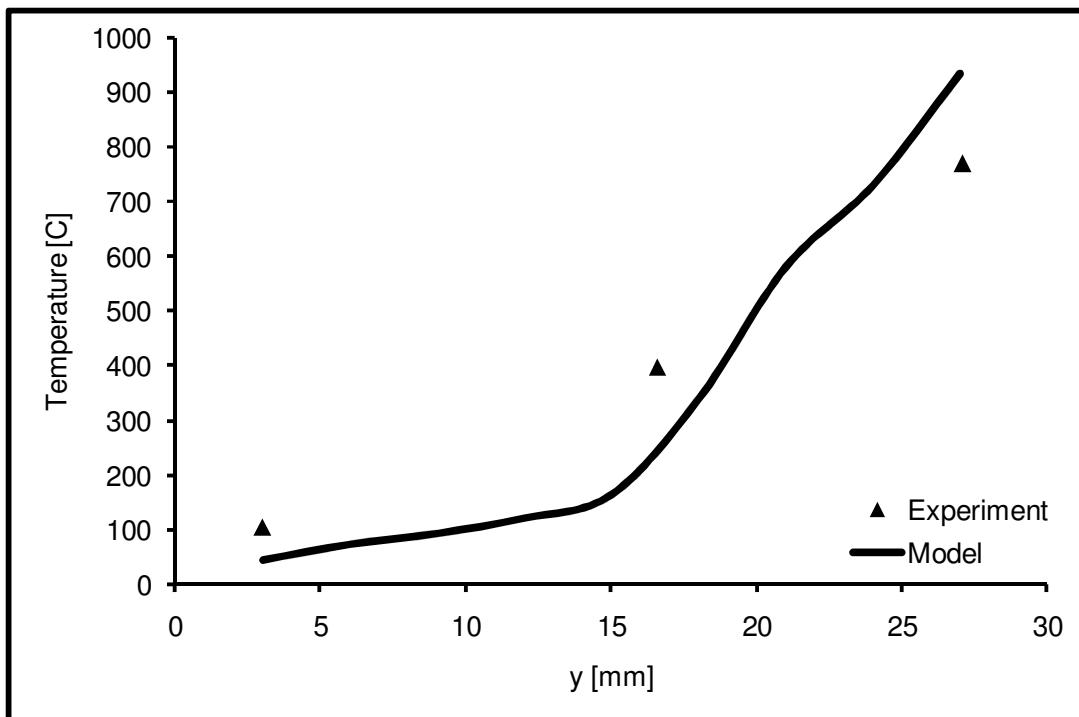
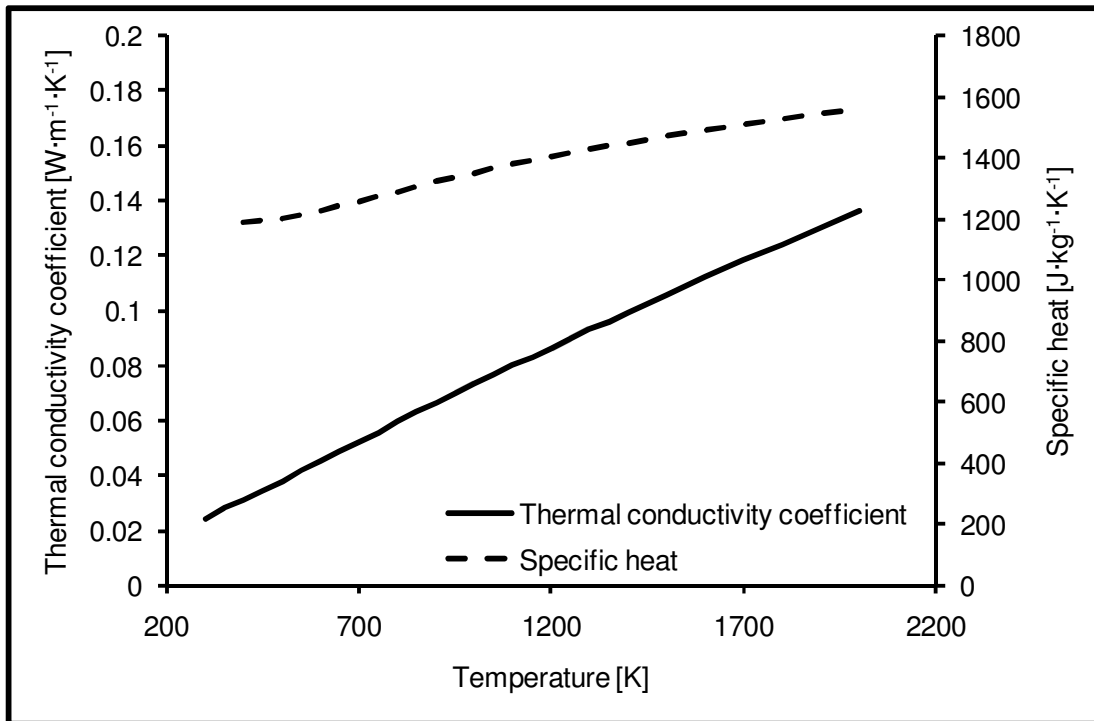


Figure 54: Model to experiment comparison with the temperature between the lamella of the Intergas boiler in the y direction for x=240 mm.

## Appendix VI: Thermal conductivity coefficients and specific heats

The thermal conductivities for aluminum, copper and water used for the temperature profile calculations in this thesis are more or less constant since the wall temperature only varies up to 50 K in the Intergas heat exchanger. For  $k_{al}$ ,  $k_{cu}$  and  $k_{H_2O}$  the values 235, 400 and  $0.62 \text{ W}\cdot\text{m}^{-1}\cdot\text{K}^{-1}$  (for  $T=323 \text{ K}$ ) were used respectively [16]. For the specific heat of water the value  $4180 \text{ J}\cdot\text{kg}^{-1}\cdot\text{K}^{-1}$  (for  $T=323 \text{ K}$ ) was used [16]. The composition of the flue gases in the heat exchanger was calculated using PREMIX (75%  $\text{N}_2$ , 8%  $\text{CO}_2$  and 17%  $\text{H}_2\text{O}$  (g)). Each component fraction was multiplied with the specific heat or thermal conductivity coefficient [16]. The addition of these values yielded the average specific heat and thermal conductivity coefficients for the flue gases. Figure 55 shows the specific heat and thermal conductivity for the flue gases as a function of temperature.



**Figure 55: Thermal conductivity coefficient and specific heat of the flue gases (composition 75%  $\text{N}_2$ , 8%  $\text{CO}_2$  and 17%  $\text{H}_2\text{O}$  (g)) as a function of temperature.**